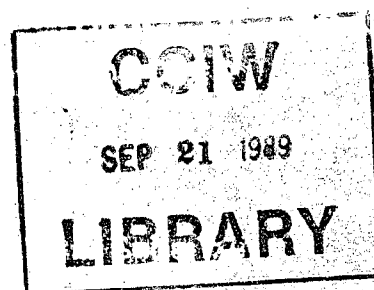


CANADA INLAND WATERS Directorate  
SCIENTIFIC SERIES  
#171



GB  
707  
C335  
no. 171E



Environment  
Canada

Environnement  
Canada

# **The Circulation of Lake Ontario during the Summer of 1982 and the Winter of 1982/83**

**T.J. Simons and W.M. Schertzer**

**SCIENTIFIC SERIES NO. 171**

**NATIONAL WATER RESEARCH INSTITUTE  
LAKES RESEARCH BRANCH  
CANADA CENTRE FOR INLAND WATERS  
BURLINGTON, ONTARIO, 1989**

*(Disponible en français sur demande)*

Published by authority of  
the Minister of the Environment

© Minister of Supply and Services Canada 1989

Cat. No. En 36-502/171E

ISBN 0-662-16915-8

# Contents

	Page
ABSTRACT.....	v
RÉSUMÉ.....	vii
1. PURPOSE OF STUDY AND SUMMARY OF RESULTS.....	1
1.1 Introduction.....	1
1.2 Experimental Program.....	4
1.3 Results of Summer Study.....	8
1.4 Results of Winter Study.....	9
1.5 Acknowledgments.....	10
2. SUMMER STUDY: NORTH-SOUTH TRANSECT.....	14
2.1 Wind and Wind Stress.....	14
2.2 Surface Waves.....	17
2.3 Temperature.....	21
2.4 Currents.....	24
2.5 Response of Lake to Wind.....	29
3. SUMMER STUDY: NORTH SHORE.....	71
3.1 Alongshore Variation of Temperature and Currents.....	71
3.2 A Simple Model of Coastal Upwelling.....	73
3.3 Stratification and Topography in Coastal Waters.....	78
3.4 Two-layer Response to Alongshore Wind Wave.....	80
3.5 Two-layer Response to Observed Wind.....	87
3.6 Multi-level Temperature Model.....	95
4. WINTER STUDY: NORTH-SOUTH TRANSECT.....	116
4.1 Current Measurements.....	116
4.2 Transport Calculations.....	118
4.3 Dynamics of Large Lake Circulations.....	123
4.4 Numerical Models.....	126
4.5 Model Resolution.....	130
4.6 Short-term Current Fluctuations.....	135
4.7 Long-term Circulations.....	141
4.8 Discussion.....	145
4.9 Conclusions.....	149
5. WINTER STUDY: NORTH SHORE.....	170
5.1 Introduction.....	170
5.2 Time Series Analysis.....	171
5.3 Spectral Analysis.....	174
5.4 Empirical Models.....	177
5.5 Summary and Conclusions.....	181
REFERENCES.....	187

## Abstract

The International Field Year on the Great Lakes (IFYGL) in 1972 provided a wealth of knowledge on water movements in Lake Ontario. During the IFYGL Study, observations were primarily carried out in the stratified season. A limited network of mid-lake current meter stations was maintained during the 1972/73 winter, but the resolution of the array was too thin to provide a clear picture of winter circulation. Furthermore, the IFYGL data were often difficult to reconcile with the model results, particularly in the nearshore zone during the homogeneous season. Thus, the IFYGL Study left a number of questions unanswered while actually raising some new ones.

To address these problems, a major experimental program was carried out in Lake Ontario during the summer of 1982 and the following winter. Hydrodynamical and empirical modeling procedures were employed to design the field program and to analyze the results. This study provides a detailed description and analysis of nearshore current reversals related to wind forcing and alongshore propagation of topographic and baroclinic wave phenomena; cross-lake variations of currents in terms of wind forcing, cross-lake depth variations, and effects of friction and diffusion in shallow water; and the relative effects of wind-induced upwelling, alongshore Kelvin waves, and small-scale mixing on the nearshore thermal regime in spring, summer and fall.

The current distributions are shown to have strong implications on water quality and fate and pathways of toxic contaminants in the aquatic system.

## Résumé

À l'occasion de l'année internationale d'étude des Grands Lacs en 1972, la communauté scientifique a énormément appris sur les mouvements de l'eau du lac Ontario. La plupart des observations effectuées au cours de cette étude ont coïncidé avec la période de stratification thermique des eaux. Bien que pendant l'hiver de 1972-1973, on ait laissé en place un réseau limité de courantomètres dans le centre du lac, la résolution du réseau était trop grossière pour produire une représentation précise des courants en hiver. De plus, dans plusieurs cas, les données recueillies pendant cette période ne concordaient pas avec les prédictions des modèles, notamment celles qui s'appliquaient à la zone littorale en l'absence de stratification thermique. Par conséquent, au terme de l'année d'étude des Grands Lacs plusieurs questions sont restées en suspens tandis que d'autres ont été soulevées pour la première fois.

Durant l'été de 1982 et l'hiver suivant, un vaste programme d'études sur le terrain a été mis sur pied pour répondre à ces questions. On a eu recours à des modèles empiriques et hydrodynamiques pour déterminer les types de mesures expérimentales souhaités et les méthodes d'analyse des données. Cette étude fait l'analyse et la description détaillées de l'inversion des courants littoraux en fonction de la poussée des vents prédominants et de la propagation le long de la rive des perturbations d'origine topographique et baroclinique; des fluctuations du courant d'un bout à l'autre du lac en fonction de la poussée du vent, du relief du fond et des effets de friction et de dispersion en eau peu profonde; et de l'importance relative des effets de la remontée des eaux sous la poussée du vent, des vagues de Kelvin (qui se propagent parallèlement à la rive) et des échanges de faible envergure qui caractérisent les régimes thermiques près de la rive au printemps, en été et à l'automne.

On a démontré que dans le réseau aquatique, la répartition des courants a des effets importants sur la qualité de l'eau ainsi que sur l'acheminement et le devenir des contaminants toxiques.

## Purpose of Study and Summary of Results

### 1.1 Introduction

In the Great Lakes, as well as in the world's oceans, the coastal zones are the areas of most immediate interest to the general public. It is therefore not surprising that current limnological and oceanographic research places considerable emphasis on the physics and biochemistry of these zones. While there are many conceptual models and theoretical ideas concerning the dynamics of coastal waters, it appears difficult to identify the relative effects of different processes and forces in any particular situation and, hence, to arrive at an adequate deterministic model.

The overall circulation of large lakes is characterized by complicated variations in space and time. Detailed measurement of such circulations would require deployment of self-recording current meters at numerous locations and various depths, which is not a practical proposition. In the past, therefore, lake circulation studies have generally relied on a sparse network of instruments covering the whole lake and have tried to fill the voids by interpolation and by recourse to hydrodynamical models (see e.g., Pickett, 1976). While circulation models of large lakes appear to give adequate simulations of the current response to strong wind impulses, their overall reliability is less impressive (Allender,

1977; Simons, 1980; Schwab, 1983). Clearly, it is desirable to design a measurement program which permits unambiguous interpolation between instruments and allows for verification of mass conservation requirements. This suggests a high resolution array of current recorders in one or more cross sections of a lake.

In order to address these problems, a major experimental program was carried out in Lake Ontario during the summer of 1982 and the following winter. Hydrodynamical and empirical modeling procedures were employed to design the field program and to analyze the results. The objectives of the 1982/83 Lake Ontario study were:

- (1) To relate nearshore current reversals to wind forcing and alongshore propagation of topographic and baroclinic wave phenomena.
- (2) To analyze cross-lake variations of currents in terms of wind forcing, cross-lake depth variations, and effects of friction and diffusion in shallow water.
- (3) To determine the relative effects of wind-induced upwelling, alongshore Kelvin waves, and small-scale mixing on the nearshore thermal regime in spring, summer and fall.
- (4) To study the impact of mass exchanges between the coastal zone and open lake on seasonal variations of nutrients and other water quality parameters in the nearshore zone.
- (5) To compute seasonal mass budgets of nutrients in the nearshore zone by recourse to observations of biochemical conversion rates, and



- (6) To delineate the seasonal characteristics of the Niagara River plume in spring, summer and fall in support of toxic contaminant studies and other related biochemical surveys in the Niagara River plume.

The present study addresses itself to objectives (1) - (3) and specifically to the dynamics of coastal waters along the northshore of Lake Ontario and offshore variations of temperature and currents in a north-south transect. A report on the dynamics of the Niagara River plume has already been published by Murthy et al. (1984). In order to meet objectives (4) and (5), a biochemical surveillance program was carried out under the title "Lake Ontario Nutrient Assessment Study (LONAS)". The pathways of toxic contaminants in the Niagara River plume were studied in a concurrent program, "Operation Niagara".

A wealth of information on water movement in Lake Ontario has been obtained during the 1972 International Field Year (IFYGL). For an extensive bibliography and review of results of the program, reference is made to Saylor et al. (1981). The IFYGL study was primarily concerned with the stratified season, and in particular the nearshore observations were limited to that season. Although a network of mid-lake moorings was maintained during the following winter, the resolution of the array was insufficient to arrive at a clear picture of the winter circulation. Furthermore, the current meter data were often difficult to reconcile with available model results. Thus the IFYGL study left a number of questions unanswered and actually raised some new ones.

One of the most striking observations during the 1972 Field Year was a strong eastward current along the south shore of Lake Ontario. During the stratified season this boundary current formed part of the lake-wide counterclockwise circulation associated with generally warmer water in the shore zones (Saylor et al., 1981). The limited observations during the winter of 1972/73 indicated that this current persisted during the homogeneous season but the origin and extent of the phenomenon was not clear. The 1982/83 measurements to be discussed in the present paper provide a much more detailed description of this eastward flow along the south shore of Lake Ontario. In addition, the present measurements show how this flow is balanced by a westward flow in the interior of the lake.

## 1.2 Experimental Program

The summer program of the 1982/83 Lake Ontario study covered a four-month period from early May to late August, 1982. Continuous time series of temperatures, currents, winds and waves for this period are available from eight fixed temperature profilers, some forty current meters, four meteorological buoys on the lake, a number of shore-based meteorological stations and one waverider. Most of the instruments were located in a cross section of the lake between Port Hope, Ontario, and Point Breeze, New York. Two coastal transects were established 30 km east and west of the main transect. Additional

current meters were moored in a transect from the Niagara River to Toronto as part of the Niagara River study (Murthy et al., 1984). These moorings will not be considered here.

The upper part of Figure 1.1 shows the location of the main transect, the two coastal transects and the network of meteorological stations. The lower part of Figure 1.1 shows the depth profile of the central cross-section with current meters identified by black dots and fixed temperature profilers by vertical lines. The offshore location of the current meter moorings and the measurement depths are summarized in Table 1.1. Only stations with complete or substantial data return are included. Current meters were actually placed at the 10-m level of each mooring but, as seen from Table 1.1, many of these instruments failed to return useful data while others provided only partial records.

During the winter of 1982/83, current meters were deployed in two arrays, the first one following the 50-m depth contour along the northshore, the second one extending across the lake from Port Hope, Ontario to Point Breeze, New York (top of Fig. 1.2). Current meters were placed at depths of 12 m below the surface and 1 m above the bottom and at a few intermediate depths in the cross-lake array (bottom of Fig. 1.2). A total of 34 complete records were obtained for the 140-day period of measurements, 4 November 1982 to 23 March 1983. The distance between stations and measurement depths are summarized in Table 1.2, and the bathymetry in the area of interest is shown in Figure 1.3.

**Table 1.1 Current meter moorings with complete data return for period 6 May to 30 August 1982. Partial records in parentheses**

Station	Distance from North Shore (km)	Water Depth (m)	Instrument Depths (m)	
C1	5.4	29	10	28
C2	8.0	54	10	53
C3	14.3	76	(10)	30 75
C4	21.0	100		30, 50 99
C5	23.6	112	10	111
C6	30.5	146	10	145
C7	38.6	177	(10)	30 176
C8	47.5	170	10	169
C9	55.8	93	(10)	92
C10	57.4	75	10	74
C11	59.3	52	10	
C12	61.6	31	(10)	30
South Shore	64.2			
E1	4.7	31		30
E2	11.3	51	10	50
E3	17.3	80	(10)	79
E4	26.0	110		109
W1	4.0	32		31
W2	8.0	53		52
W3	15.0	80	10	79
W4	22.2	109	(10)	(108)

**Table 1.2 Listing of current meter moorings with complete records in alongshore array (above), and cross-lake array (below), 4 November 1982 to 23 March 1983**

Station	A1	A2	A3	A4	A5	A6	A7
Alongshore distance (km)	0	16	33	49	64	79	94
Sounding depth (m)	49	50	54	51	51	51	50
Depths of current meters (m)	{ 12		12	12			12
	{ 48	49		50	50	50	49

Station	Distance from north shore (km)	Water depth (m)	Instrument depths (m)
C1	5.2	28	12
C2	8.3	54	12
C3	15.1	74	12
C4	21.7	100	12
C5	24.0	112	12
C6	30.7	147	12
C7	40.2	180	12
C8	47.4	171	12
C9	55.6	95	12
C10	57.3	74	
C11	59.2	52	
C12	61.4	29	12
South shore	64.2		

### 1.3 Results of Summer Study

Observations of currents and temperature along the northshore of Lake Ontario confirm the anticipated effect of wind forcing. Alongshore wind components induce alongshore current components and move the surface water to the right of the wind direction, thus causing upwelling for westerly winds and downwelling for easterly winds. The wind-induced upwelling or downwelling occurs more or less simultaneously along the whole northshore because the wind field is rather uniform over the lake. However, the relaxation of the thermocline after a storm tends to propagate from east to west in the form of an internal Kelvin wave. This wave can be accompanied by strong currents.

The temperature measurements are used to compare different models for simulating the response of stratified coastal waters to wind forcing. Coupling of the baroclinic and topographic response is evaluated for the area of interest and is found to lead to significant changes in the speed of alongshore wave propagation. The results affirm that alongshore variations must be included in an upwelling model and, hence, such models are inherently three-dimensional. Comparison of conventional two-layer models with multi-level temperature models shows good agreement.

Observations of temperature in the north-south cross section of Lake Ontario are interpolated to determine two-day averaged

temperature distributions for the period May 9 to August 28, 1982. The development of lake stratification is illustrated from the onset of the thermal bar in spring to the establishment of the lake-wide summer thermocline. Temperature variations in summer are dominated by wind-induced upwelling and downwelling events.

Current meter observations in the north-south cross section show that currents are quite uniform between the thermocline and the bottom. Persistent boundary currents exist throughout the season. Along the north shore the water flows from east to west, along the south shore the currents run from west to east.

#### 1.4 Results of Winter Study

Observations of winds and currents along the northshore of Lake Ontario are analyzed to evaluate effects of topographic wave propagation on wind-driven currents. Lagged cross-correlations and spectral transfer functions between winds and currents are found to be consistent with the mechanism of resonant topographic wave response in the presence of bottom friction. Transfer function models in the time domain are shown to explain 70 to 80 percent of the variance of observed currents.

In the north-south cross section, nearshore current fluctuations are large and generally coherent with wind variations, while currents in deep water tend to flow in opposite direction and are quite uniform in the vertical. Time-averaged currents show a

pronounced maximum of eastward flow along the south shore balanced by westward flow in the central part of the cross section, while the net transport near the northern shore tends to vanish. The total transport in the belt of eastward flow is ten times larger than the hydraulic transport associated with the Niagara-St. Lawrence flow. Since only 10% of this flow can leave the lake through the St. Lawrence, 90% of the Niagara discharge must be recirculated.

The current meter observations are used to evaluate the performance of circulation models for different time scales. The study takes advantage of the high data resolution to verify conservation of total water transport through the cross section. The results indicate that a typical linear hydrodynamic model can reproduce short- and medium-term circulations induced by wind variations but that nonlinear effects must be included to simulate seasonal current patterns.

#### 1.5 Acknowledgements

The measurement program was planned and coordinated by J.A. Bull, C.R. Murthy and F.M. Boyce, the field data were processed by J.A. Bull, F. Chiocchio, M.F. Kerman and D.B. Robertson, and the satellite data was provided by A. Condal and G. Irbe of the Atmospheric Environment Service. M.A. Donelan supplied the wave prediction program, and A.H. El-Shaarawi and D.C.L. Lam provided advice on empirical model design.



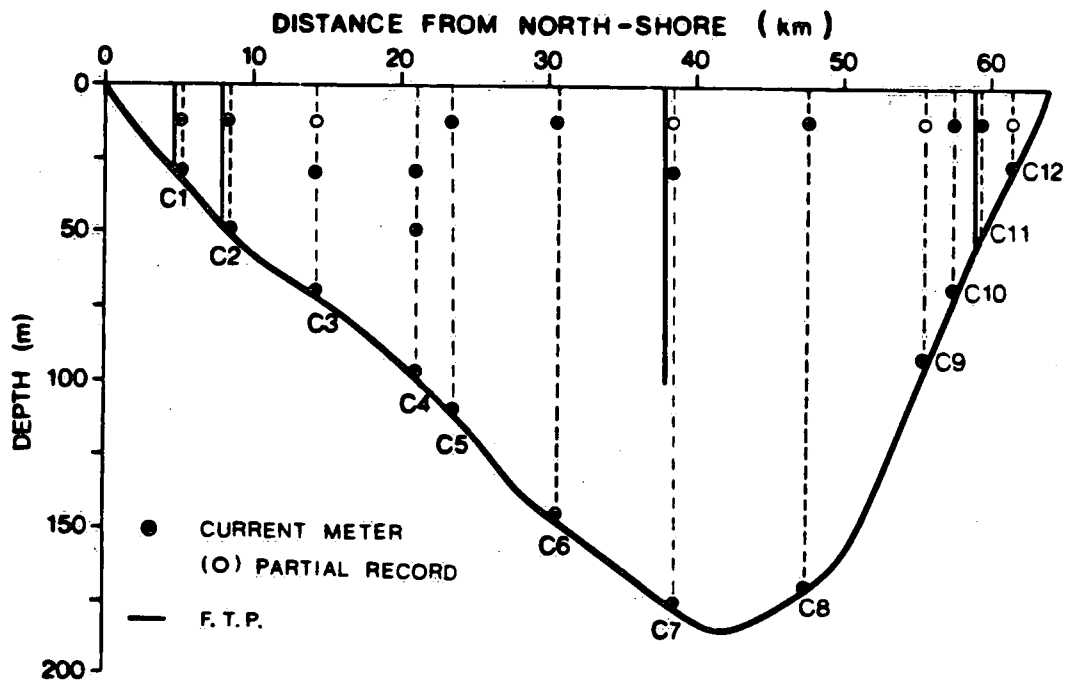
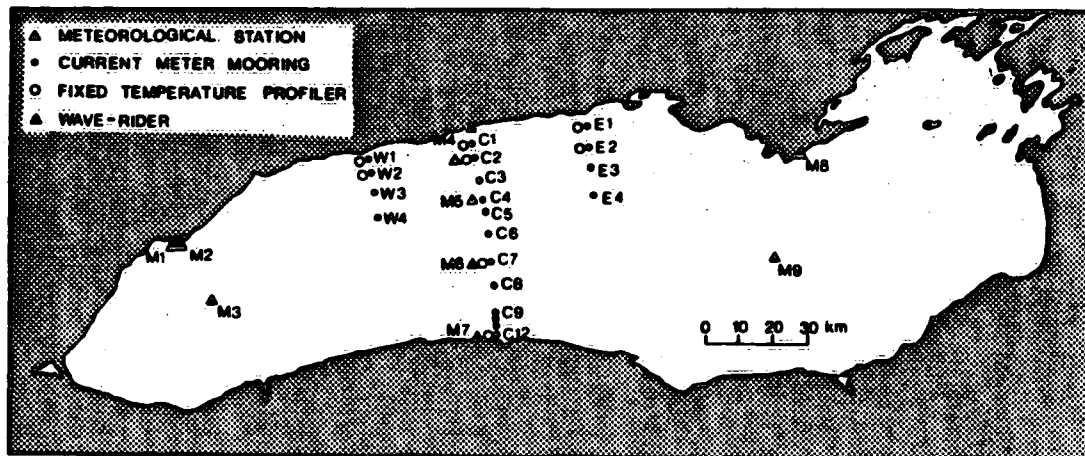


Fig. 1.1 Location of current meters, fixed temperature profilers, meteorological stations and waverider in Lake Ontario, 6 May - 30 August 1983.

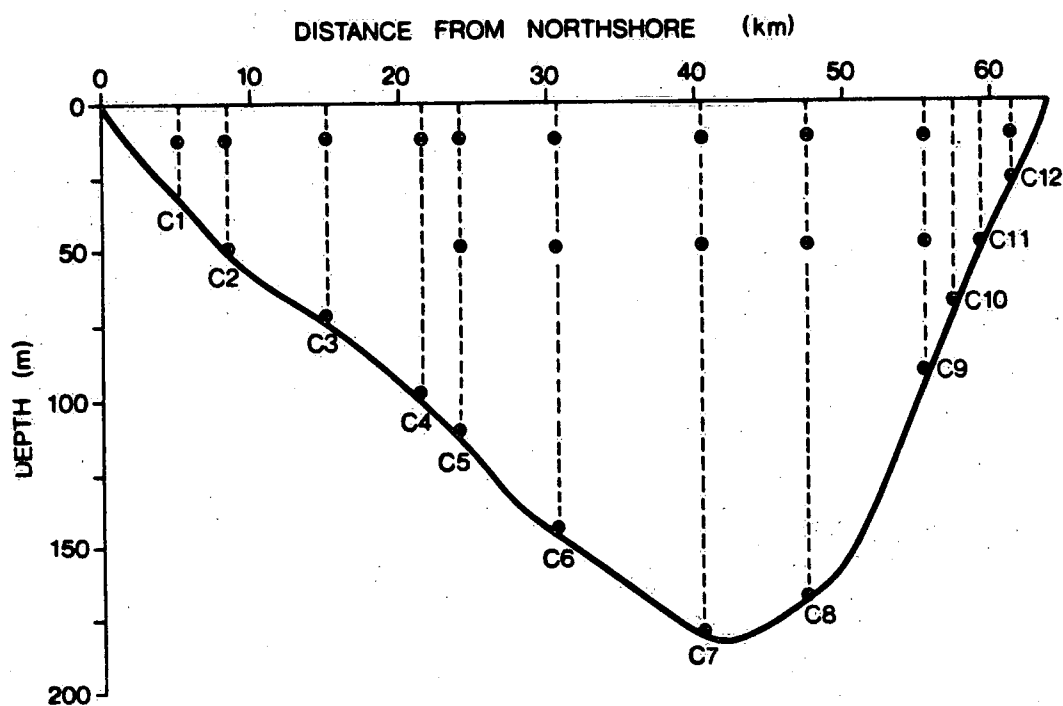
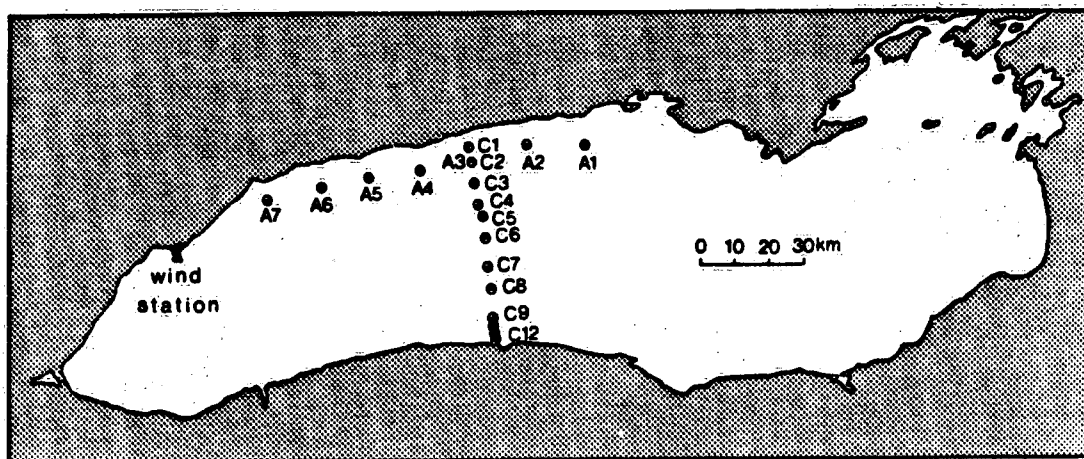


Fig. 1.2 Location of current meter moorings in Lake Ontario,  
4 November 1982 - 23 March 1983.

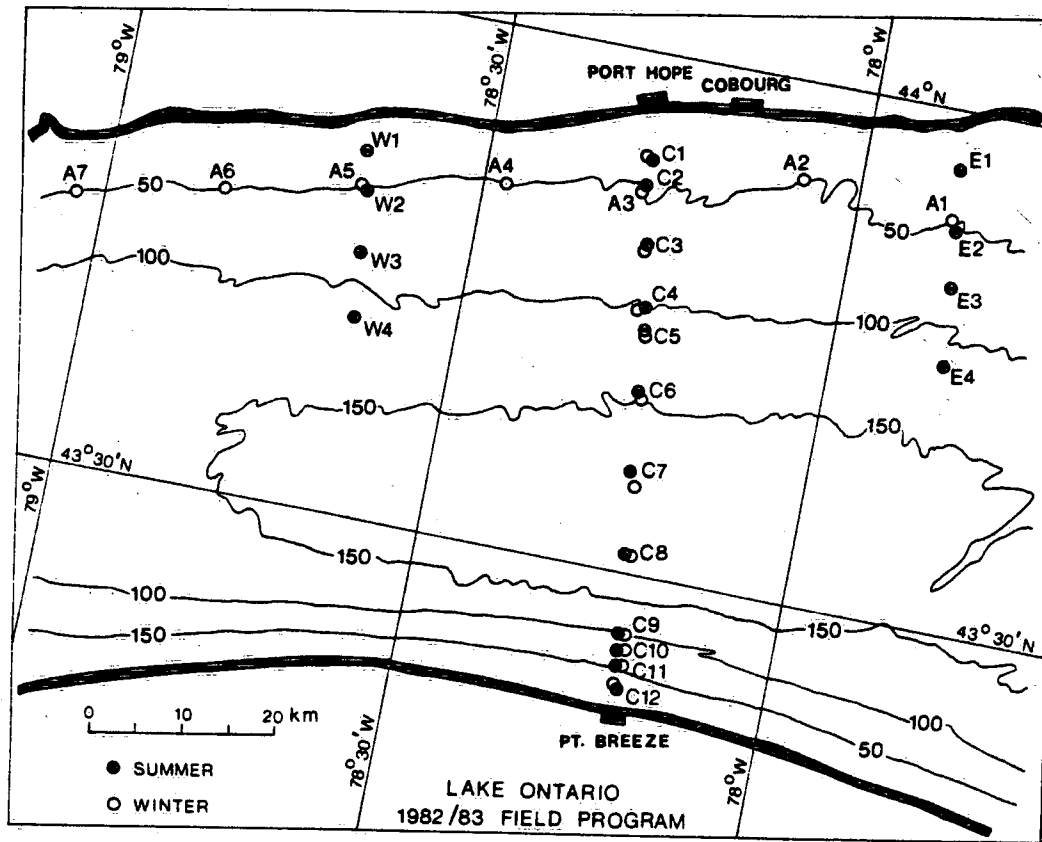


Fig. 1.3 Topography of Lake Ontario in area of 1982/83 field program.

## Summer Study: North-South Transect

### 2.1 Wind and Wind Stress

As part of the 1982 field program four meteorological buoys were deployed on Lake Ontario and four meteorological stations were established on the shoreline at Toronto, Port Hope and Point Petre, Ontario and Point Breeze, New York. In addition, routine wind observations are available from Toronto Island Airport. The locations of these stations were shown in Figure 1.1.

Since the scale of atmospheric weather patterns is typically much larger than Lake Ontario, the wind field may be expected to be rather uniform over the lake. In order to test this hypothesis, hourly values of wind speed and direction observed at each station were compared with the values measured at the central station M5. In order to eliminate doubtful wind directions at low wind speeds, comparison of directions was restricted to speeds over 3 m/s (about 10 km/hr). The results for the period of measurement, 6 May - 30 August 1982 are displayed in the form of scatter diagrams in Figures 2.1 and 2.2. In addition, deviations were computed between hourly values of wind speed and direction observed at each station and those measured at the central station. These results are presented in the form of frequency distributions in Figure 2.3.

Inspection of Figures 2.1 and 2.3 shows that the direction of the wind tends to deviate to the left in the western basin and to the right in the eastern basin. An exception is the Toronto Island station (M2) which shows a systematic clockwise deviation of wind direction from the adjacent beach station M1. The angle of deviation is about 50 degrees. With regard to the wind speeds shown in Figs. 2.2 and 2.3, the greatest deviations are observed at the Port Hope station (M4), which systematically underestimates the speed of the wind.

The wind stress at the water surface was computed in the conventional way from the square of the wind speed. The drag coefficient was taken to be  $1.2 \times 10^{-3}$  for speeds less than  $10 \text{ ms}^{-1}$ , linearly increasing from  $1.2 \times 10^{-3}$  to  $2.4 \times 10^{-3}$  for speeds between 10 and  $20 \text{ ms}^{-1}$ , and equal to  $2.4 \times 10^{-3}$  for higher wind speeds. The stresses were decomposed into alongshore and onshore components with the alongshore direction being aligned with the general orientation of the north shore of Lake Ontario ( $80^\circ$  clockwise from North). Time series of these wind stress components are presented in Figures 2.4 and 2.5. Since the present study is not concerned with short-term wind and current fluctuations, the records were smoothed by a digital filter to eliminate fluctuations with periods shorter than two days.

Power spectra and cross-spectra of wind stress were computed by the lagged covariance method with maximum lag of 23.4 days, i.e. one-fifth of the total record length of 117 days. Spectral estimates

were obtained for fractions of the maximum period of 46.8 days and smoothed by Hanning. The power spectra are presented in Figure 2.6 for both components of the stress and the sum of the components. They show a gradual decrease of energy density with increasing frequency except for a broad peak at periods of about a week. The wind energy is fairly uniform over the lake except for the Port Hope station (M4).

Figure 2.7 shows the rotary spectra of the wind. Rotary coefficients are identified by dashed lines, ellipse orientation by solid lines. According to mathematical convention, ellipse orientations are measured relative to the alongshore direction with positive values indicating counterclockwise rotation. The results indicate a clockwise shift in prevailing wind directions between the western and eastern ends of the lake. Such a curvature of the wind field is consistent with the centre of atmospheric pressure systems being located to the south of Lake Ontario. As noted earlier, the Toronto Island station (M2) shows a systematic clockwise deviation of about 50 degrees from the adjacent beach station (M1).

Figure 2.8 presents the coherence between the different stations of the meteorological network and the central station (M5). As expected, high coherences are obtained between over-water stations, including Toronto Island. The lowest coherences are found between Port Hope (M4) and the central station (M5) in spite of their proximity. Figure 2.8 also shows amplitude ratios of wind stresses as a function of frequency, again using the central station for

reference. These amplitude ratios clearly show the uniformity of wind speed over the whole lake, the drastic reduction of wind speed at Port Hope (M4), and the substantial reduction at the Toronto Beach station (M1).

## 2.2 Surface Waves

According to Donelan (1978, 1982) the wind drag at the lake surface depends on the wave field such that the form stress is large as the waves are building up and decreases once the wave field adjusts itself to the wind. In order to use this theory in models of coastal currents and lake circulation, it is necessary to compute the surface waves, since detailed observation of the wave field is clearly out of the question. Donelan (1977) developed a wave prediction scheme and was successful in hindcasting observed waves on Lake Ontario. The same model was tested by Schwab et al. (1984) against Lake Erie data. In the present study, the model will be verified against the wave observations at station C2 (Fig. 1.1).

Numerical wave prediction models may be divided into two classes: spectral or parametric. Spectral models deal with discrete frequencies of the energy spectrum, while parameter models assume a certain spectral shape and predict a few wave parameters such as characteristic wave height and peak period. In general, both types of models are based on energy considerations. The model developed by

Donelan (1977) belongs to the class of parameter models but it computes wave momentum instead of energy transport. It also allows for a fossil wave field left behind by a rapidly changing wind. For a discussion of the model, the reader is referred to Donelan (1977) and Schwab et al. (1984).

The model predicts the wave field from the wind field at each point of a two-dimensional grid covering the whole lake. For the present application a 20-km grid was used and the model was driven by hourly winds observed on the lake (Fig. 1.1). The model was run continuously for the period 8 May to 29 August 1982, and the results at the location of station C2 (Fig. 1.1) were compared with local wave observations at three-hour intervals.

Time series of computed and observed values of significant wave heights and peak periods are compared in Figs. 2.9 and 2.10. Table 2.1 presents statistical comparisons. The correlation coefficient for wave heights is 0.84, as compared to values ranging between 0.88 and 0.93 found by Schwab et al. (1984). The slope of the linear regression of computed on observed heights is 0.86, as compared to values of 0.68 - 0.99 found by the above authors. While this would suggest that the model underestimates the heights of the waves, it should be noted that regression of observed on computed heights gives a slope of 0.82, thus implying that the model overestimates wave heights. Indeed, as measured by the slope of the maximum likelihood estimate, the ratio of computed to observed wave heights is 1.03,



which indicates that the wave heights are accurately predicted (see Fig. 2.9).

The measurements of wave periods exclude periods shorter than two seconds. Therefore, the cases when the computed periods were less than two seconds were excluded from the statistical computations of Table 2.1. The correlation coefficient of 0.75 may be compared with values of 0.72 - 0.81 found by Schwab et al. (1984), while the slope of the linear regression of computed on observed peak periods is 0.57 as compared to values of 0.69 to 0.77 found by these authors. On the other hand, regression of observed on computed periods gives a slope of 0.98. As a result, the maximum likelihood estimate has a slope of 0.70, which indicates that the wave periods are underestimated (see Fig. 2.10).

Figure 2.11 presents scatter diagrams of computed wave bearing against wind bearing, computed against observed wave heights and computed against observed wave periods. The upper right-hand corner of the same figure shows a frequency distribution of wind bearings. Since the quality of the wave predictions may depend on the wind direction relative to the adjacent shore, the model results were analysed separately for 45 degree sectors of wind direction. The corresponding regression coefficients are displayed on the right in Figure 2.11. Above-average correlations with measurements are obtained for south-easterly winds (bearing 240-330 degrees), which indicates that model performance improves with fetch.

**Table 2.1 Comparison of computed and observed wave heights and peak periods, Lake Ontario, 8 May - 29 August 1982**

	Wave Height	Peak Period
	(m)	(s)
Number of data points	589	367
Observed mean	.26	3.28
standard deviation	.23	.81
Computed mean	.34	2.84
standard deviation	.24	.62
Correlation coefficient	.84	.75
Linear regression:		
Computed vs observed	{ slope	.86 .57
	{ intercept	.12 .96
Observed vs computed	{ slope	.82 .98
	{ intercept	-.02 .50
Maximum likelihood	{ slope	1.03 .70
(computed vs observed)	{ intercept	.07 .54

### 2.3 Temperature

This section is concerned with temperature distributions in a north-south cross section of Lake Ontario from early May to late August, 1982. For that period, continuous time series of temperatures are available from four fixed temperature profilers and 24 current meters in the transect between Port Hope and Point Breeze (Fig. 1.1). In addition, satellite observations of surface temperature are available for days with clear skies. A sample of such observations is presented in Figures 2.12 - 2.13. Time variations of the 10-degree isotherm measured by the fixed temperature profilers at the north shore, mid-lake and south shore, respectively, are shown at the bottom of Figure 2.14. The top of Figure 2.14 shows the eastward component of the wind stress. Since the surface transport tends to be to the right of the wind, the east-west component of the wind is primarily responsible for upwelling and downwelling along the north and south shores. It is apparent from Figure 2.14 that, at opposing shores, the thermocline moves in opposite directions in response to the wind.

In order to describe the stratification cycle, two-day averaged temperature distributions were prepared for the north-south cross section of Lake Ontario. The procedure consisted of two steps. First, vertical temperature profiles were constructed at the location of the current meters by recourse to profiles measured by nearby fixed temperature profilers. These additional profiles are identified by

dashed lines in Figure 2.15 where, as in Figure 1.1, fixed temperature profilers are shown by solid lines and current meters by black circles. Figure 2.15 also shows the location of five stations where biochemical surveys were carried out during 1982.

The additional temperature profiles at the location of the current meter moorings were obtained by adopting the shape of the profile measured by an adjacent temperature profiler and shifting this profile up or down to match the temperatures measured by the current meters. A total of ten vertical temperature profiles were thus obtained for the cross section.

The next step was to interpolate the temperature horizontally between temperature profiles. This was done at vertical intervals of 1 m between the surface and the 30 m level, using an objective computer routine. Figures 2.16 - 2.22 show the resulting temperature distributions in the form of isotherms at two-degree intervals. For easy reference, the five biochemical stations are indicated by triangles on the horizontal axis at the bottom.

As seen in Figure 2.16, the start of the measurement program coincided with the onset of the thermal bar episode at the north shore. By the middle of May, the north-shore water became stratified and by the end of May (Fig. 2.17) the same happened at the much steeper south shore. During the month of June (Figs. 2.17 - 2.18) the stratification in the shore zones increased gradually, but the open lake remained colder than 4 degrees and hence continued to be fully mixed in the vertical.

Superimposed on the gradual increase of stratification, periodic temperature fluctuations occurred in the shore zones due to wind reversals. In the latter part of June the weather was dominated by a series of strong winds from westerly directions (Fig. 2.14). The resulting Ekman drift to the south caused upwelling of cold water at the north shore and accumulation of warm water at the south shore. Apparently, the forcing was so persistent that the warm north-shore water became separated from the shore and eventually reached the centre of the lake (Fig. 2.19). At this time, a narrow strip of the lake was still fully mixed, thus separating the epilimnion in the northern half of the lake from the warm water along the south shore (see also bottom of Fig. 2.12). This belt of cold water quickly disappeared, and by the middle of July (Fig. 2.20 and top of Fig. 2.13) the thermocline was fully established over the whole lake.

During the month of August, temperature variations were dominated by a few wind events. In early August (Fig. 2.21) persistent winds from easterly directions gradually depressed the thermocline on the north shore. A sharp wind reversal on August 9 (see Fig. 2.14) caused the thermocline to rise to the surface at the north shore and dip below 30 m along the south shore (bottom of Fig. 2.21). At this time, satellite observations (middle of Fig. 2.13) show a band of cold water extending along the entire north shore, with warm water covering the southern and eastern regions. When the wind died down, the pattern of cold and warm water started moving around the lake in counterclockwise direction. The dynamics of this

phenomenon will be addressed in Chapter 3 of this report. On August 25 - 26 the peak of the warm water wave passed through the northern part of the cross section as seen at the bottom of Figure 2.22 and the bottom of Figure 2.13.

#### 2.4 Currents

This section presents the currents observed in the north-south cross section of Lake Ontario during the summer of 1982. For the location of the current meter moorings, reference is made to Figure 1.1 and Table 1.1. All currents were decomposed into alongshore and onshore components, with the alongshore orientation being 80° clockwise from north. Alongshore currents are positive to the east and cross-shore currents are positive to the north. Since the present study is not concerned with short-term fluctuations, the time series were smoothed by a digital filter to eliminate periods shorter than two days.

Figure 2.23 shows the alongshore components of all bottom currents measured in the north-south array. For easy reference the alongshore wind stress at station M5 is presented at the top of each of the following figures. According to the temperature records, the bottom current meters were all situated in the hypolimnion ( $T < 6^{\circ}\text{C}$ ) except the last one, which on occasion was affected by downwelling of epilimnion water along the south shore. Except for these episodes (indicated by dashes in the last time series), there is good coherence

between adjacent current meter records. Apparently, the north-south variation of currents in the hypolimnion generally displays three regimes. For water depths less than 100 m near both shores, the currents tend to be strongly correlated with the wind, while in mid-lake the currents generally flow in opposite directions. Such currents are also observed during the fall and winter season and will be explained in Chapter 4.

Figure 2.24 shows hypolimnion currents at different levels for three moorings. It is seen that the currents are quite uniform in the vertical, including the currents measured 1 m above the bottom.

Figure 2.25 shows alongshore components of all currents observed at the 10-m level in the north-south array. Again nearshore currents are strongly correlated with the wind, but effects of stratification became apparent later in the season. These effects are more clearly illustrated in Figures 2.26 - 2.28. The first of these figures shows surface observations of temperature and currents (solid lines) together with bottom observations (dashed) for deep-water moorings. As soon as stratification develops, the surface currents are seen to deviate from the bottom currents. The actual unfiltered records of surface currents show large and persistent inertial motions after the onset of stratification.

Figure 2.27 presents surface (solid lines) and bottom (dashed lines) observations of temperature and alongshore currents near the north shore. The most conspicuous events are two downwelling

episodes in August with large westward currents in the upper layer. Each downwelling episode is followed by upwelling with eastward currents. Note that the westward currents show a large vertical shear, while the eastward currents are quite uniform in the vertical. The reason is that in the first case the thermocline is located between the top and bottom current meters, while during upwelling both meters are located in the hypolimnion.

Figure 2.28 shows surface (solid) and bottom (dashed) observations of temperature and alongshore currents near the south shore. In contrast to the north shore, the south-shore currents are generally directed toward the east. This can be traced back to the thermal bar episode which is known to be associated with a counter-clockwise circulation around the perimeter of the lake. In addition, the south-shore currents generally show large vertical shears because the upper meter is located in warm water and the bottom meter in the hypolimnion. During a few downwelling events in August, the bottom meter of the nearshore mooring is seen to end up above the thermocline.

Turning to the cross-shore components of the currents, Figure 2.29 shows results from all bottom measurements in the north-south array. Again in this figure and the following, the alongshore wind stress is included because this component is mainly responsible for the cross-shore as well as alongshore components of the currents in the present cross section of Lake Ontario. The



reasons for that will be touched upon at various places in the following chapters of this report. Note that the scale of the cross-shore current plots is twice as large as that of the alongshore currents shown earlier. Thus, the onshore-offshore currents are generally weaker than the alongshore components, especially in the shore zones.

Figure 2.30 shows that the currents are uniform in the vertical below the thermocline, while Figure 2.31 shows the effects of stratification on the vertical current structure in deep-water stations. Figures 2.32 and 2.33 present surface (solid) and bottom (dashed) measurements of temperature and cross-shore currents in the shore zones. Unlike the corresponding results for alongshore currents, the relation between temperature and onshore-offshore currents is not always apparent, especially at the north shore. At the south shore, however, downwelling of warm water in August is clearly correlated with shoreward surface current.

An interesting display of lake circulation is provided by the distribution of currents in a cross section such as the section between Port Hope and Point Breeze. In order to obtain this, the currents were interpolated in the same manner as the temperatures. Although no continuous vertical profiles of currents were measured, they may be inferred from the temperature profiles. In the absence of stratification, currents must be quite uniform in the vertical, and the same holds true below the thermocline during the stratified season.

Between the thermocline and the free surface, vertical variations of currents may also be expected to be relatively small, and hence the major shearing currents are concentrated around the thermocline. Thus, on occasions when the thermocline depth exceeds 10 metres, the upper current meter provides an estimate of the epilimnion current, while the bottom current meter measures the hypolimnion current. The transition from upper to lower layer current may be taken to match the temperature profile. Once the vertical current profile has been established for each mooring, horizontal interpolation is readily accomplished.

The lower half of Figure 2.34 shows monthly averages of the component of the current normal to the Lake Ontario cross section between Port Hope and Point Breeze. The units are km/day and positive values represent eastward currents; negative currents run westward. The cross-sectional distribution of currents averaged over the whole measurement period is shown at the top of Figure 2.35. The bottom of Figure 2.35 presents the north-south variation of the corresponding water transport. This was obtained by integrating the currents over depth.

The total flow of water through a cross section of a closed lake must vanish when averaged over periods of a few days or longer. For Lake Ontario, the total transport should be equal to the average flow from the Niagara to the St. Lawrence River. When the present results are averaged over the whole period of the experiment, as in

Figure 2.35, the total transport is found to be  $10 \times 10^3 \text{ m}^3/\text{s}$  to the east, which compares favourably with the Niagara discharge of  $7 \times 10^3 \text{ m}^3/\text{s}$ . Similar eastward transports are found for the months of June and August (Fig. 2.34). However, the net transport for July is two-to-three times as large, while the net transport during May is westward. Fortunately, these errors can be most likely attributed to inaccuracies in the deep lake currents which are too small to be accurately observed but make significant contributions to the total water transport because of the large water depths.

The most interesting aspects of Figures 2.34-2.35 are the persistent boundary currents near the two shores. Along the south shore, the water flows from west to east with surface velocities of 5-10 km/day. On the north shore, the water flows from east to west. The boundary currents can be traced back to the thermal bar episode which is known to be associated with counterclockwise circulation around the perimeter of the lake. Although affected by a few summer storms, the currents appear to persist throughout the season.

## 2.5 Response of Lake to Wind

In order to illustrate the response of Lake Ontario to wind impulses, detailed descriptions of temperature and currents will be presented for three periods coinciding with biochemical cruises in July and August. The periods are June 29-July 2, August 10-13 and

August 24-27. The overall temperature distributions in Lake Ontario during these periods are illustrated by the satellite pictures of Figures 2.12 - 2.13. During the first period, the deep-lake station is just getting stratified and winds from westerly directions result in upwelling of cold water at the north shore. The second period is dominated by three days of strong winds from the west again causing upwelling along the whole north shore. By the time of the third period, the cold north shore water has drifted into the western basin due to dynamical processes discussed later in this report.

Day-to-day variations of temperature and currents for each period are shown in Figures 2.36 - 2.38. The upper part of each figure presents temperature distributions for the Lake Ontario cross section between Port Hope and Point Breeze. These results were obtained by the same procedure used for the two-day averages shown before. In this case the biochemical stations are identified by vertical lines. The lower part of each figure shows currents measured at the 10-m level (solid arrows) and the bottom (dashed arrows). The arrows represent daily water displacements for an observer looking down on the lake such that west is on the left and east is on the right. The thin irregular lines represent stretches of the north and south shore, with black circles indicating the location of Port Hope and Point Breeze, respectively. In order to facilitate comparison with the temperature distributions, the current meter positions are shown by black circles in the temperature maps.

In the course of the first period, an eastward wind starts blowing over the lake, as shown at the top of Figure 2.14. The initial effect of such a wind is to move water to the east end of the lake such that the surface will slope down against the wind. The subsequent currents result from the counteracting effects of wind and surface slope. The surface slope creates a pressure gradient which is not affected by the depth of a water column. However, the wind stress is much more effective in moving shallow water than deep water. Since, as noted earlier, the total transport through a cross section of a closed lake must vanish, the net result of these opposing forces is that the shallow nearshore water moves in the direction of the wind while the mid-lake water returns against the wind. This explains the generation of eastward currents along both shores in Figure 2.36. Near the north shore the currents are weaker and more uniform than at the south shore. The reason is that the north-shore stratification is weakened by upwelling and hence the wind forcing can be mixed down to accelerate the whole water column. By contrast, the south-shore water is strongly stratified and the wind drives only the relatively thin upper layer. In addition, the surface currents are seen to be more southward than the bottom currents. This agrees with Ekman theory, which predicts surface drift to the right of the wind resulting in upwelling at the north shore and downwelling at the south shore.

During the second episode the wind blows again to the east and hence the lake reacts in the same way as before. However, in this

case the wind stops in the middle of the four-day period and, consequently, the thermocline starts returning to its original position. This is particularly noticeable on the south shore. Near the north shore, a broad band of eastward currents is observed on August 11, but the speeds decrease rapidly after the storm and the currents reverse themselves two days later. At the south shore strong eastward currents are generated which again are confined to the wedge of warm water. At the peak of the storm the thermocline is depressed below the level of the bottom current meter in the mooring adjacent to the south shore. This explains the large dashed arrows pointing to the east in that location.

The final episode is affected by two wind events, a short but strong westward wind impulse on August 25 followed by eastward winds on August 26. At first glance, this sequence of events might seem to explain the initial downwelling and westward flow along the north shore and the subsequent upwelling and current reversal. However, it will be shown in the next chapter that these events are caused primarily by the passage of a warm water wave. Indeed, near the south shore the wind seems to have little effect and a strong eastward current persists throughout this episode.

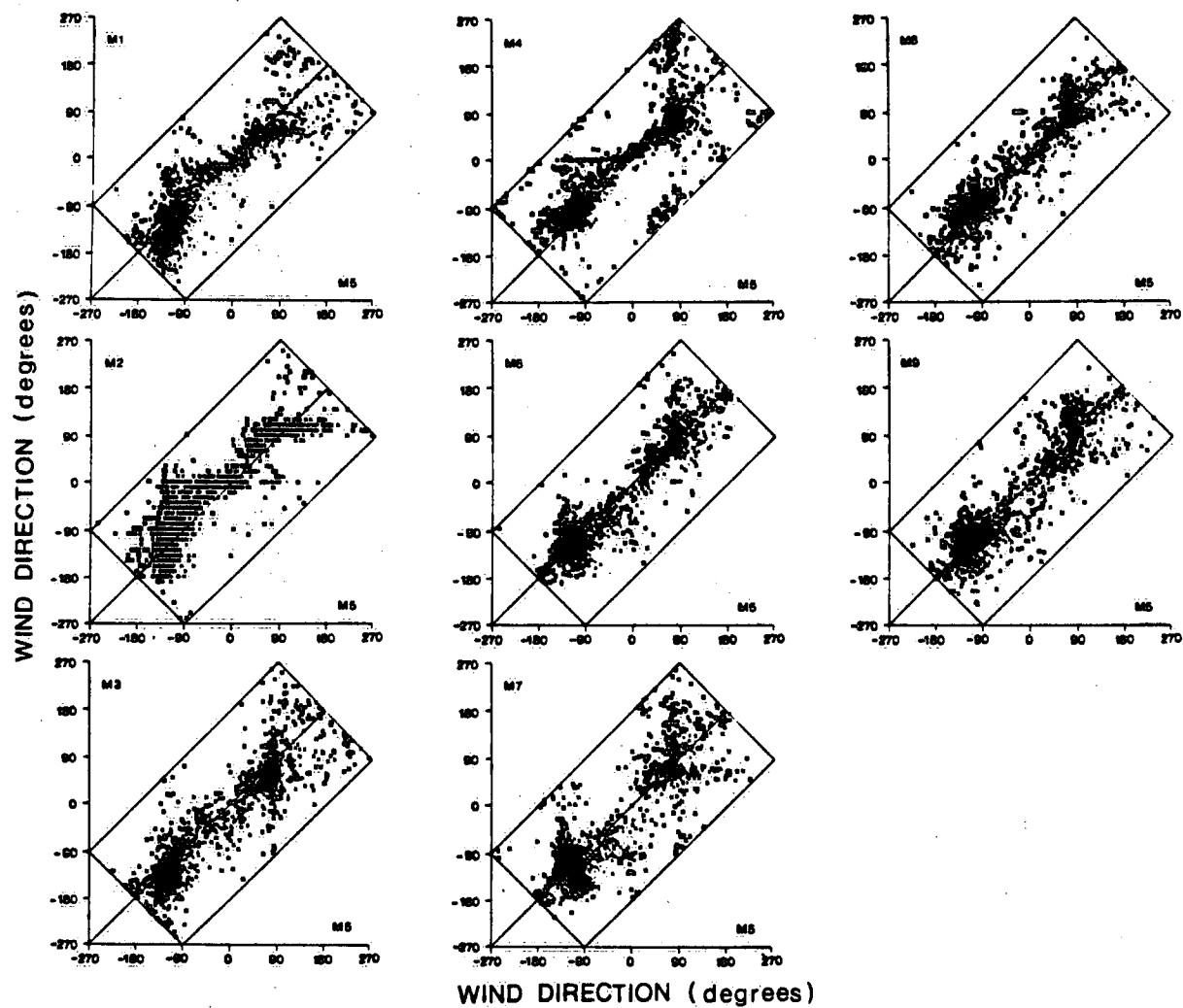


Fig. 2.1 Comparison of hourly wind directions from the meteorological network on Lake Ontario, 6 May - 30 August 1982.

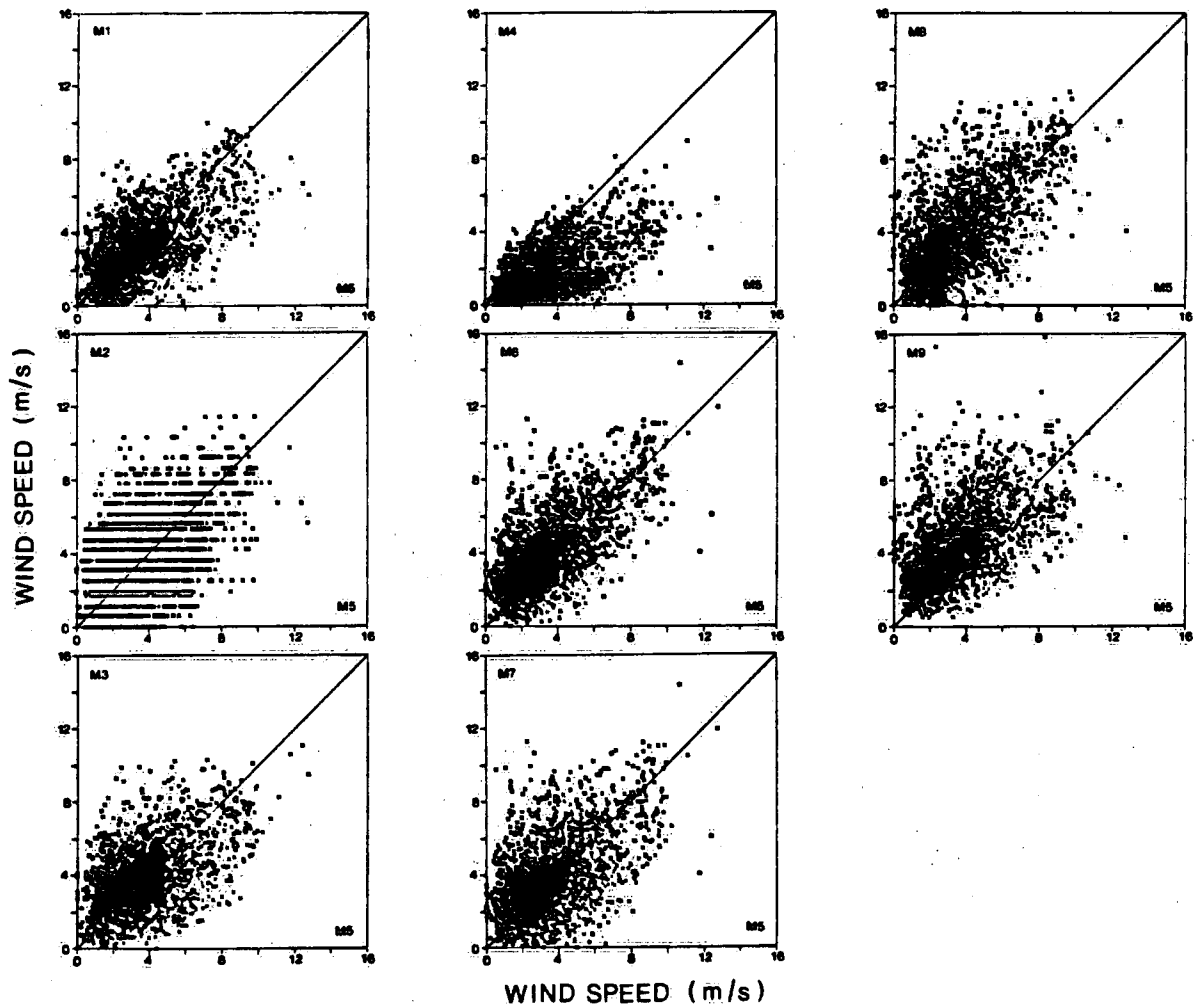


Fig. 2.2 Comparison of hourly wind speeds from the meteorological network on Lake Ontario, 6 May - 30 August 1982.



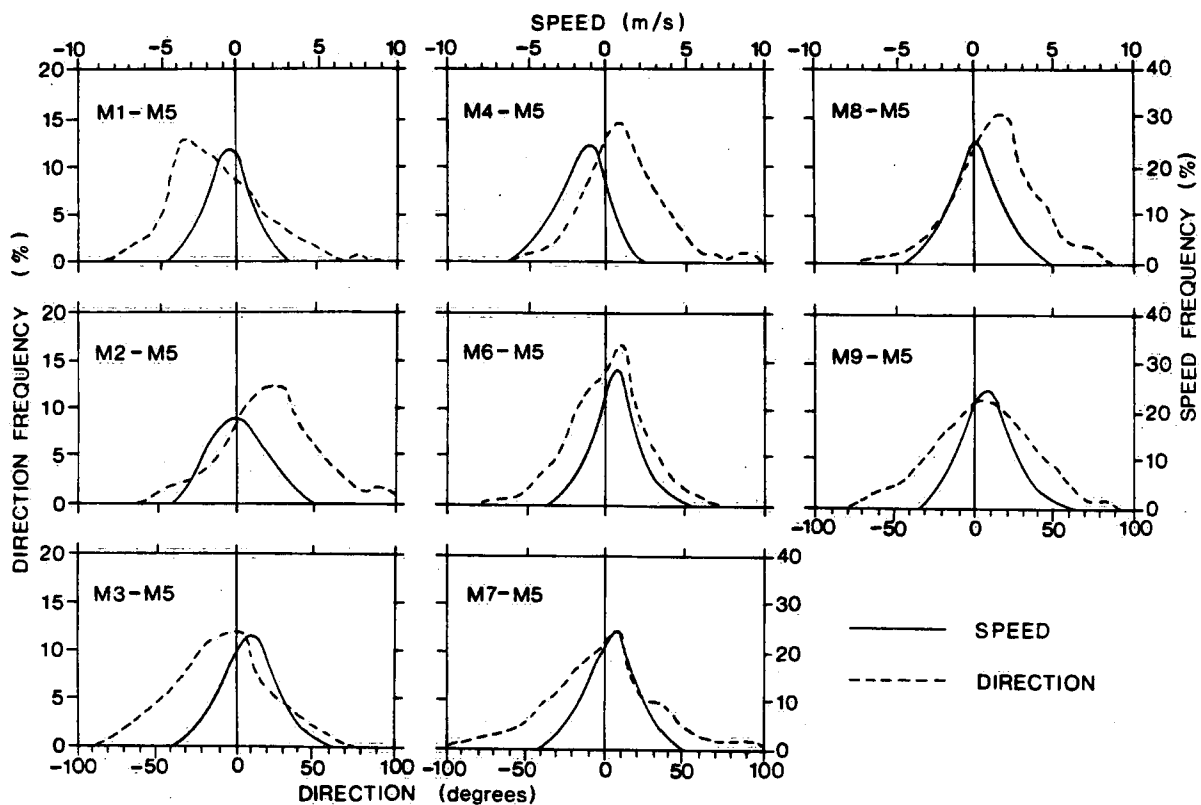


Fig. 2.3 Frequency distributions of wind deviations between different stations on Lake Ontario, 6 May - 30 August 1982.

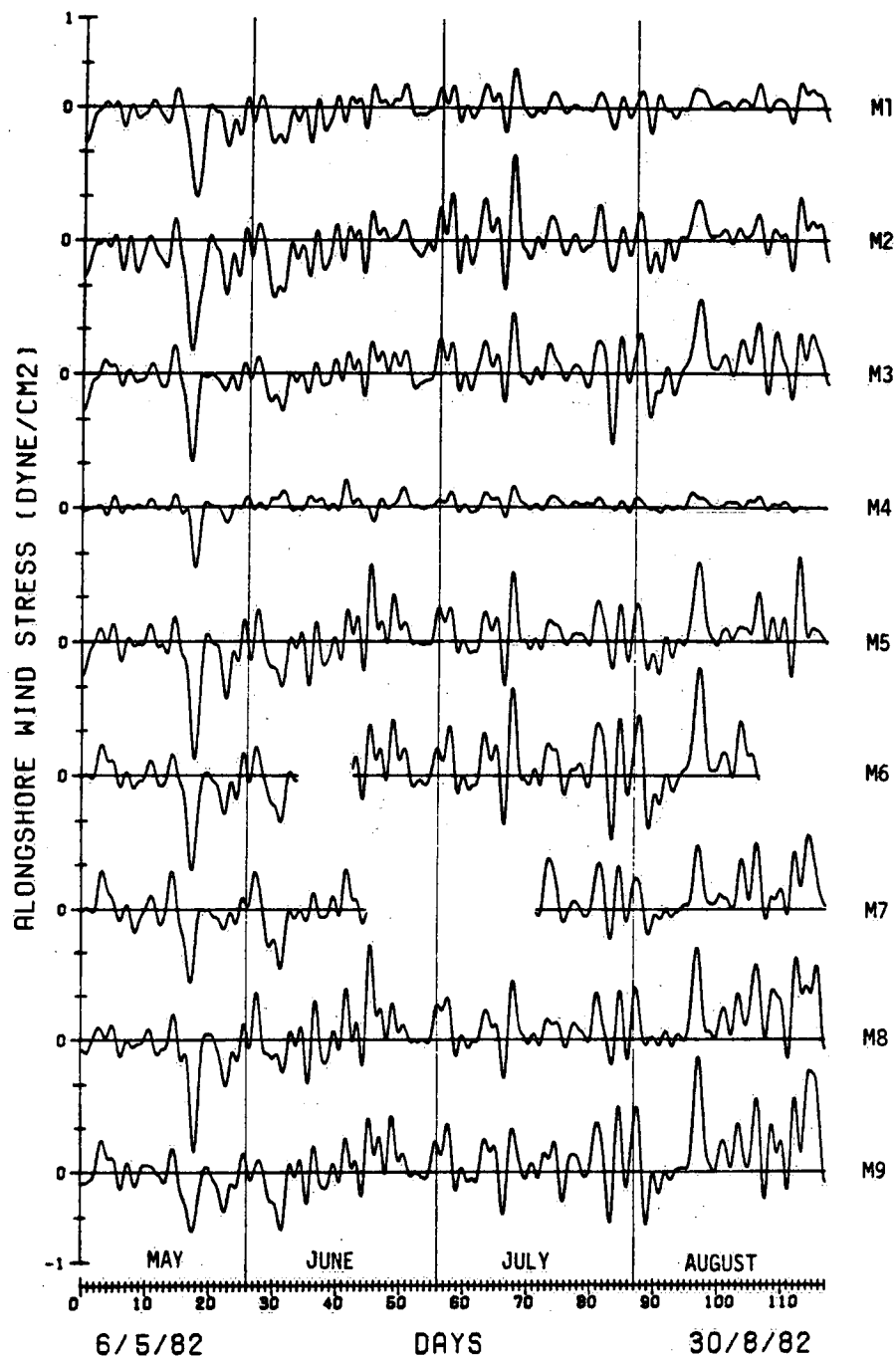


Fig. 2.4 Alongshore component of wind stress, filtered to remove periods shorter than two days.

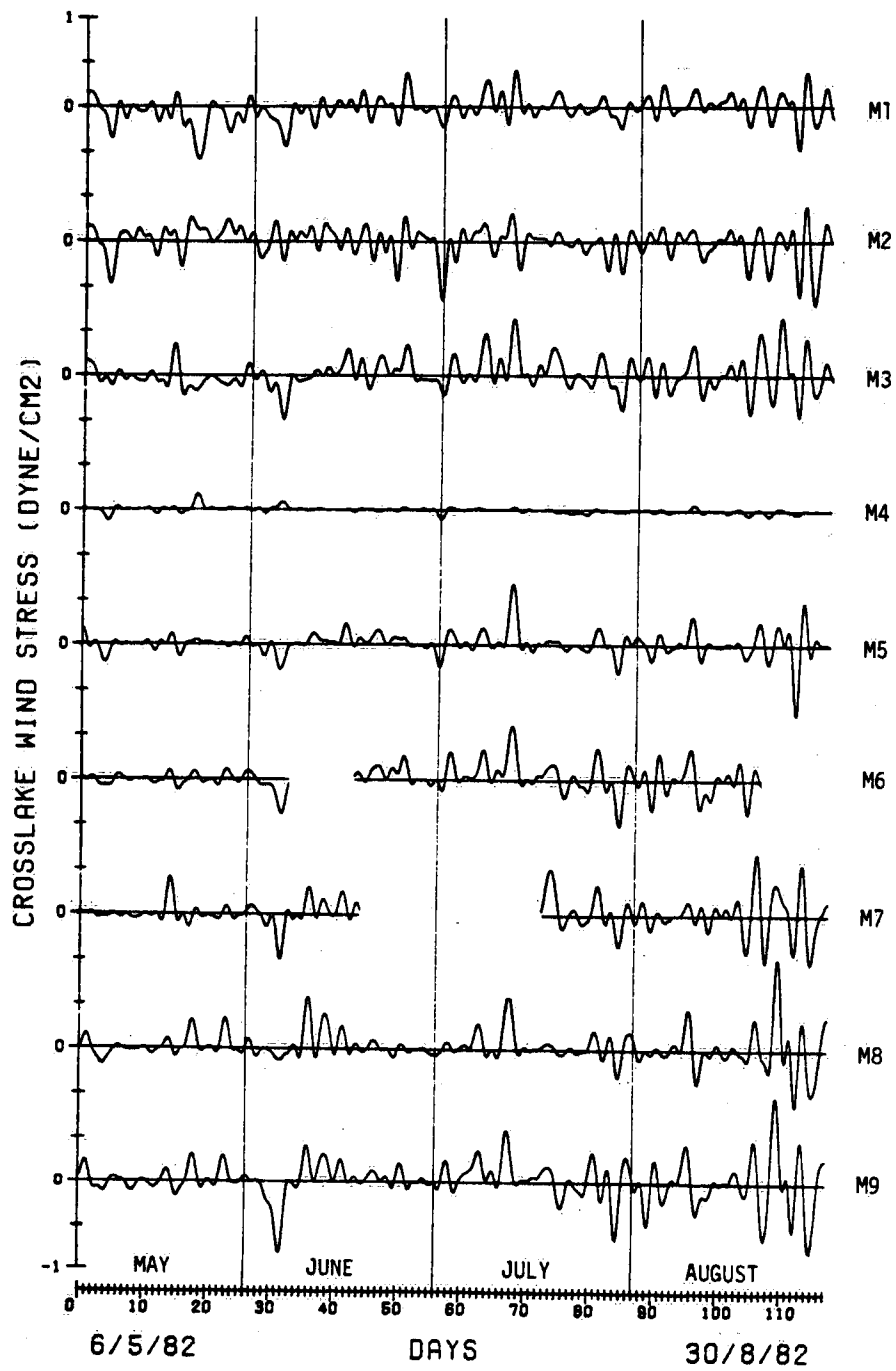


Fig. 2.5 Onshore component of wind stress, filtered to remove periods shorter than two days.

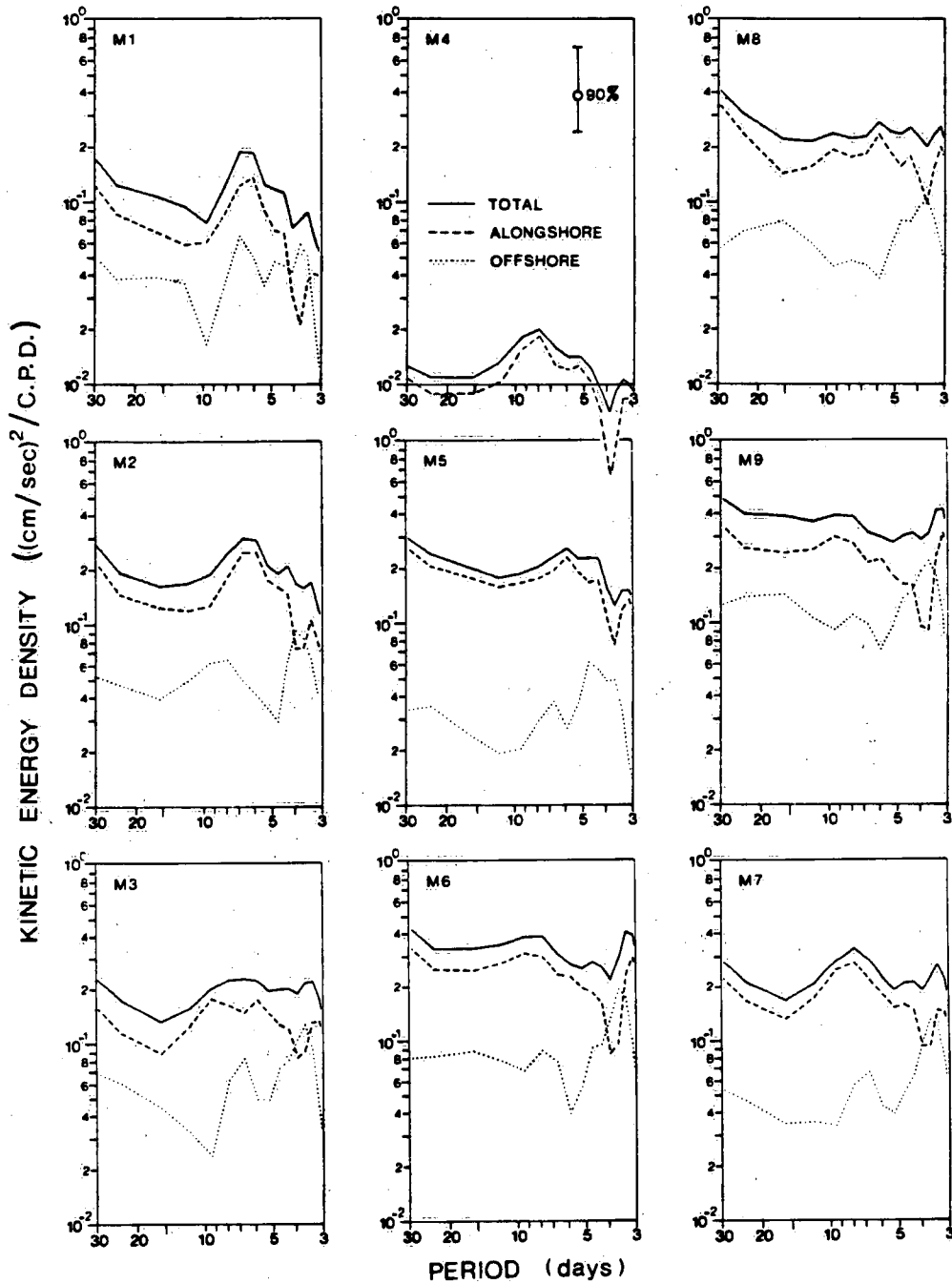


Fig. 2.6 Energy spectra of wind stress, 6 May - 30 August 1982.

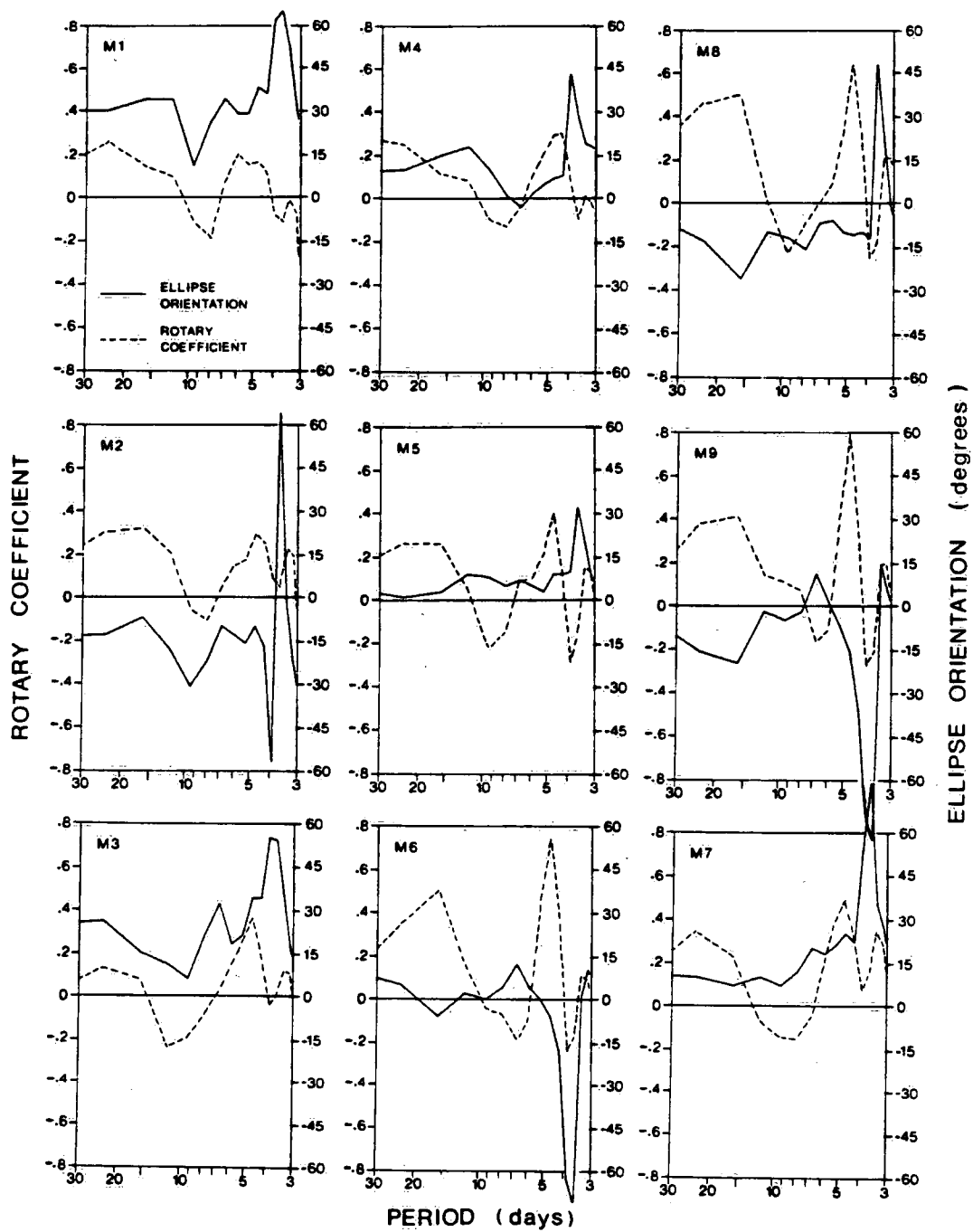


Fig. 2.7 Rotary coefficients and ellipse orientation of wind spectra, 6 May - 30 August 1982.

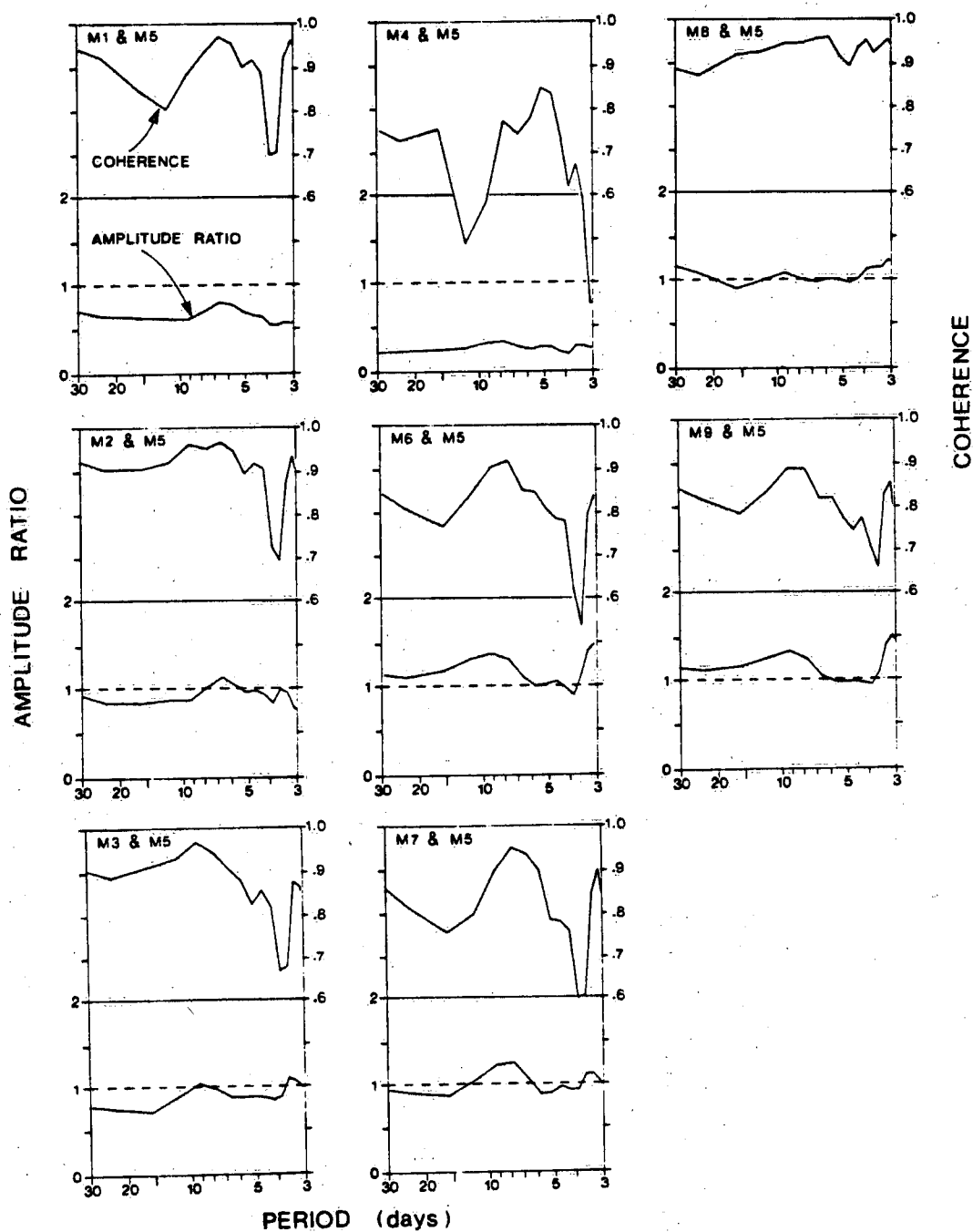


Fig. 2.8 Coherence and amplitude ratio between different wind stations on Lake Ontario, 6 May - 30 August 1982.

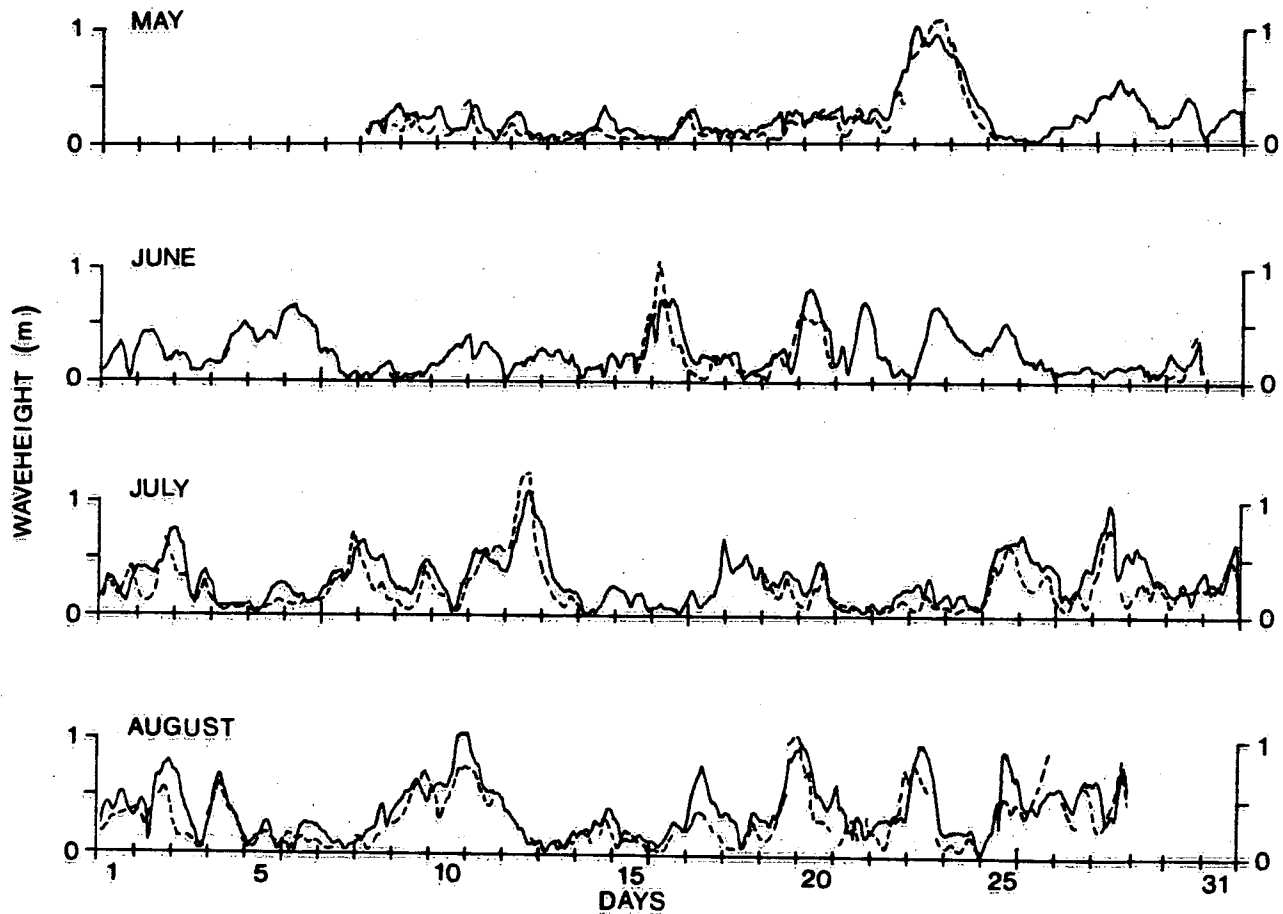


Fig. 2.9 Observed (dashed) and computed (solid) wave heights at location of waverider on Lake Ontario in 1982 (see Fig. 1.1).

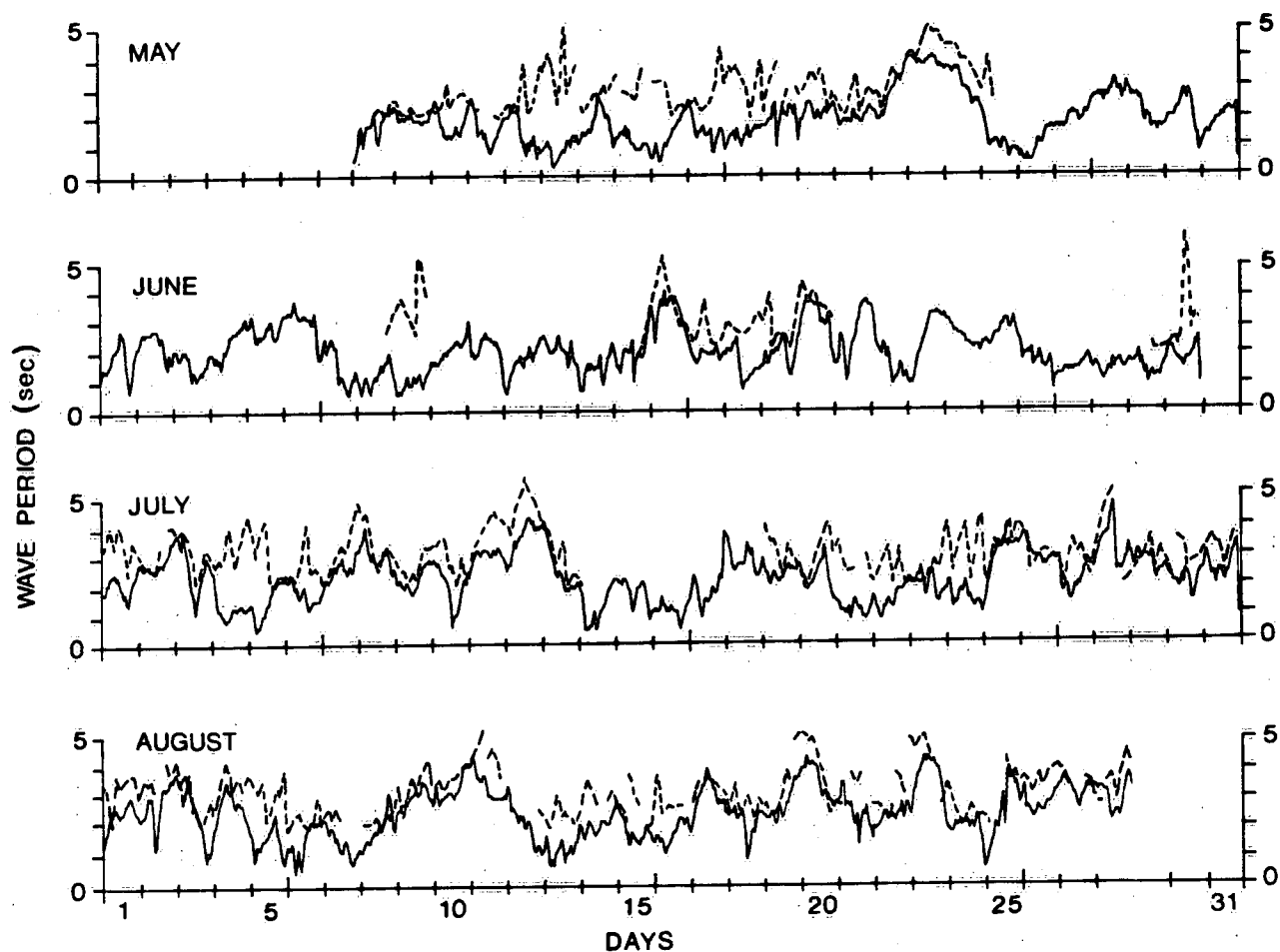


Fig. 2.10 Observed (dashed) and computed (solid) wave periods at location of waverider on Lake Ontario in 1982 (see Fig. 1.1).



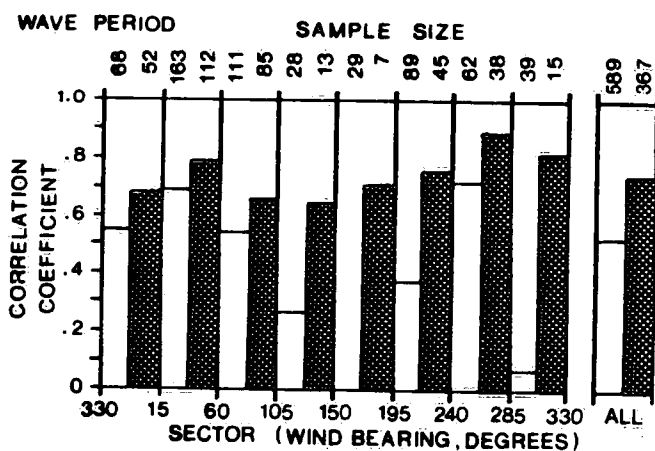
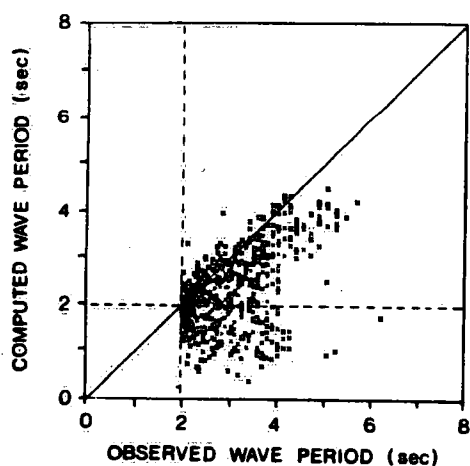
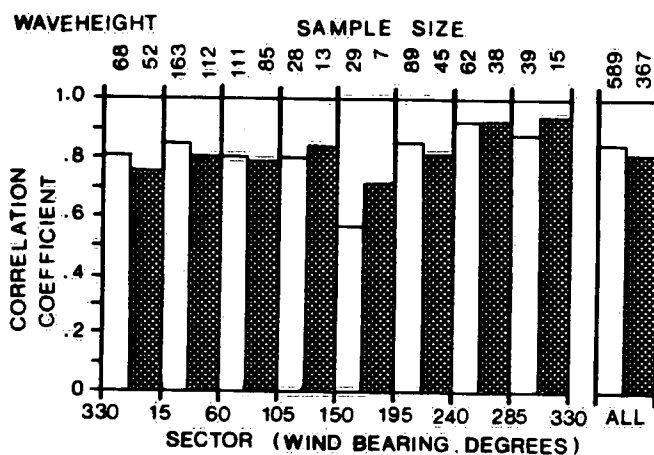
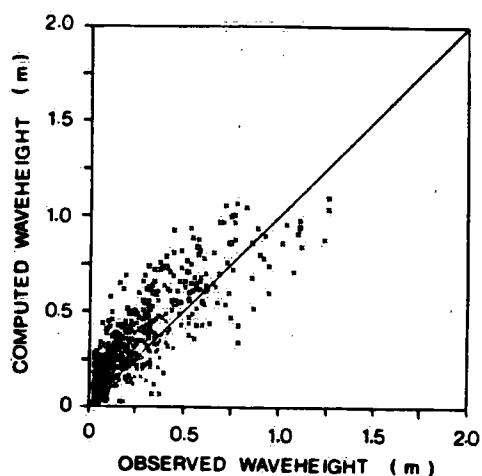
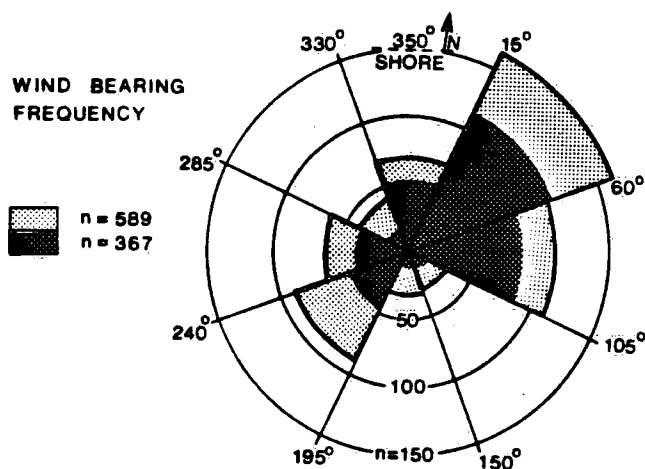
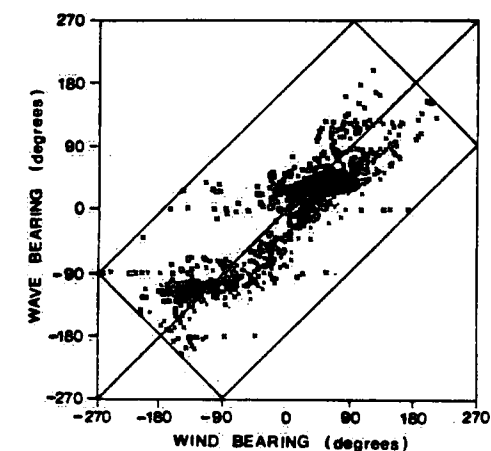
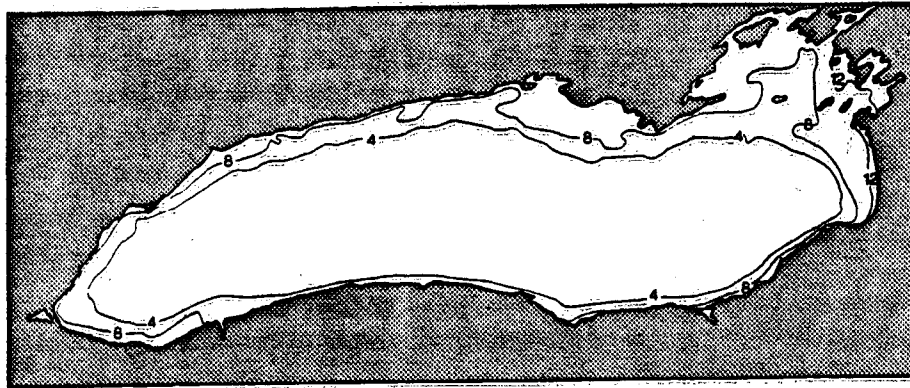
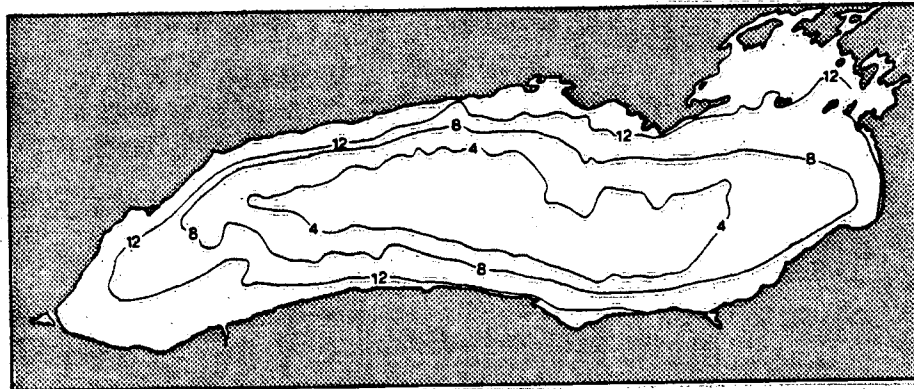


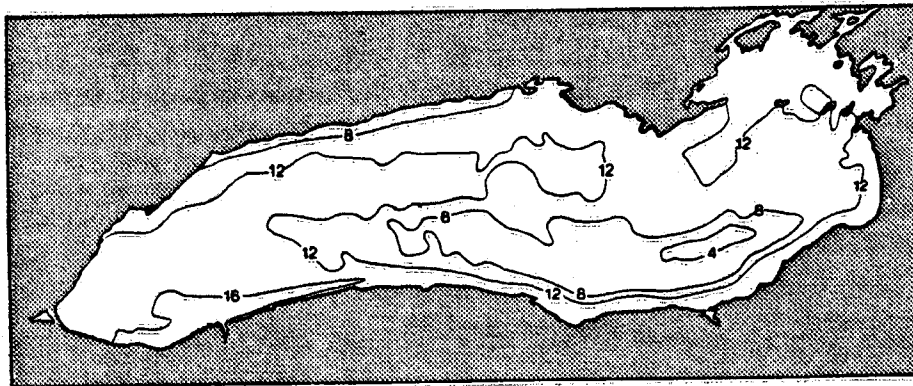
Fig. 2.11 Summary of results of wave predictions for Lake Ontario,  
8 May - 28 August, 1982. For explanation see text.



MAY 21, 1982 (1400 GMT)

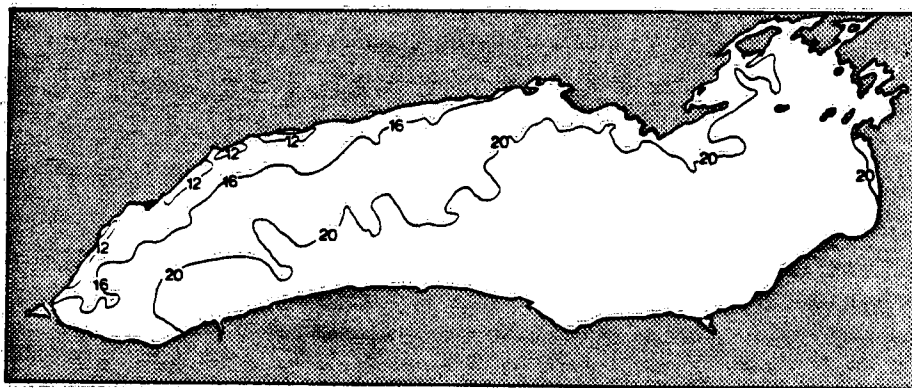


JUNE 17, 1982 (2000 GMT)

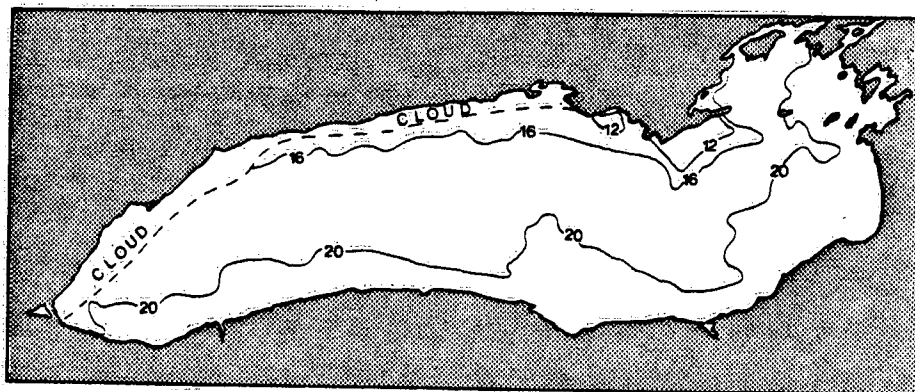


JULY 1, 1982 (0900 GMT)

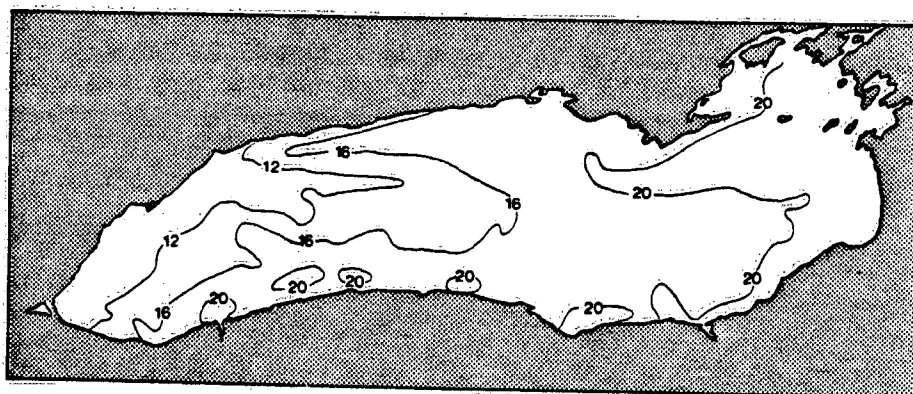
Fig. 2.12 Satellite observations of surface water temperatures in Lake Ontario, summer 1982.



JULY 21, 1982 (0800 GMT)



AUGUST 11, 1982 (1900 GMT)



AUGUST 26, 1982 (0800 GMT)

Fig. 2.13 Continuation of Fig. 2.12.

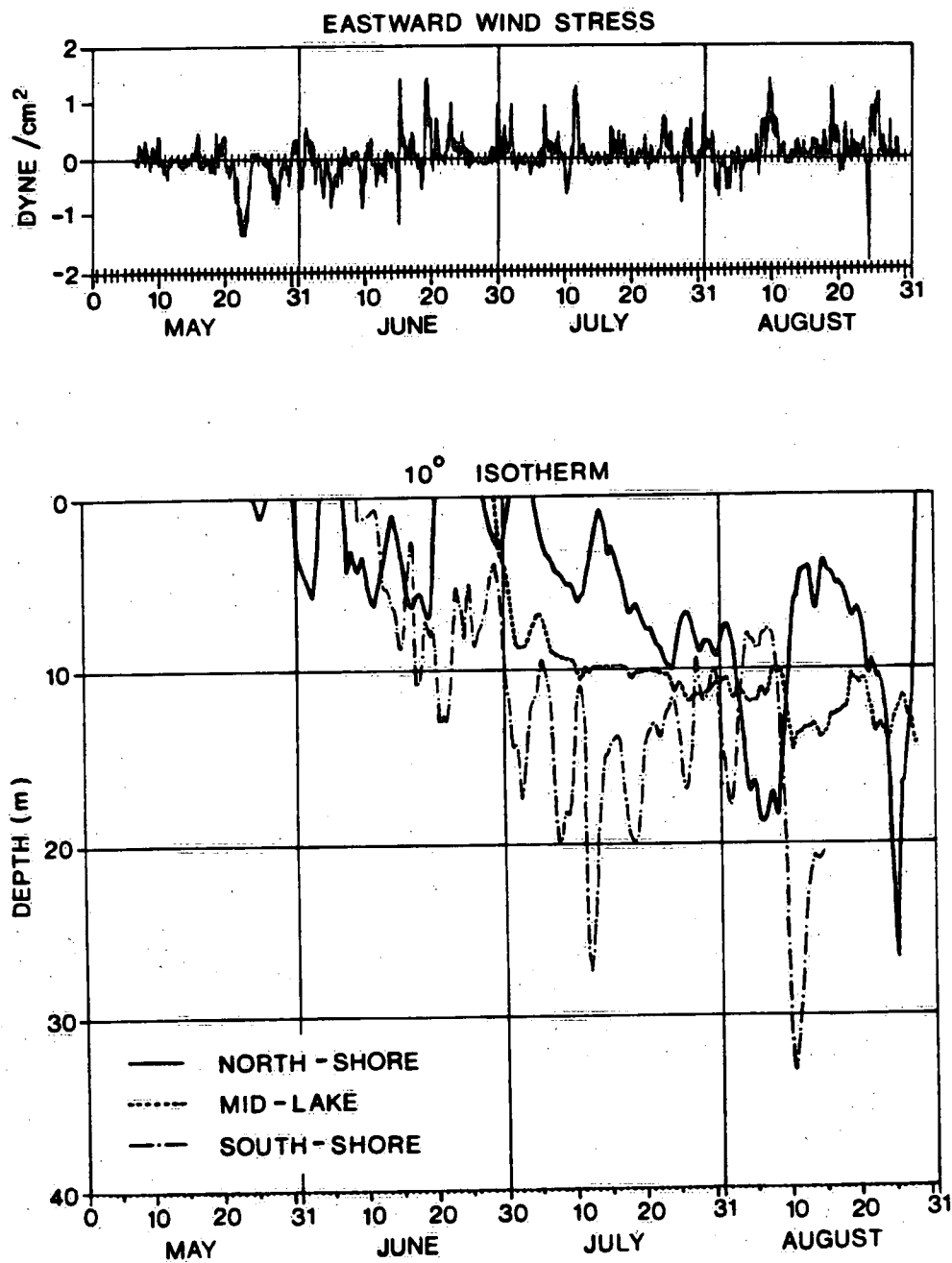


Fig. 2.14 Eastward component of wind stress and depth of 10 degree isotherm in Lake Ontario, 6 May - 30 August 1982.

AH

Nov 4-6 (3-7) San Francisco

20,21 Ithaca

19 Albany

7 a

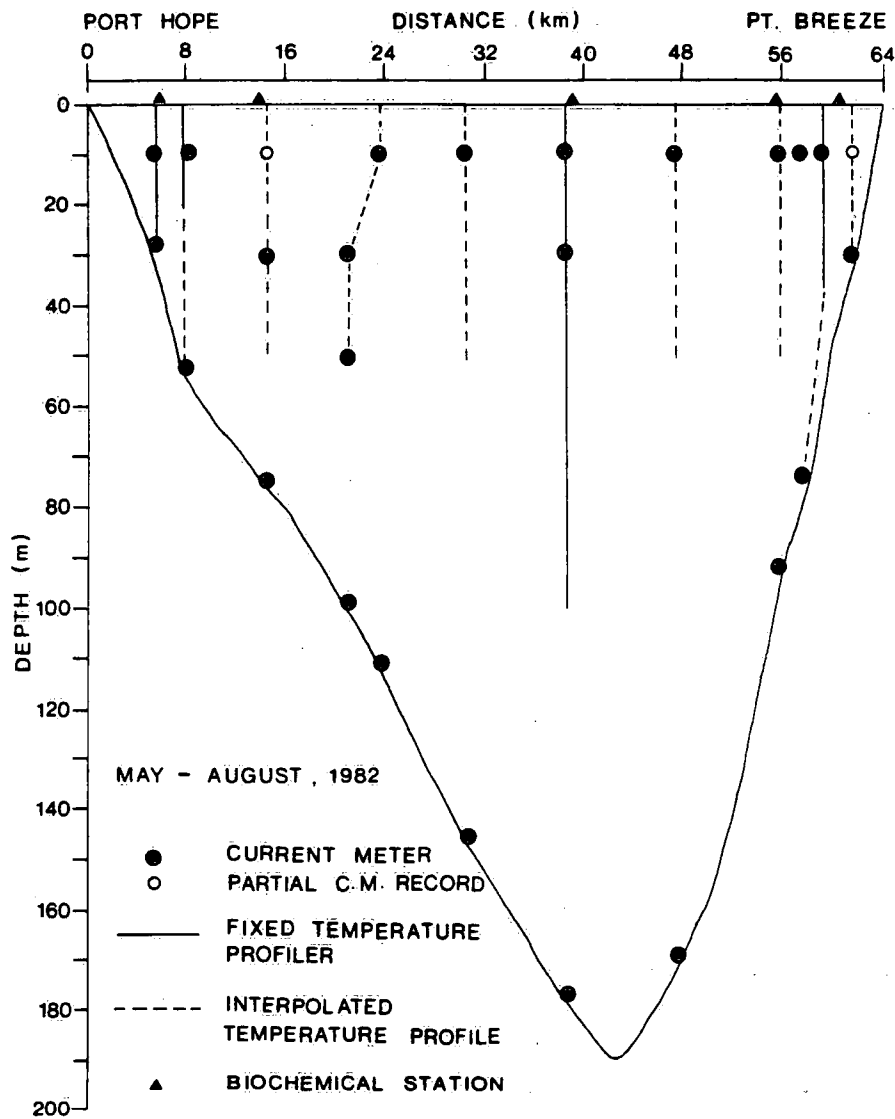


Fig. 2.15 Location of observed and interpolated vertical temperature profiles in cross section of Lake Ontario between Port Hope and Point Breeze.

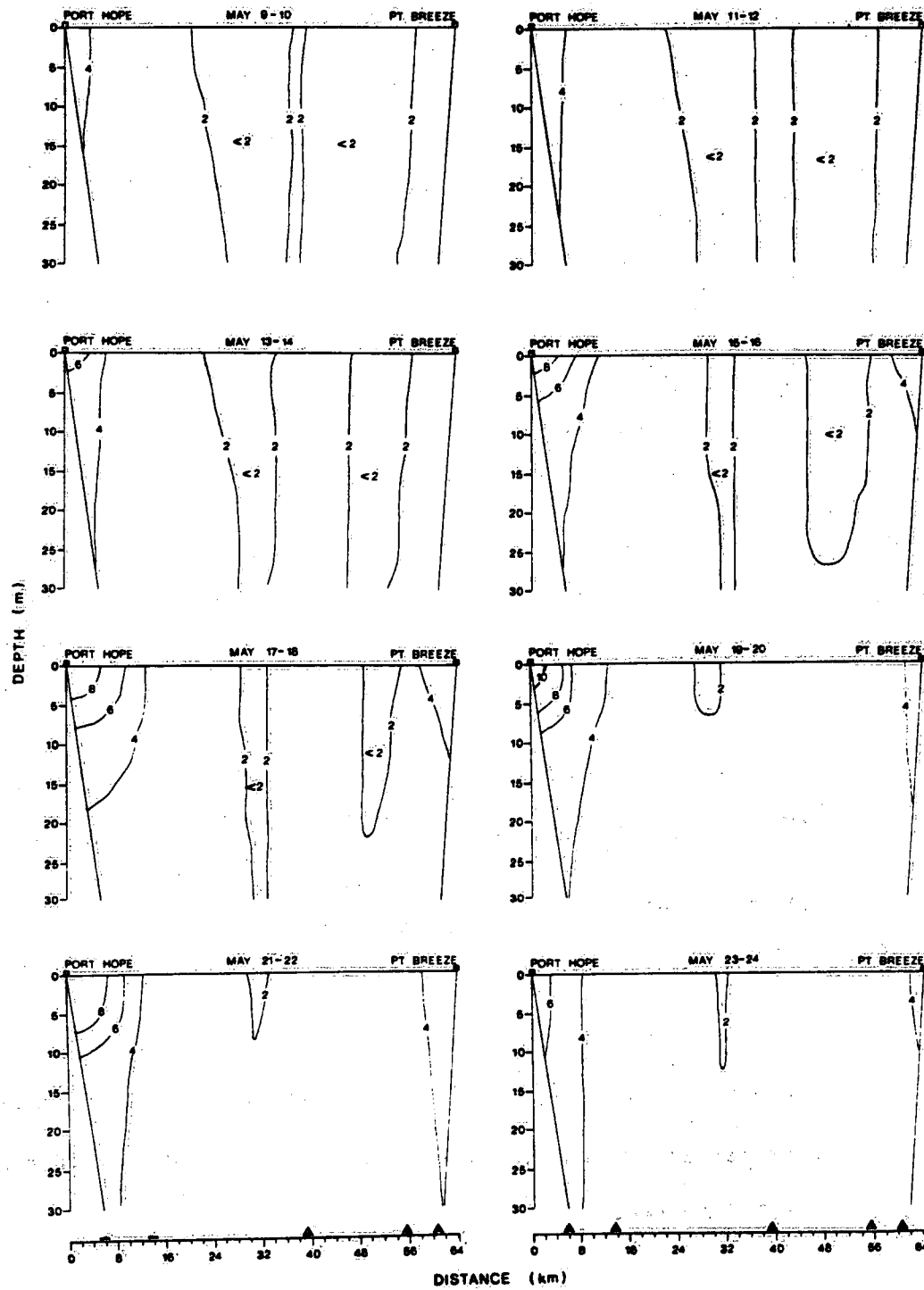


Fig. 2.16 Two-day averages of temperature distributions in cross section of Lake Ontario between Port Hope and Point Breeze.

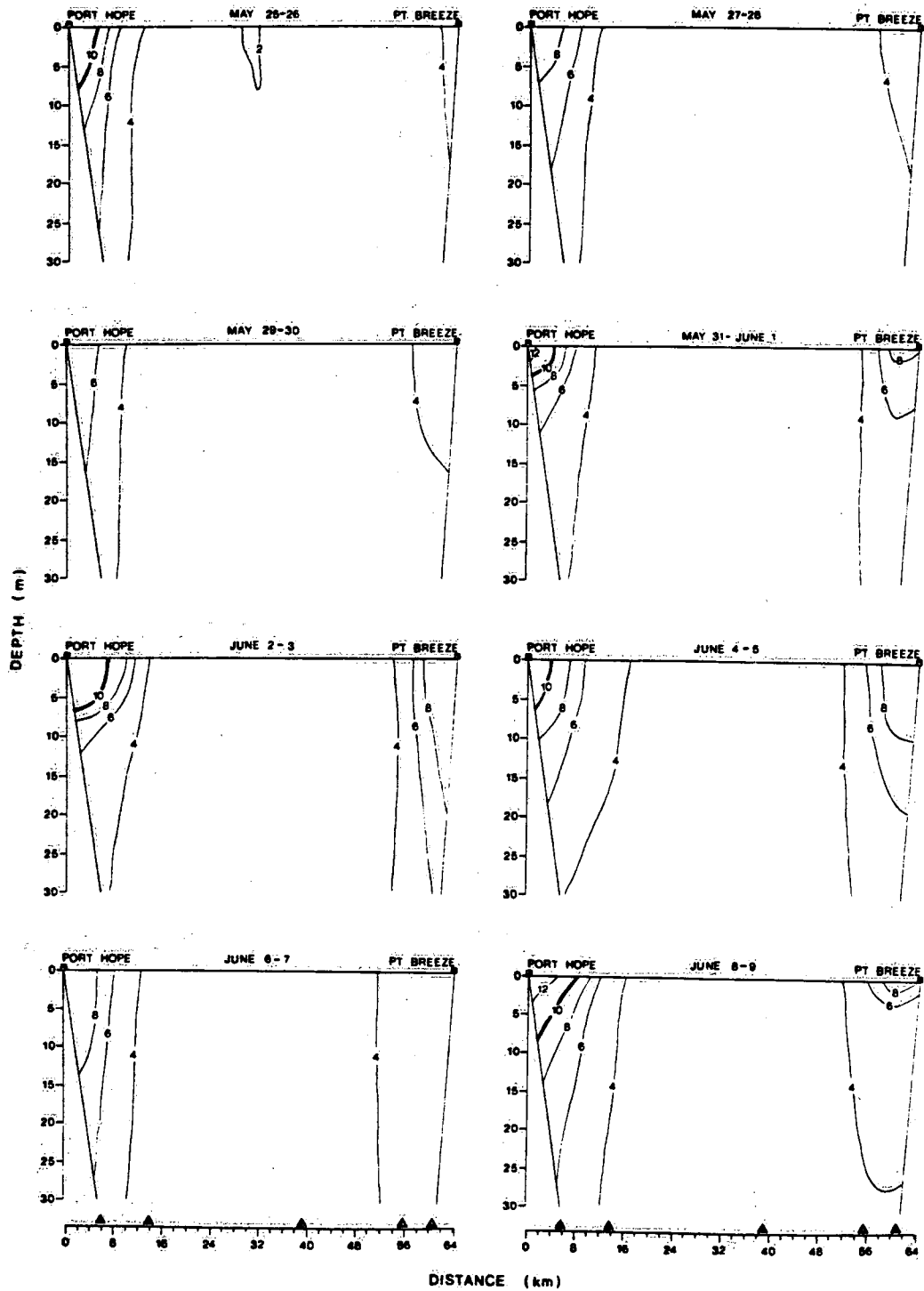


Fig. 2.17 Continuation of Fig. 2.16.



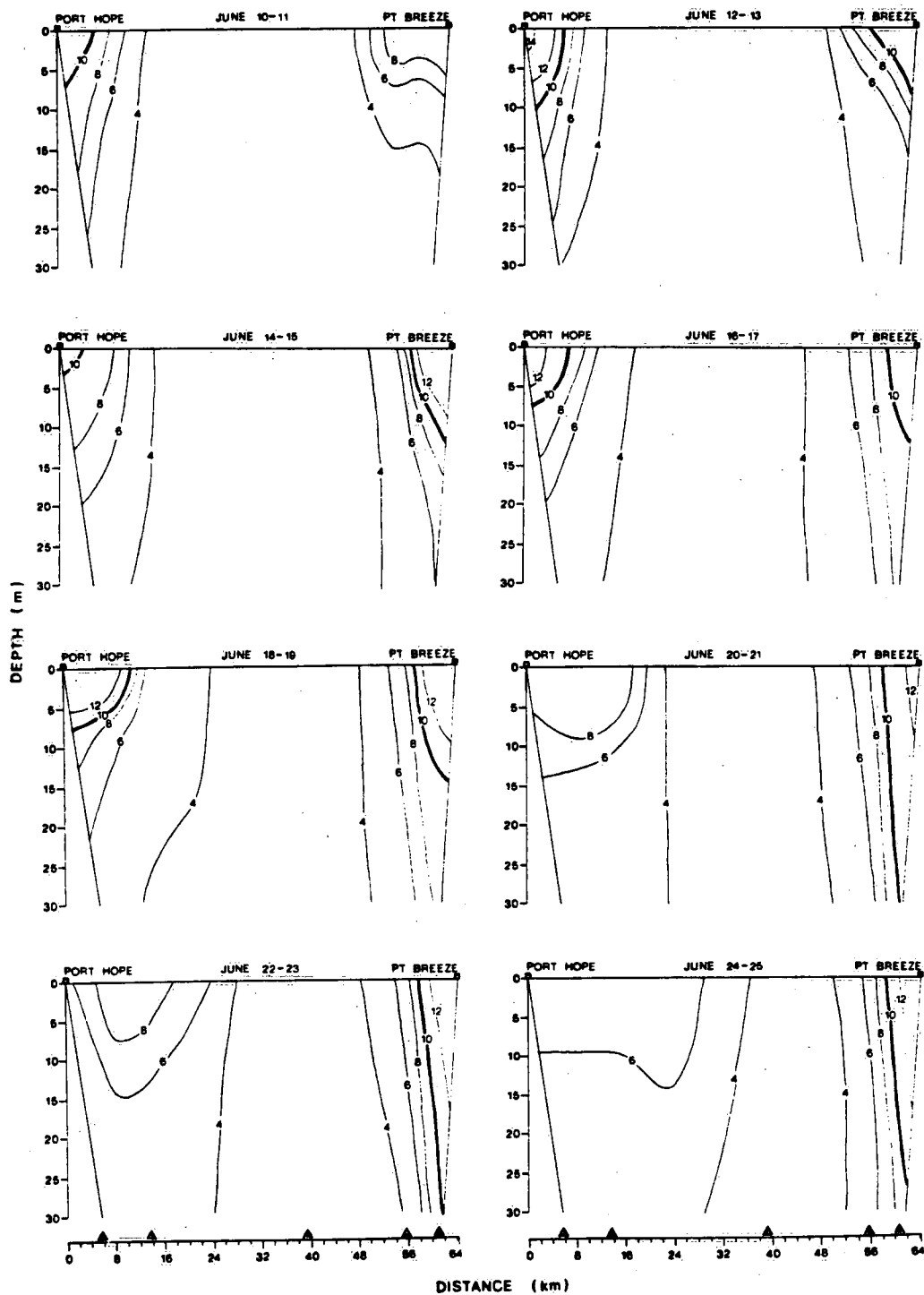


Fig. 2.18 Continuation of Fig. 2.17.

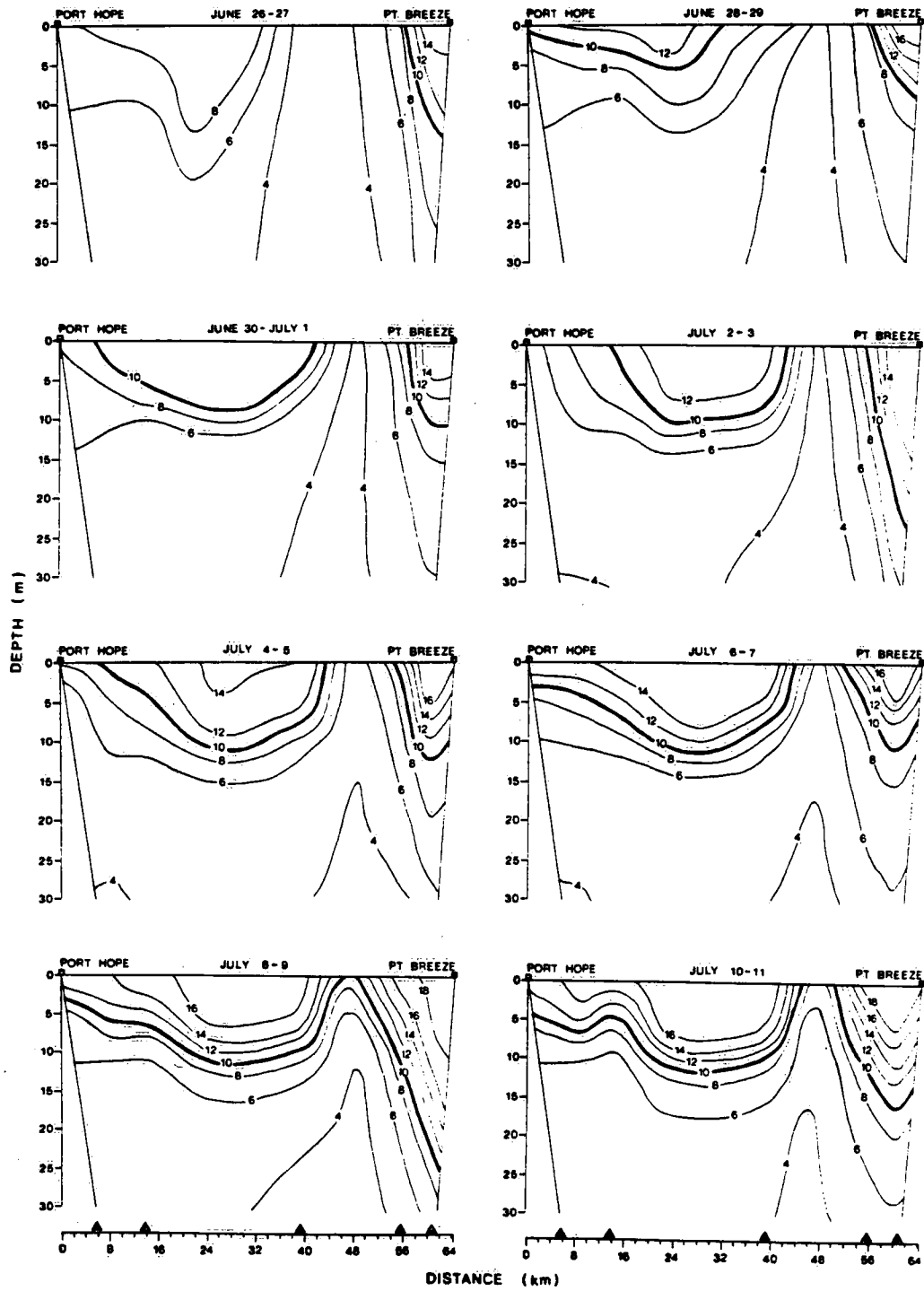


Fig. 2.19 Continuation of Fig. 2.18.

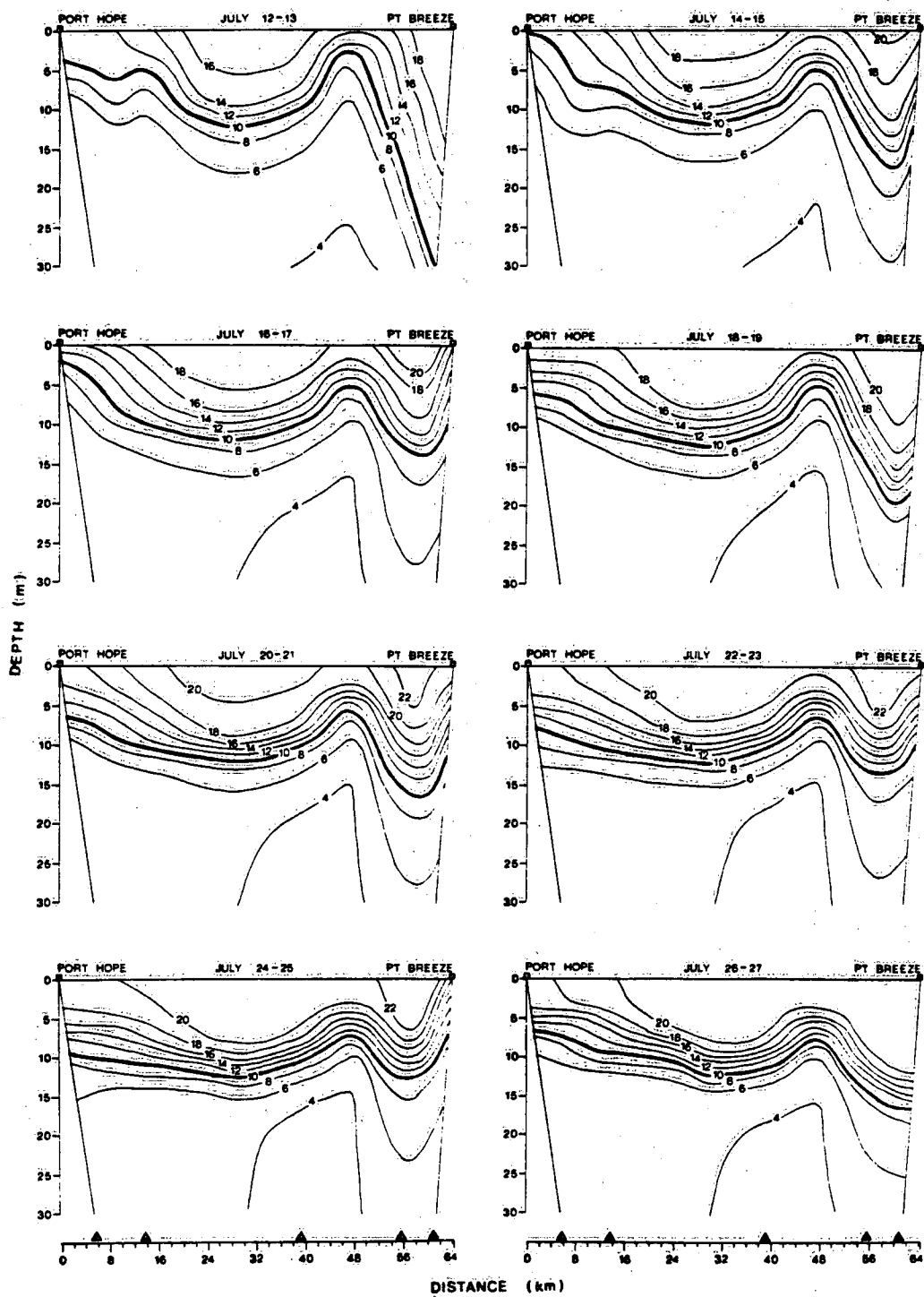


Fig. 2.20 Continuation of Fig. 2.19.

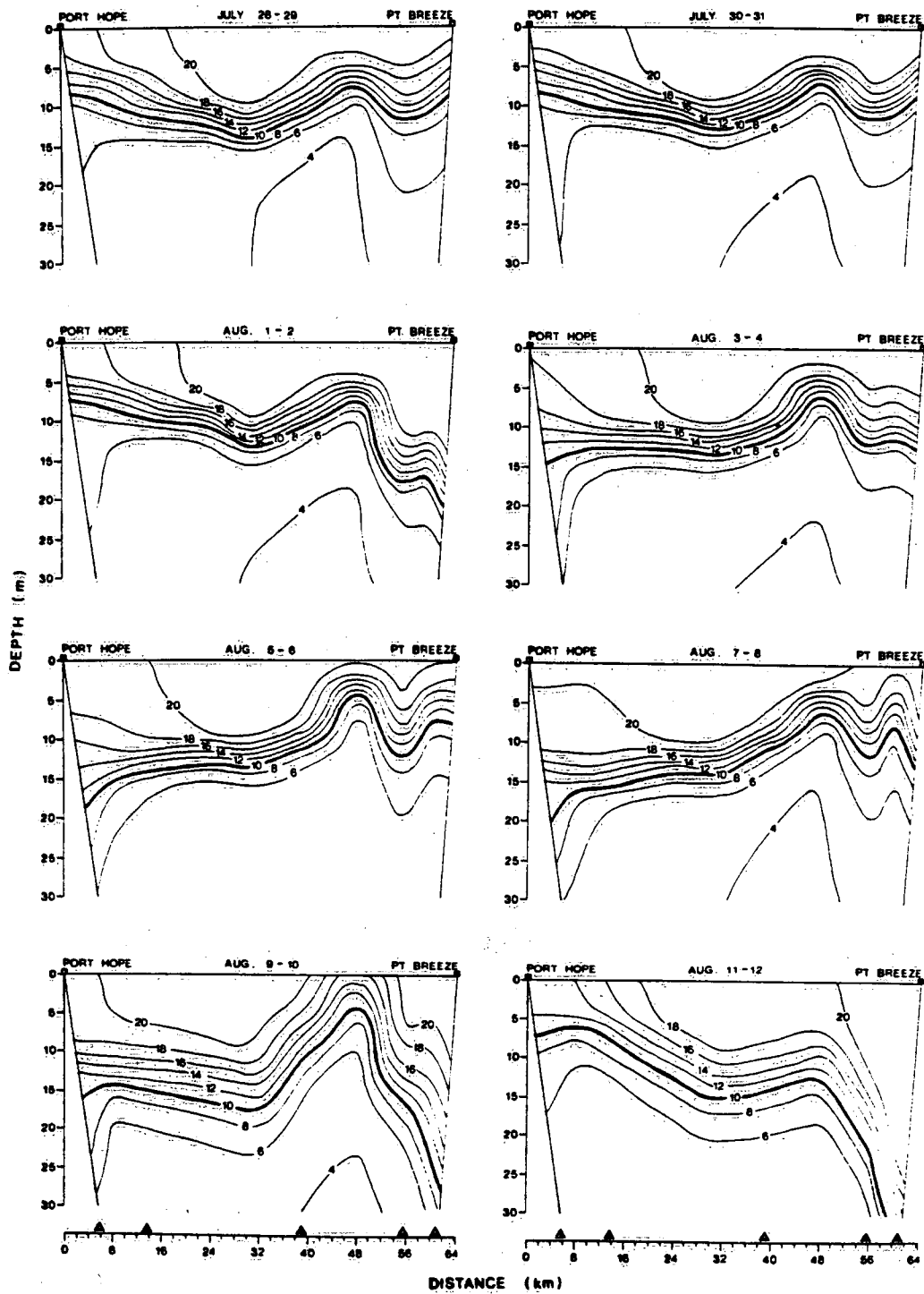


Fig. 2.21 Continuation of Fig. 2.20.

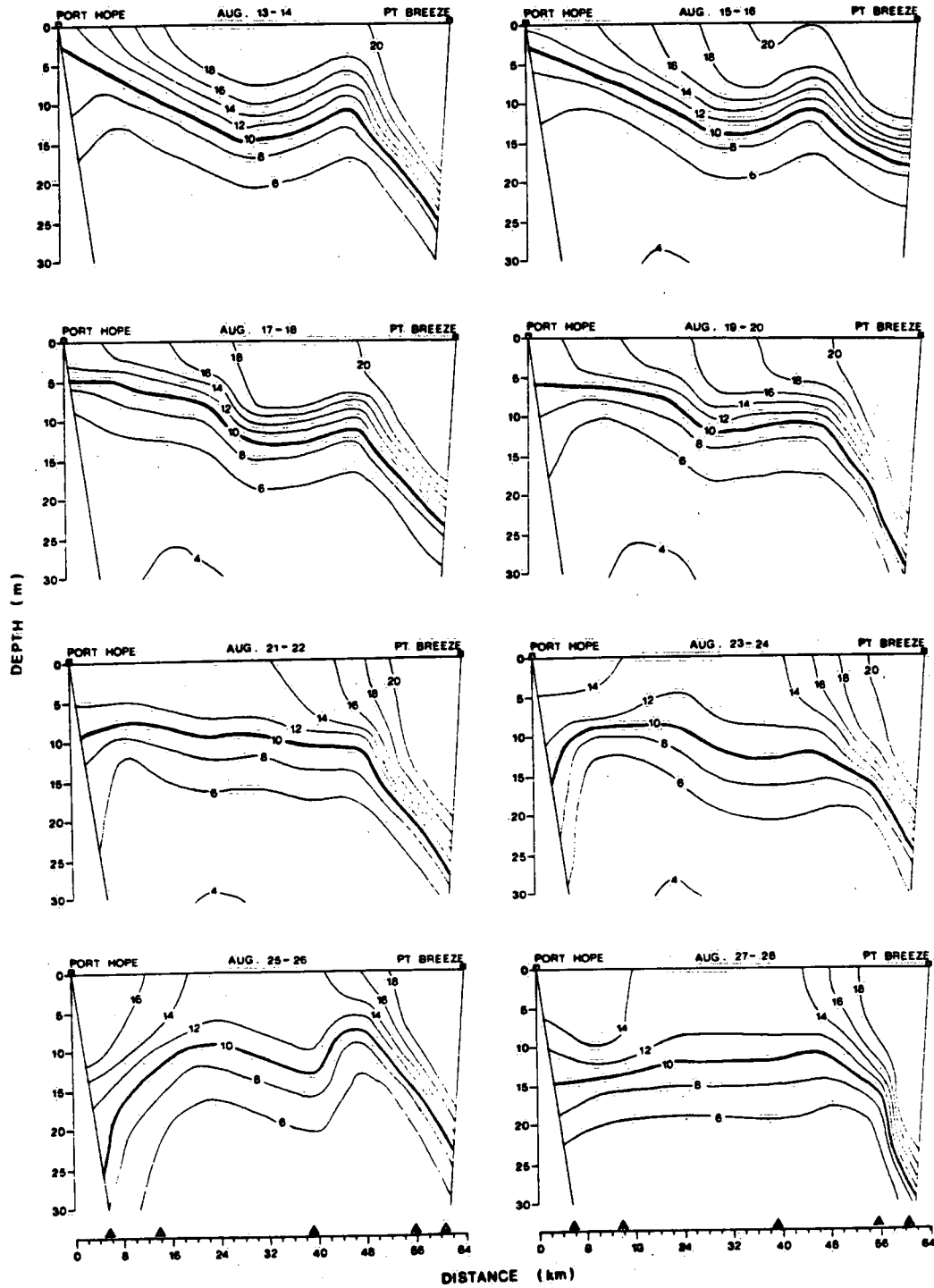


Fig. 2.22 Continuation of Fig. 2.21.

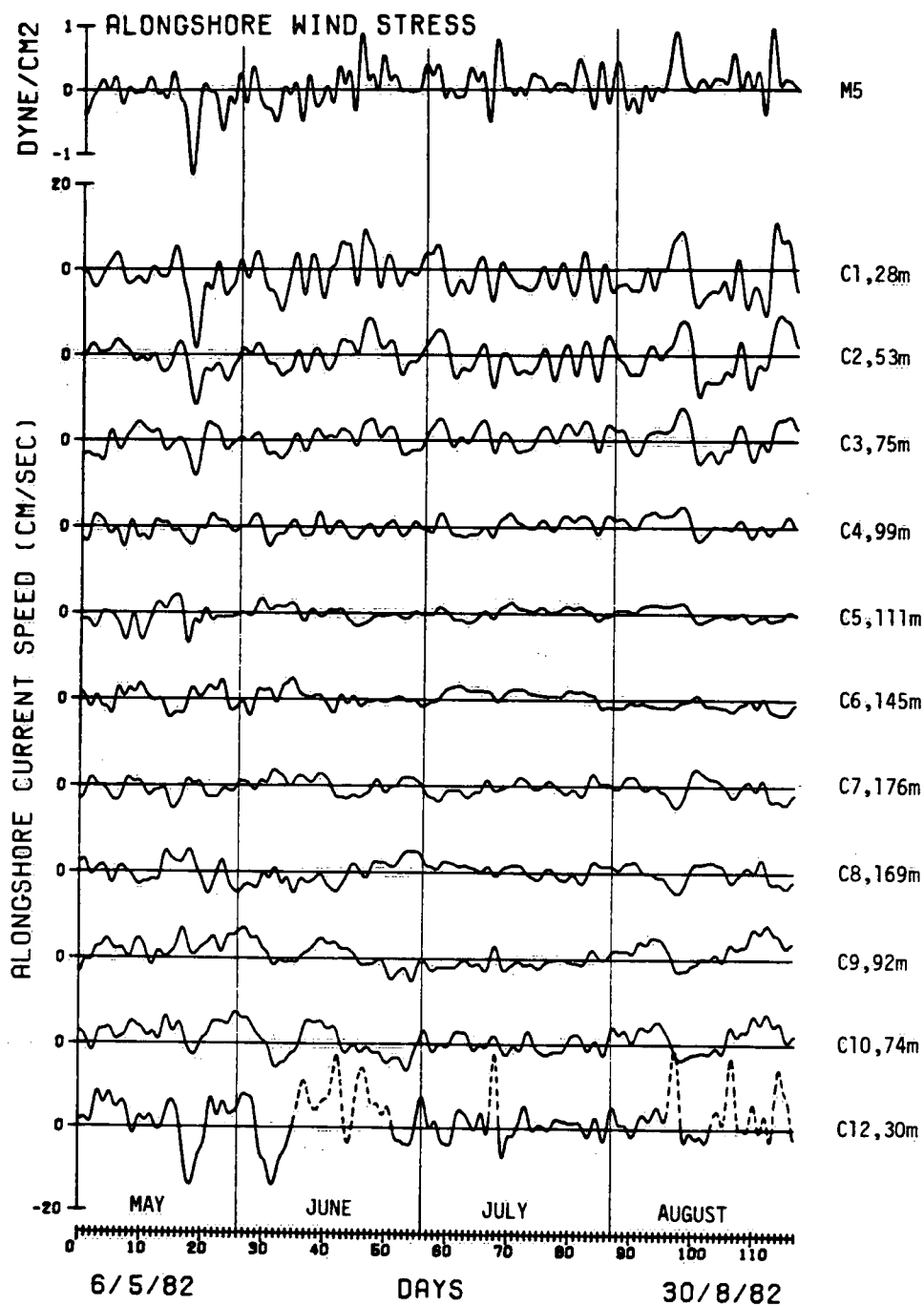


Fig. 2.23 Alongshore components of bottom currents in cross section of Lake Ontario between Port Hope and Point Breeze.

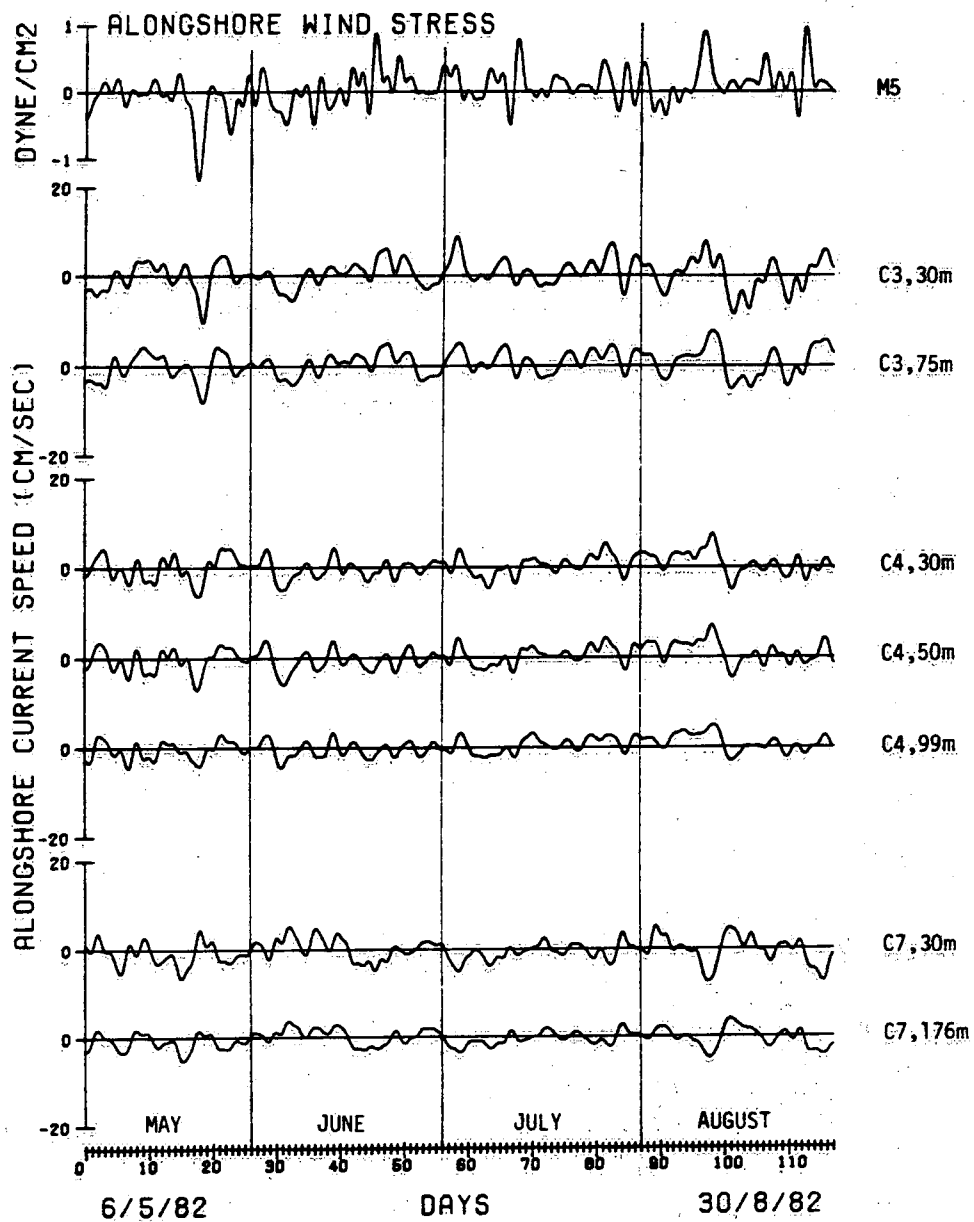


Fig. 2.24 Vertical structure of alongshore currents in hypolimnion.

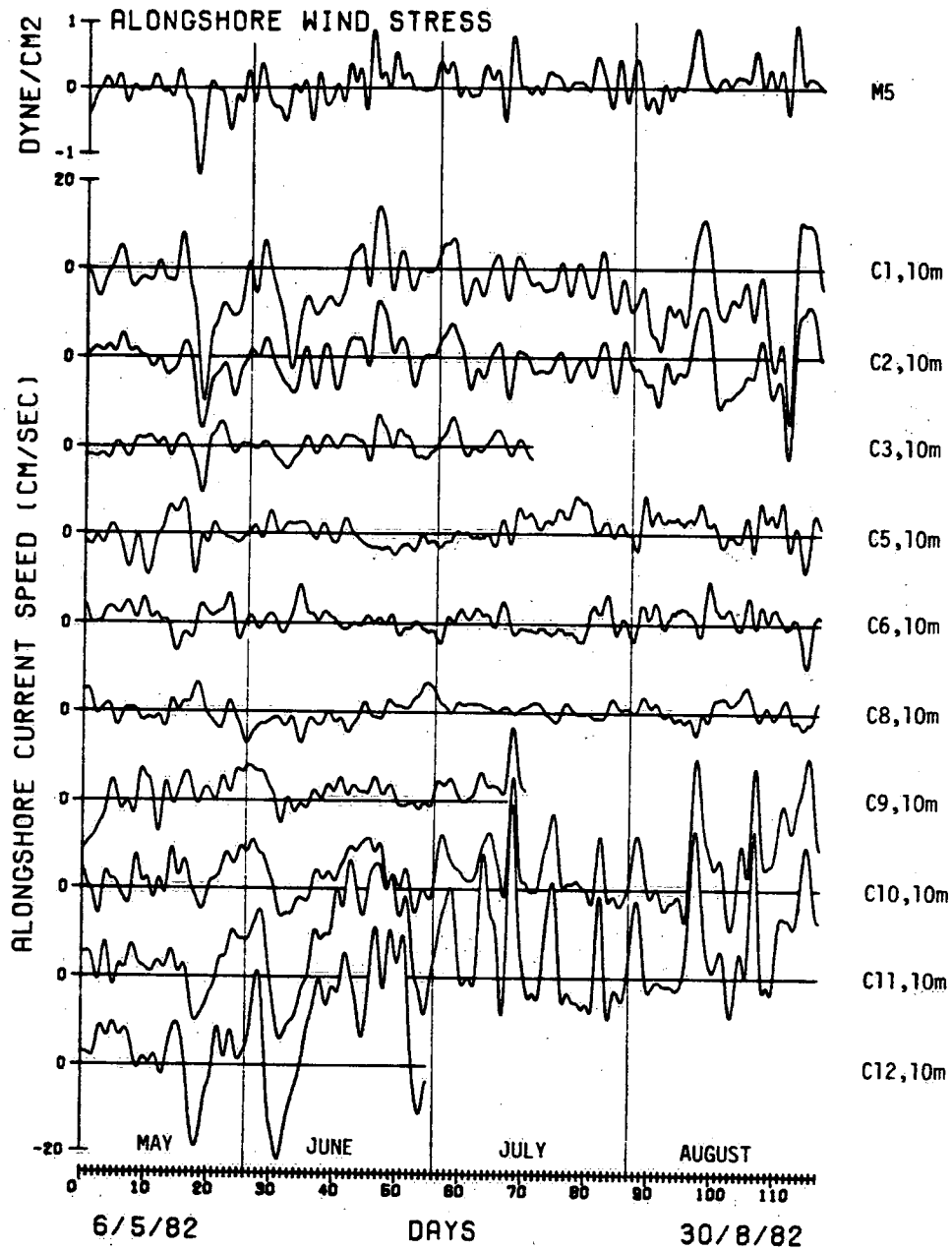


Fig. 2.25 Alongshore current components at 10 m depth in cross section of Lake Ontario between Port Hope and Point Breeze.



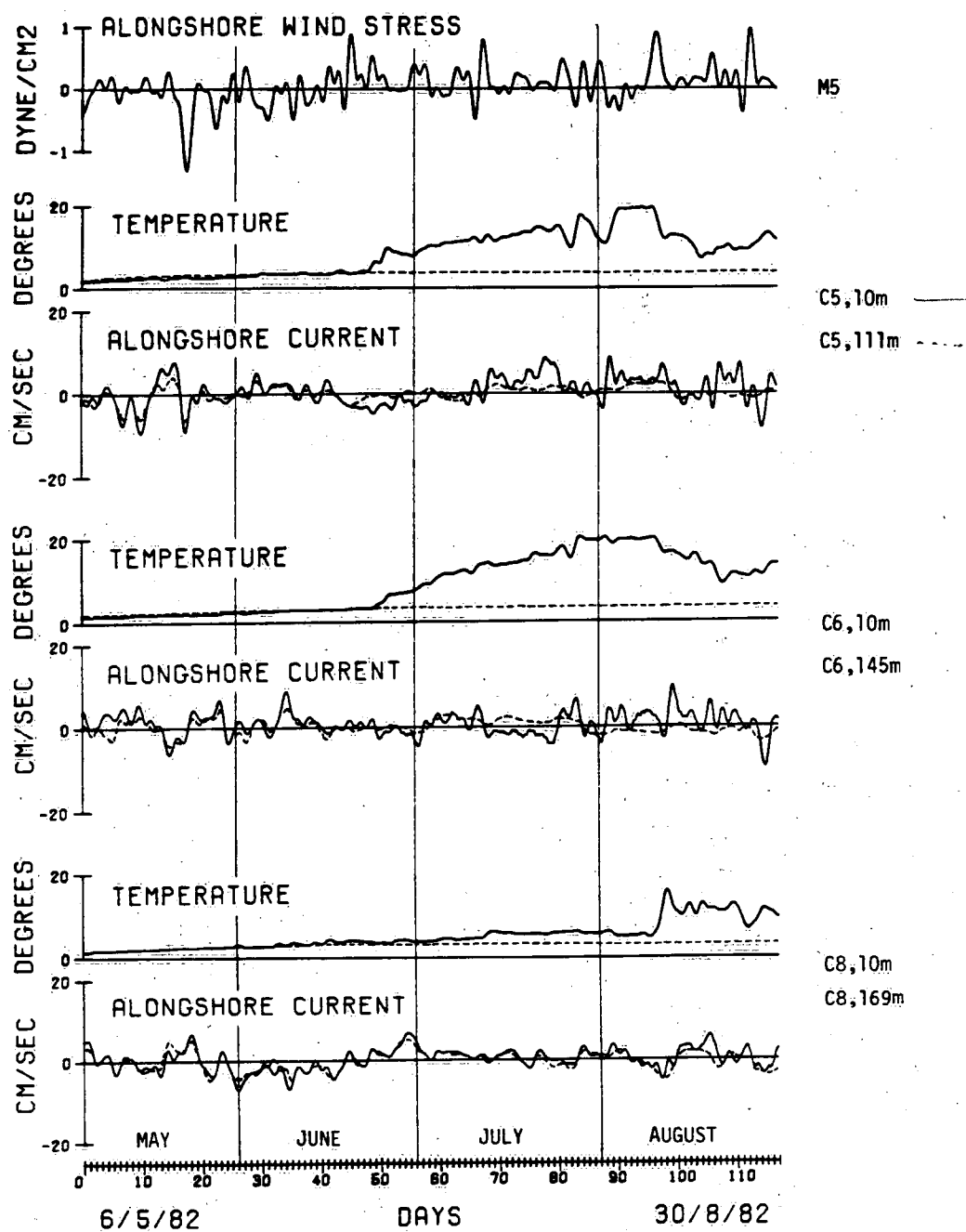


Fig. 2.26 Vertical structure of temperature and alongshore current in selected deep-water moorings.

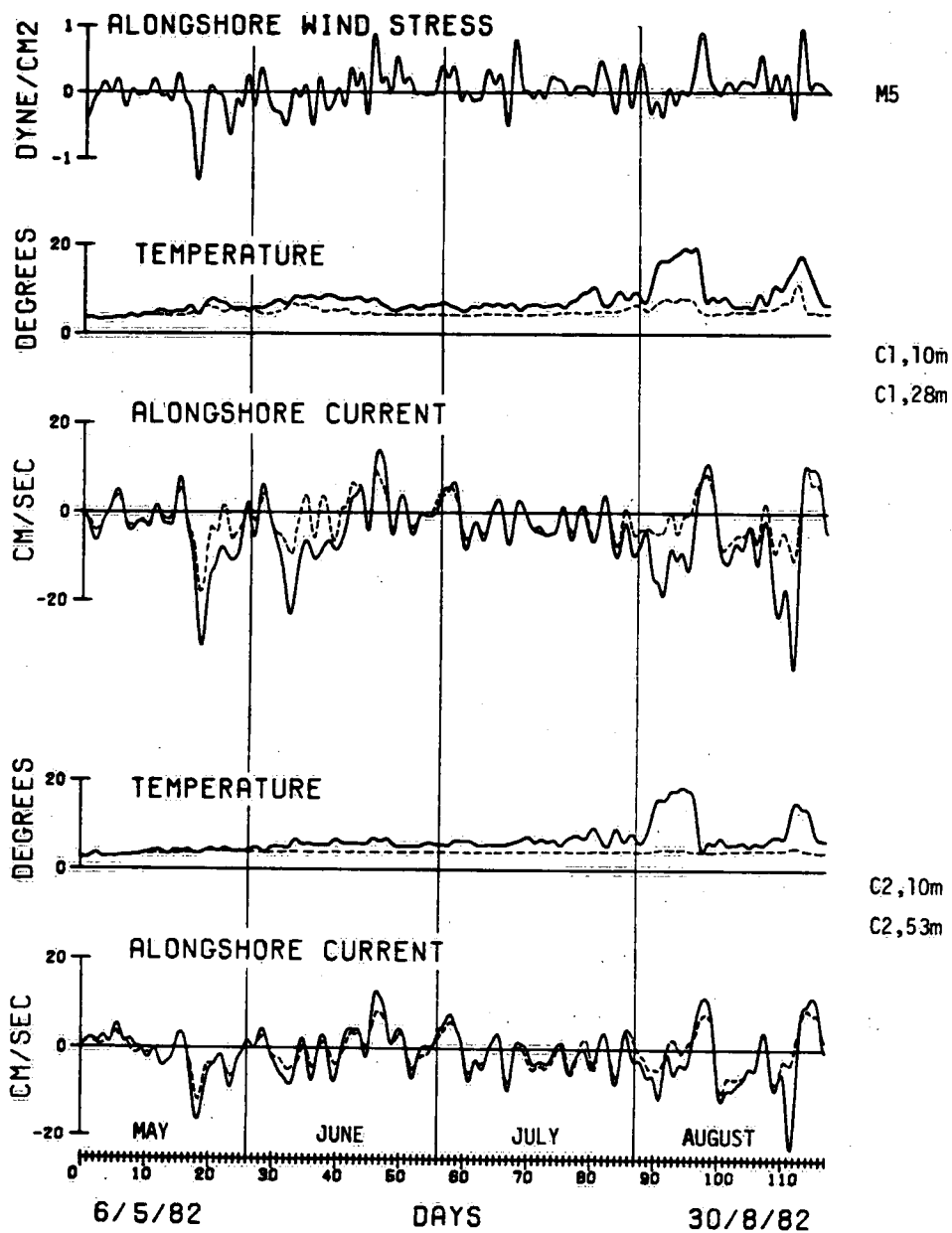


Fig. 2.27 Vertical structure of temperature and alongshore current for north-shore stations.

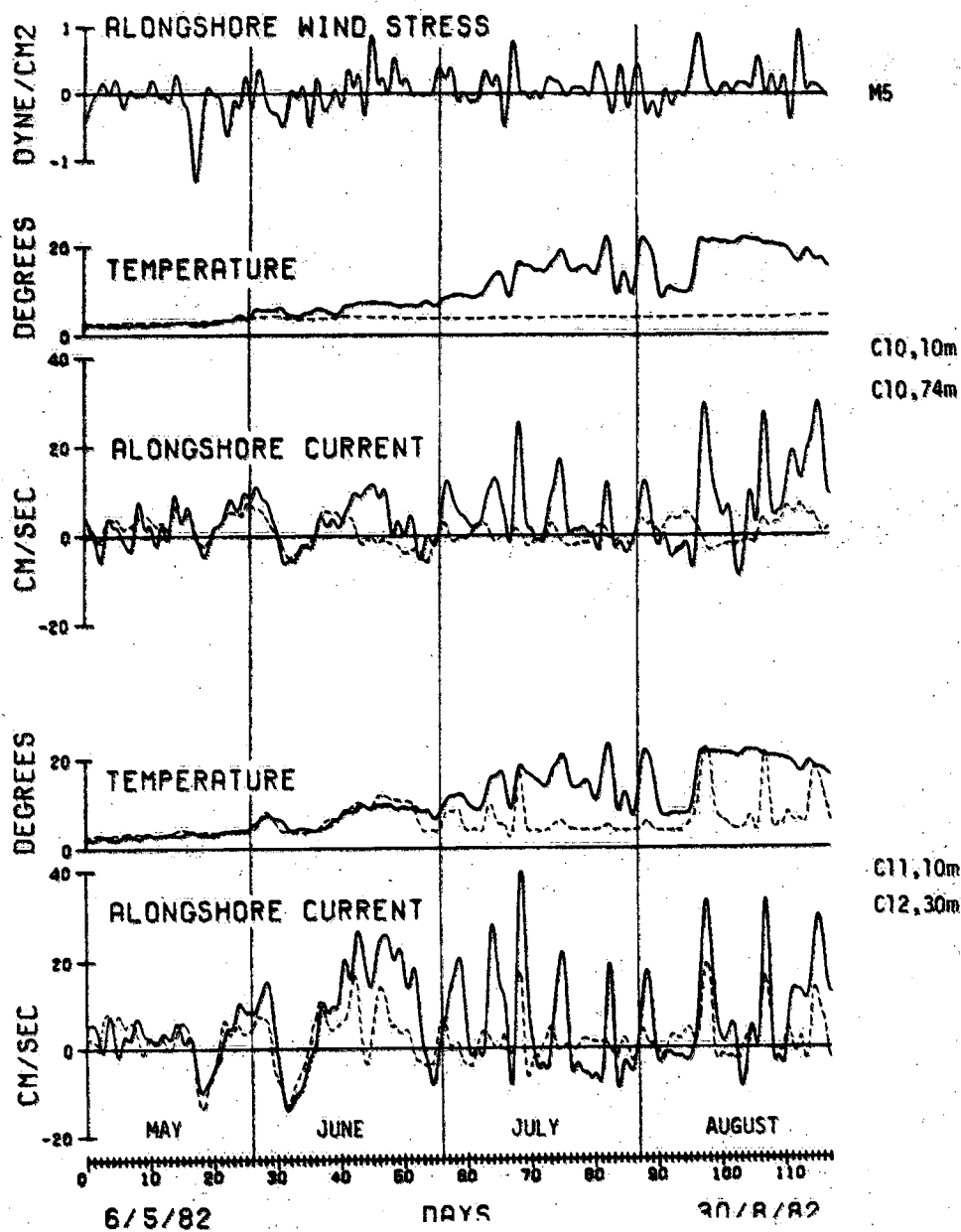


Fig. 2.28 Vertical structure of temperature and alongshore current for south-shore stations.

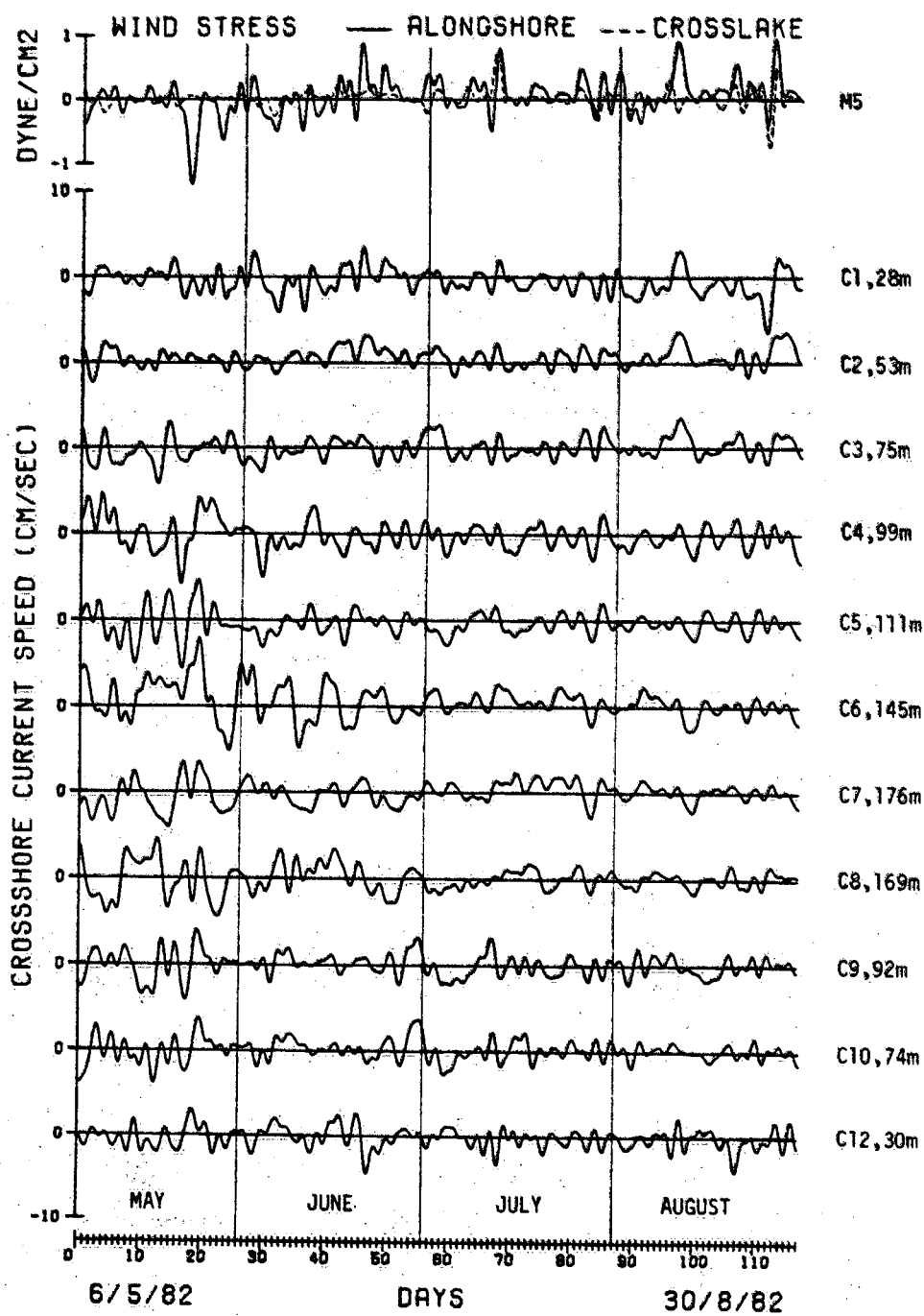


Fig. 2.29 Cross-shore current components at bottom of cross section of Lake Ontario between Port Hope and Point Breeze.

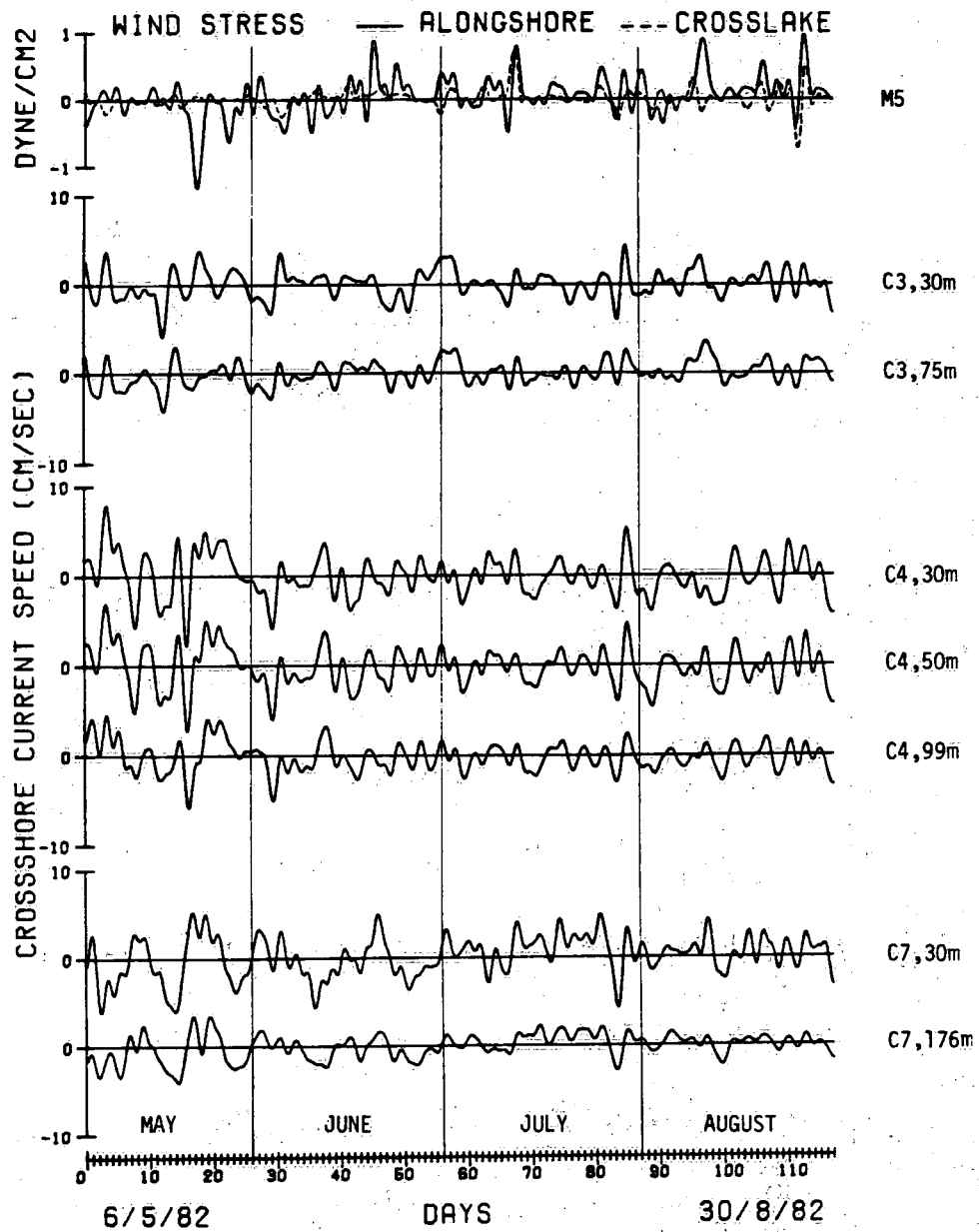


Fig. 2.30 Vertical structure of cross-shore currents in hypolimnion.

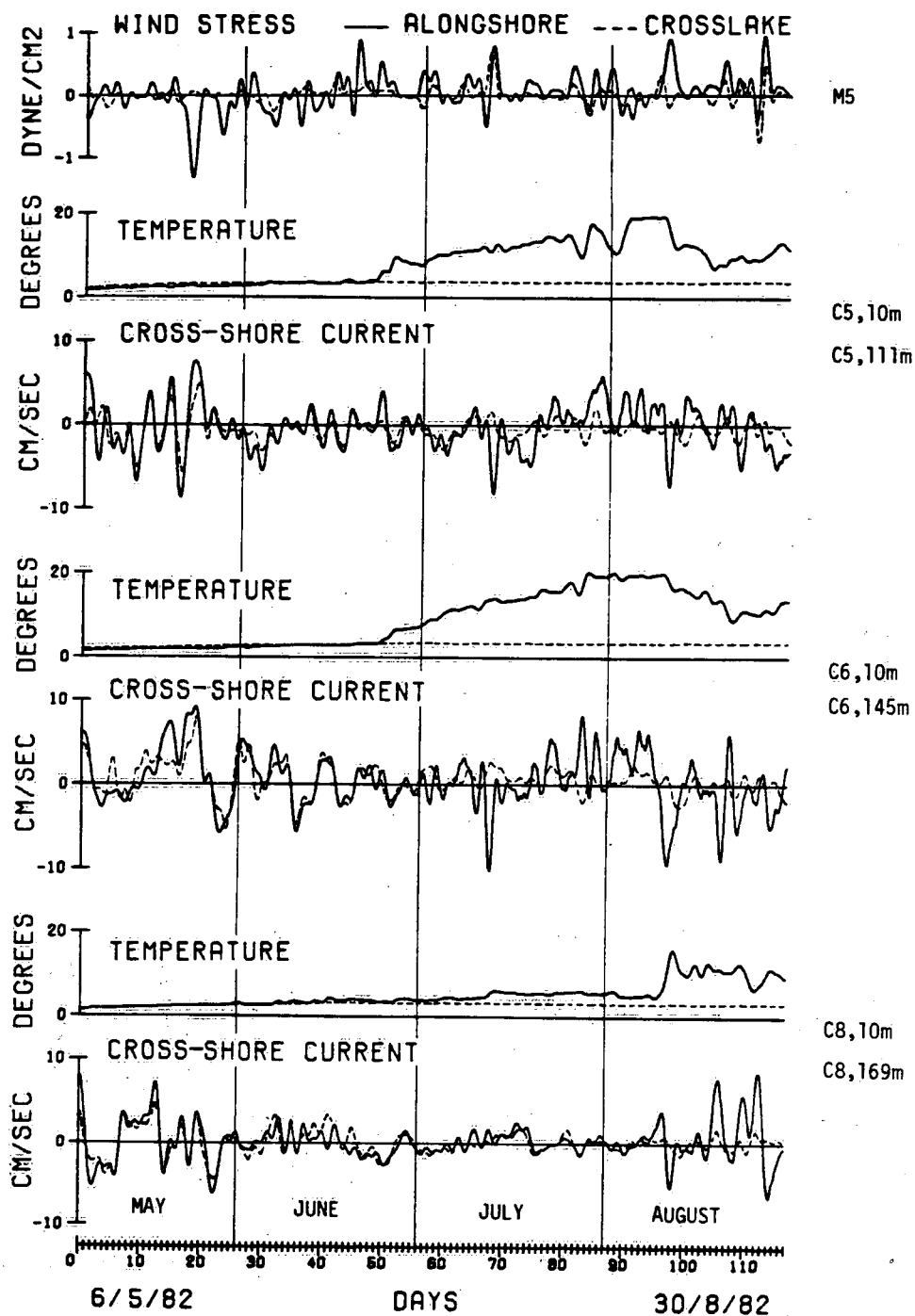


Fig. 2.31 Vertical structure of temperature and cross-shore current in selected deep-water moorings.

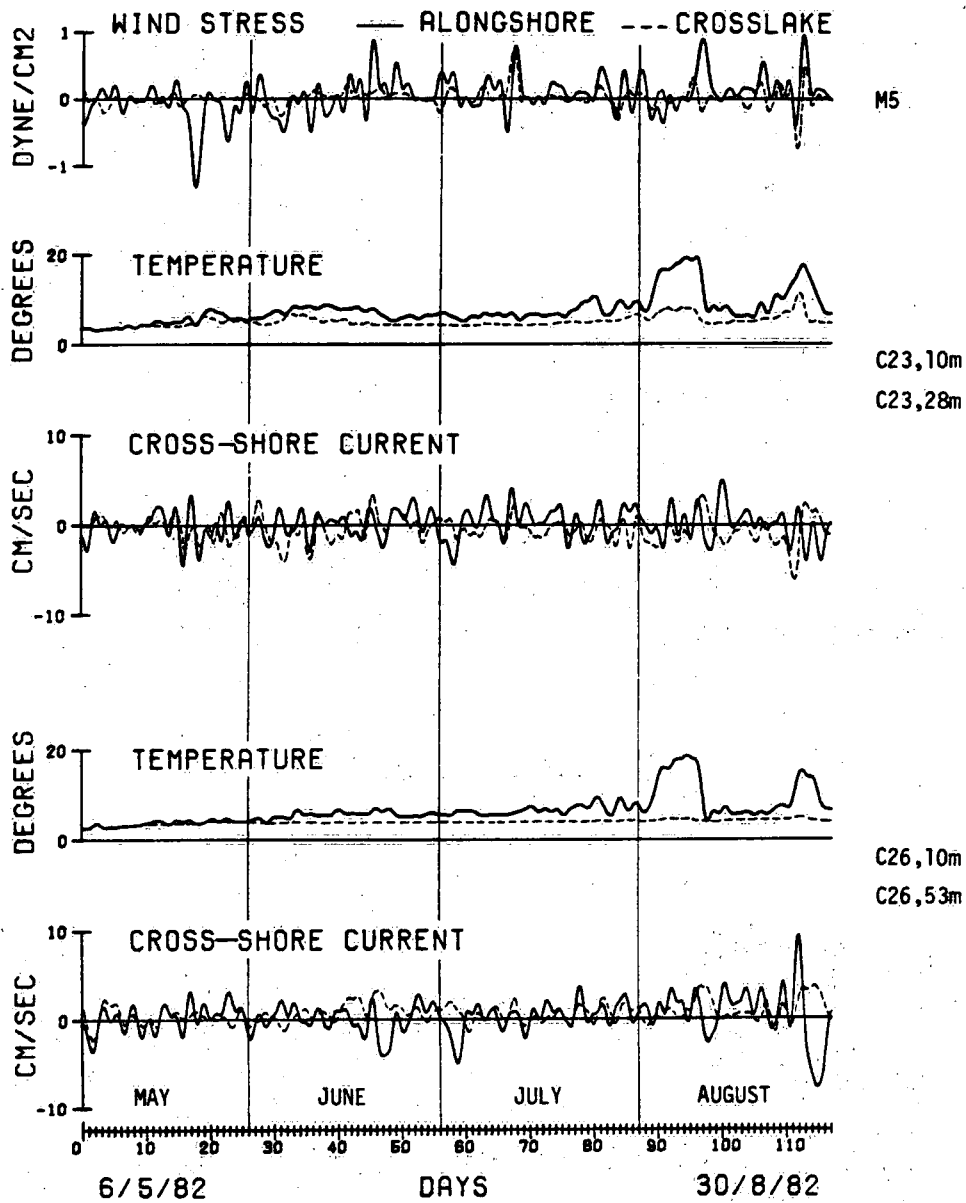


Fig. 2:32 Vertical structure of temperature and cross-shore current for the north shore.

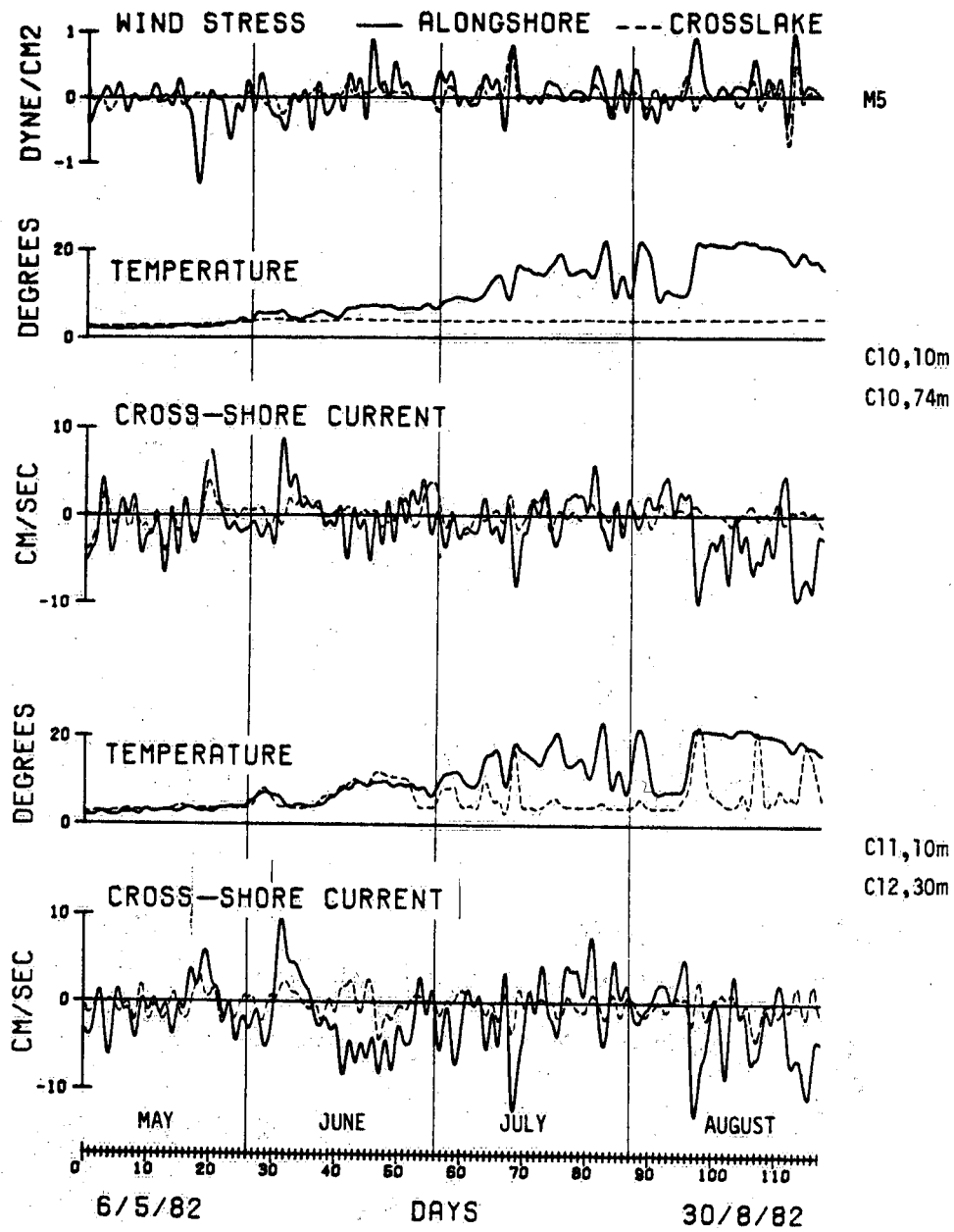


Fig. 2.33 Vertical structure of temperature and cross-shore current for the south shore.



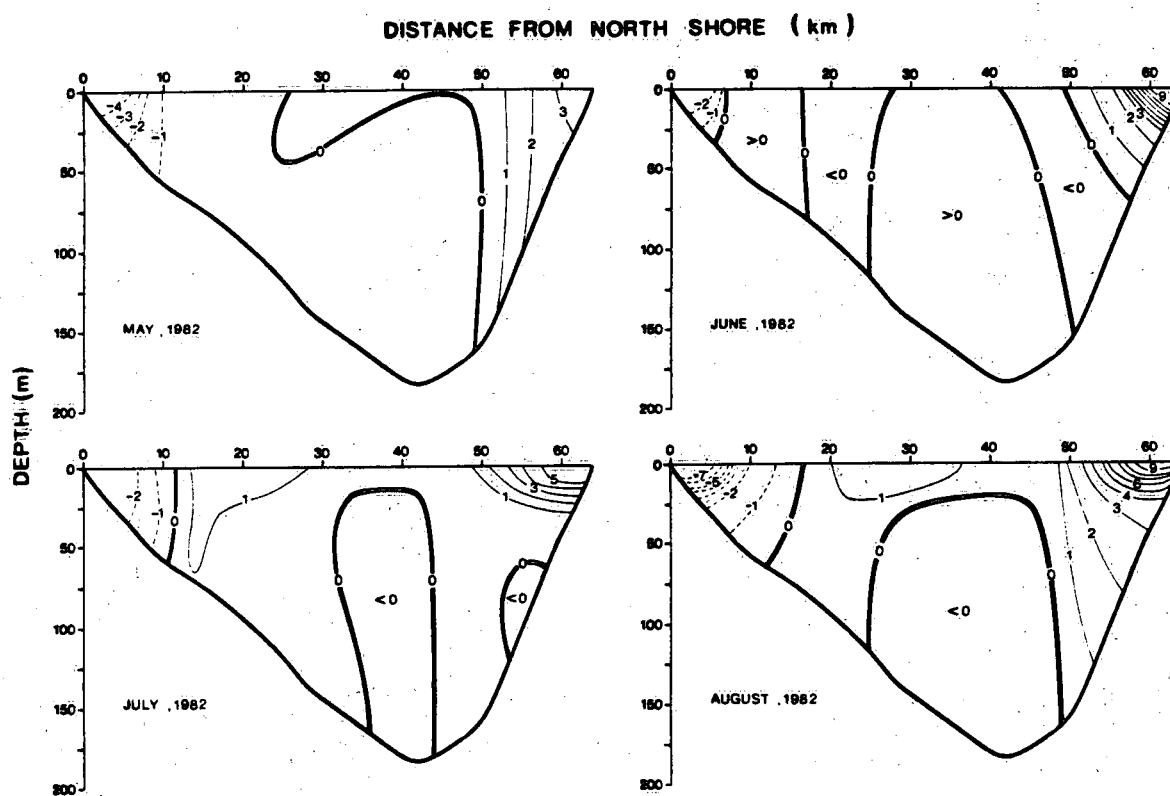


Fig. 2.34 Monthly averages of current distributions in cross section of Lake Ontario between Port Hope and Point Breeze. Positive values represent eastward current.

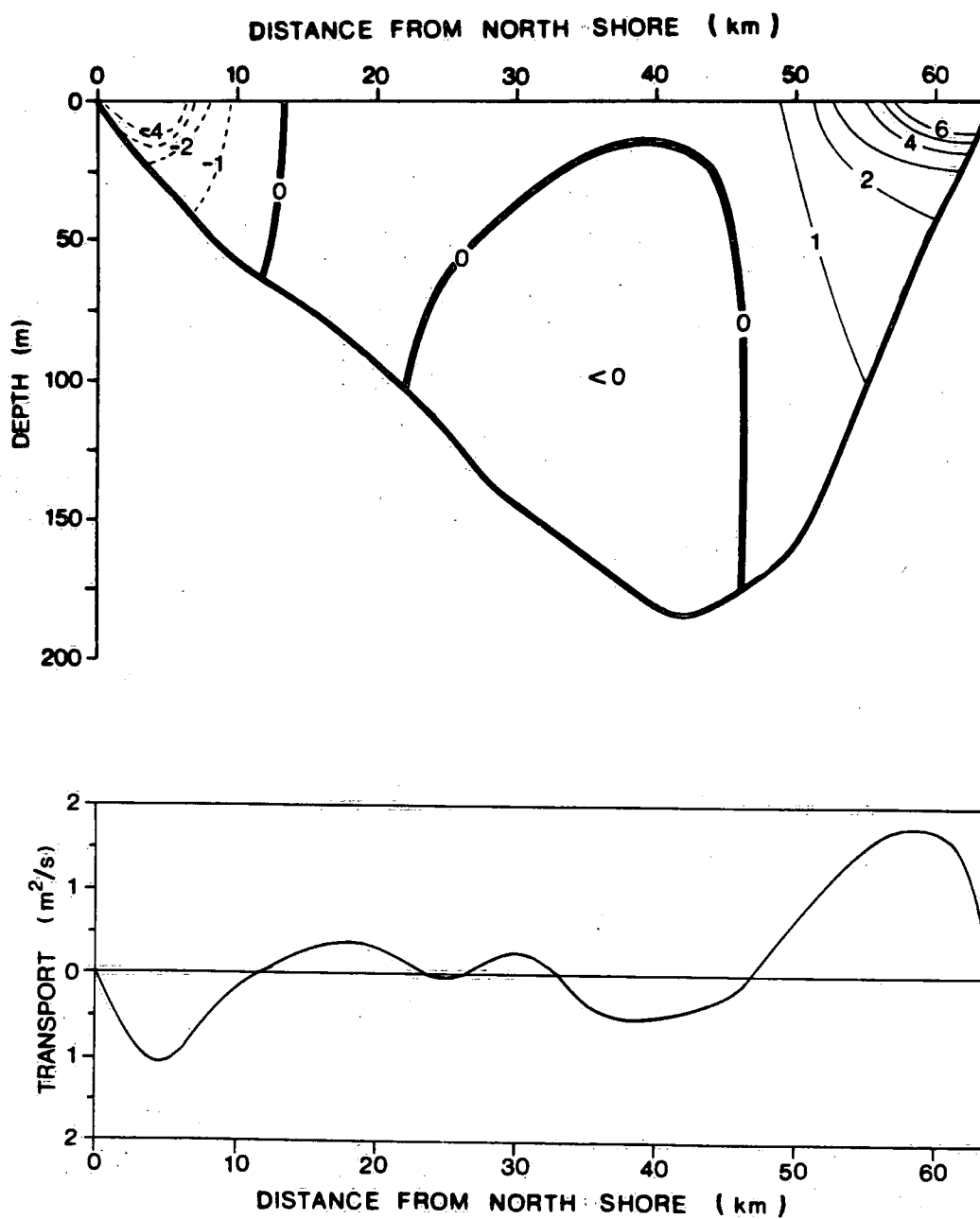


Fig. 2.35 Average current distribution in cross section of Lake Ontario, May - August 1982 (above) and average transport through cross section (below). Positive values represent eastward flow.

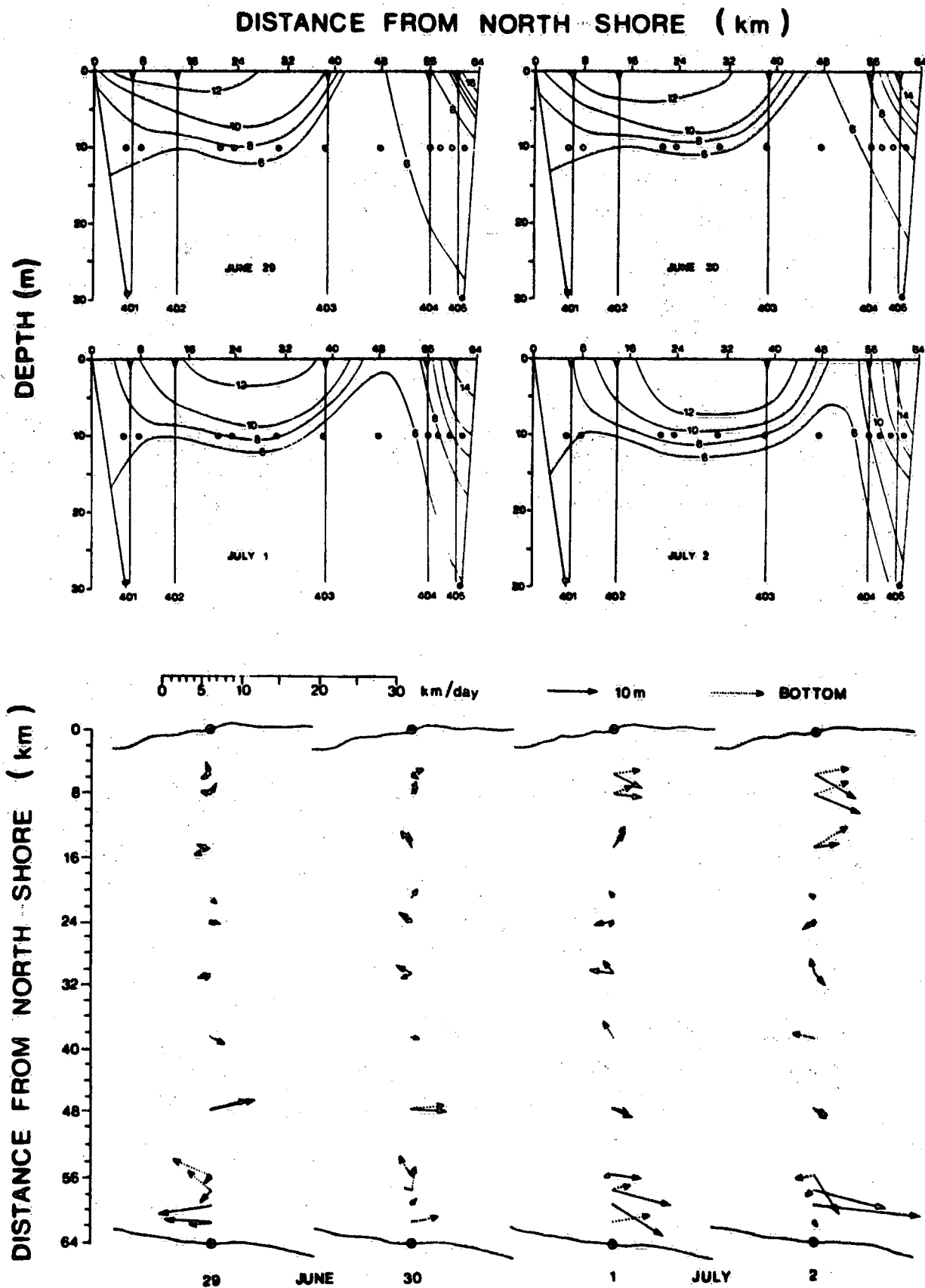


Fig. 2.36 Daily temperatures (above) and currents (below) in Lake Ontario cross section between Port Hope and Point Breeze, June 29 - July 2, 1982.

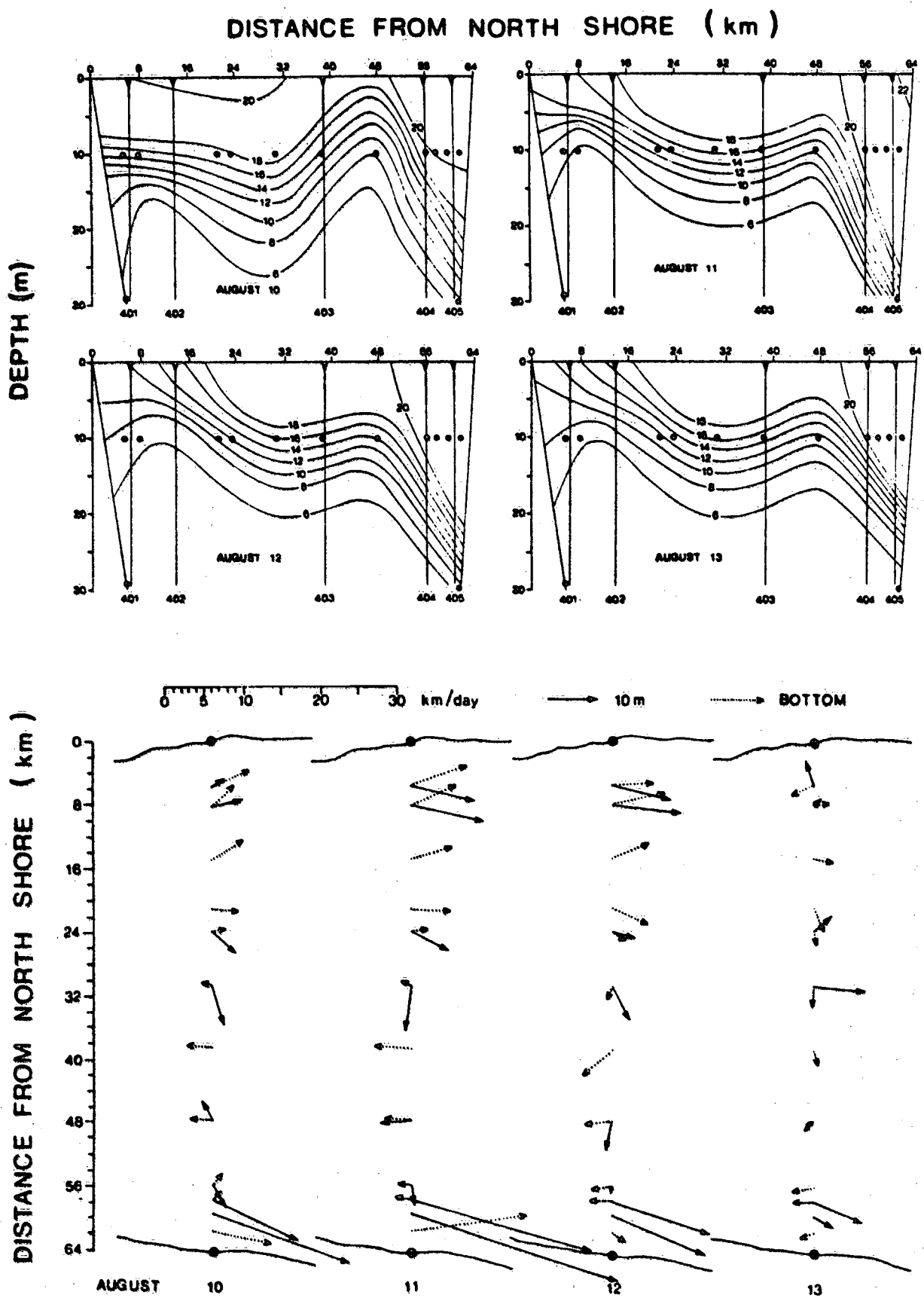


Fig. 2.37 Daily temperatures (above) and currents (below) in Lake Ontario cross section between Port Hope and Point Breeze, August 10 to 13, 1982.

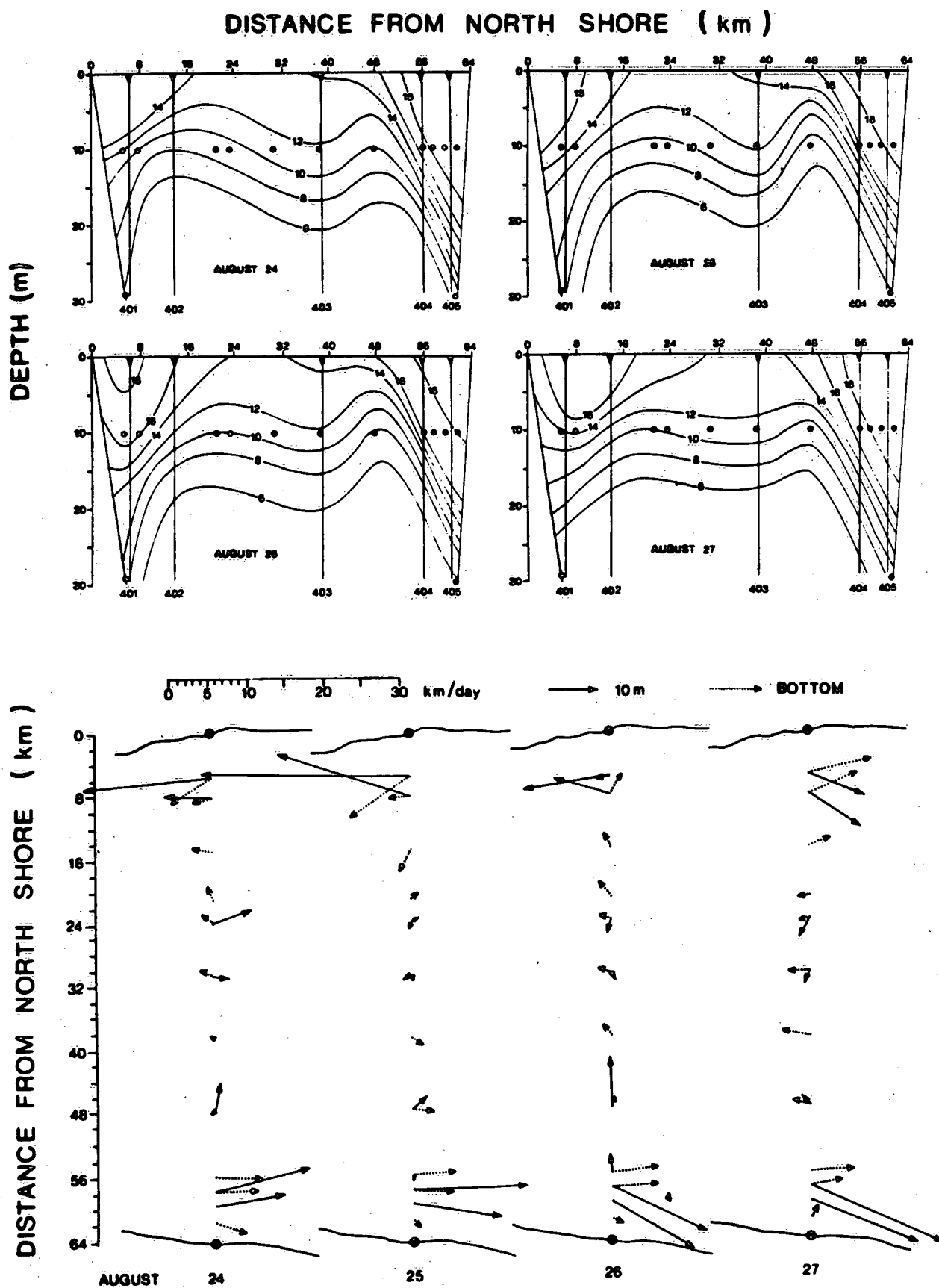


Fig. 2.38 Daily temperatures (above) and currents (below) in Lake Ontario cross section between Port Hope and Point Breeze, August 24 to 27, 1982.

## Summer Study: North Shore

### 3.1 Alongshore Variation of Temperatures and Currents

The following discussion is concerned with observation of temperatures and currents in the northern part of the central transect of Lake Ontario and the coastal transects to the east and west (Figure 1.1, Table 1.1). Figure 3.1 presents the east-to-west variation of alongshore currents at depths of 30 m (top of figure), 50 m (middle) and 75 m (bottom). All data have been smoothed to eliminate fluctuations with periods shorter than two days. The currents are seen to be quite uniform alongshore and highly correlated with the alongshore wind shown at the top of the figure.

Figure 3.2 illustrates the vertical structure of temperature and currents in the coastal zone. Surface observations are denoted by solid lines, bottom observations by dashed lines. Only during periods of strong downwelling in August, the thermocline dips below the 10-m level and a vertical shear appears in the current meter records. These downwelling events appear to be associated with wind impulses from easterly directions but, as will be seen in the following, the dynamics of the second event are quite different from the first.

Figure 3.3 presents temperature variations obtained from the fixed temperature profilers. The onset of wind-induced upwelling

and downwelling occurs essentially simultaneously along the whole north shore as seen, for instance, during the first ten days of August. This is to be expected, since the scale of meteorological systems is so large that the wind is quite uniform over the whole lake (see section 2.1). However, the relaxation of the thermocline after an upwelling event in large lakes often takes place in the form of an internal Kelvin wave propagating around the basin in counterclockwise direction. For Lake Ontario, a number of such events were documented during the 1972 International Field Year. A striking example is found in the present records after the upwelling event of August 9-11. The subsequent deepening of the thermocline is seen to propagate from east to west along the north shore until another upwelling event occurs in late August.

In order to investigate the alongshore structure of the temperature response to wind, use was made of observations in the coastal transects 30 km east and west of the main transect (Figure 1.1). Alongshore distributions of temperature were obtained by the same interpolation procedure used for the cross-sectional distributions of section 2.3. Figures 3.4 - 3.6 show daily averaged alongshore temperature patterns at a distance of 5 km from the north shore of Lake Ontario. The vertical line at the centre of each diagram represents the intersection with the main cross section of Lake Ontario; the left side coincides with the coastal transect to the west and the right side with the transect to the east. Daily values

of observed currents are shown by arrows. The results show a wave of warm water progressing from east to west along the north shore and being accompanied by strong westward surface currents. The peak of the warm water wave is seen to pass through the central cross section on August 25. At that time, the daily averaged current at the 10 m level reaches a value of 28 km/day. This indicates that nonlinear processes play a crucial role and that the Kelvin wave takes on the form of a warm front. The dynamics involved in this event will be discussed in the following.

### 3.2 A Simple Model of Coastal Upwelling

The theory of wind-induced upwelling in large lakes contains two basic elements. The first element concerns the forcing of coastal upwelling by local winds. According to Ekman theory, the wind causes a 10-20 m deep surface layer to move to the right of the wind due to the Coriolis force of the earth's rotation. Therefore, an alongshore wind tends to generate a surface current normal to the coast. In order to maintain a mass balance in the coastal zone, the surface drift must be offset by a return current at lower levels and the two are joined together by vertical motion at the coast. Thus, a wind blowing along the shore with the land on the left causes upwelling and vice versa. It has been shown by Charney (1955) that, in presence of stratification, thermocline displacements due to upwelling decrease



rapidly with offshore distance such that coastal upwelling affects only a strip of a few km adjacent to the shore.

The second element of the theory of coastal upwelling deals with the way a pattern of upwelling and downwelling, once established by the wind, propagates around the lake. From the foregoing it follows that a uniform wind blowing over a lake causes upwelling at the shore to the left of the wind and downwelling at the shore to the right but has little or no effect at the upwind and downwind shores where the alongshore component of the wind vanishes. By unfolding the whole shoreline of the lake into a straight shore, it is easy to visualize that the wind-induced thermocline excursions display a wave-like variation along the shore with wavelength equal to the perimeter of the lake. A thermocline wave of this type which, as noted above, is confined to a narrow strip near the coast, is known as an internal Kelvin wave. Such waves move with the speed of gravity waves on the interface between layers of fluid of different density, but due to the Coriolis force of the earth's rotation they remain trapped at the shore and propagate with their right shoulder to the shore (in the Northern hemisphere), that is, counterclockwise around the Great Lakes. This alongshore propagation of warm and cold water after major upwelling events was first observed in Lake Michigan by Mortimer (1963) and a theoretical discussion for idealized lakes was presented by Csanady (1968). This Kelvin-wave mechanism is responsible for the wave propagation seen in Figures 3.5-3.6.

From the foregoing it follows that upwelling at a given location depends not only on local wind forcing but also on the history of wind-induced upwelling at other points around the lake since these disturbances may eventually propagate into the region of interest. On this basis, a workable theory of wind-induced upwelling in large lakes was developed in the early seventies by Bennett (1973), Bennett and Lindstrom (1977), Csanady and Scott (1974), Gill and Clarke (1974), and Clarke (1977). This theory will now be used to explain observed thermocline movements at the north shore of Lake Ontario after the storm of August 9-11, 1982.

Following the outline of the theory, the first step is to compute the alongshore component of the wind stress at regular intervals around the shore, since it is this component which drives the upwelling or downwelling. Given the wind, the alongshore component for each shoreline interval follows from the local orientation of the shoreline relative to the wind direction. By way of illustration, the mean wind stress for the August 9-11 storm is shown by the arrow at the centre of Lake Ontario in Fig. 3.7, and a few alongshore stress components are shown by arrows at selected shore locations. The actual calculations were carried out at 5-km intervals along the shore. The middle of Figure 3.7 shows the same information after the shoreline has been unfolded into a straight line, starting from the west end of the lake and proceeding in clockwise direction around the perimeter. Note that the arrows along the south shore now point to

the left because the shore lies to the right of the local wind direction. The bottom of Figure 3.7 presents the resulting thermocline excursions at the shore measured relative to the thermocline level before the storm. These excursions are proportional to the alongshore stress component integrated over the duration of the storm. According to theory, the proportionality factor is  $(C/\epsilon gh)$  where  $C$  is the internal wave speed,  $\epsilon$  is the density difference across the thermocline,  $g$  is the earth's gravity and  $h$  is the mean thermocline depth. Based on Figure 3.3, estimated values are  $\epsilon=.0015$  and  $h=12$  m, while the empirical model of Bennett and Lindstrom (1977) for Lake Ontario suggests  $C=20$  km/day. The average stress for the three-day storm period is  $.54$  dyne/cm<sup>2</sup>, and thus the theoretical thermocline excursion during the storm is  $18.3$  m. This compares favourably with the observations in Port Hope and Point Breeze (Figure 3.3).

The next step of the calculation is to move the thermocline wave along the shoreline such that the shore is to the right of the direction of propagation. Thus the wave moves to the left in Figure 3.7 as indicated by the open arrows. With the above propagation speed of  $20$  km/day, the wave front would reach Port Hope by August 19, a little earlier than indicated by the observations of Figure 3.6. However, a number of additional effects will modify the shape of the wave as it propagates along the shore. In the first place, allowance must be made for a gradual damping of wave amplitude

due to bottom and shoreline irregularities and mixing across the thermocline. Secondly, although the storm of August 9-11 accounts for most of the subsequent thermocline movements, each of the following wind events makes a similar, but smaller, contribution. Therefore, the above procedure must be repeated for each wind event and the result must be added. Since effects of past winds are gradually damped out, the result at any given time depends primarily on the more recent wind events. Finally, as shown by Bennett (1973), nonlinear effects cause the warm water wave to steepen into a warm front.

To conclude this discussion, a few words may be added regarding the currents associated with wind-induced thermocline movements. According to the above upwelling model, the thermocline excursions are accompanied by alongshore currents in a narrow coastal strip. Above the thermocline, the currents run with the shore on their left in upwelling zones and with the shore on their right in downwelling areas. Thus the surface water flows in the same direction as the wind arrows shown in Figure 3.7. As the wave moves to the left, so does the current pattern. Thus the eastward currents induced by the wind on the north shore will turn to the west as the warm water approaches. The current-meter observations of Figure 3.6 show the expected strong westward surface currents following the passage of the warm front.

### 3.3 Stratification and Topography in Coastal Waters

The time-dependent response of stratified waters to wind may involve a number of different wave forms. The baroclinic response of the shore zones is often dominated by alongshore internal Kelvin waves, while offshore areas may exhibit Poincaré-type waves. Internal Kelvin waves are gravity waves trapped at the right-hand shore (in the northern hemisphere), while internal Poincaré waves are equivalent to inertial motions in homogeneous basins. The water displacements associated with Poincaré waves have time scales shorter than a day and will not be considered here. However, as shown in the foregoing, the time scales of long, internal Kelvin waves may be as long as a few weeks and such waves can be accompanied by strong alongshore currents and large, persistent thermocline excursions. In a closed basin, these waves can be excited by uniform winds, since the associated alongshore component of the wind is periodic around the perimeter of the basin. Along a straight ocean shelf, similar alongshore Kelvin waves may be generated by synoptic-scale meteorological waves.

In addition to this internal response, nearshore water movements will be affected by topography under stratified as well as homogeneous conditions. Again, this topographic response to wind involves alongshore waves. These waves belong to the class of shelf waves and propagate with the shore on their right (in the northern hemisphere) in the same way as internal Kelvin waves. The currents associated

with a pure topographic wave are barotropic and as such, distinguishable from the current shears induced by pure internal Kelvin waves. However, the time scales are comparable and hence it is often difficult to determine whether observed current reversals are caused primarily by baroclinic or topographic effects (Simons, 1975; Csanady, 1976). The matter is complicated by the fact that, in the presence of both topography and stratification, the baroclinic and barotropic responses to wind are not separable and hence internal Kelvin waves and topographic shelf waves do not occur in pure form (Allen, 1975; Wang, 1975). For a review of these various wave effects, the reader is referred to Mysak (1980).

The presence of alongshore waves imposes certain conditions on studies concerned with modelling nearshore upwelling and downwelling and associated currents. In the first place, longshore variations imply that the problem is essentially three-dimensional. In the second place, coupling of baroclinic and topographic modes precludes the use of the familiar internal wave equations without regard to vertical-mean flow. Since the resulting model is fairly complicated, the question arises to what extent the same phenomena can be simulated by simpler and less expensive models. This is one of the problems considered in the following.

Another aspect of stratified models is the vertical structure of such models. The simplest version is a model consisting of two layers of fluid of constant density separated by a moving, imper-

meable interface. In recent years, multi-level models have been introduced which compute temperatures and currents at an arbitrary number of fixed levels. This type of model can deal with more general temperature gradients but it may be subject to greater damping of internal waves and erosion of the thermocline due to numerical truncation errors. It is of interest to use both of these models to simulate the same observed upwelling event and to investigate which level of complexity is required to arrive at acceptable results. This is the second subject to be addressed here.

### 3.4 Two-Layer Response to Alongshore Wind Wave

Before proceeding to simulation of an observed upwelling event, effects of longshore waves and coupling of internal and external modes will be evaluated for the nearshore location of interest. For simplicity, this study employs the conventional two-layer model. The rigid lid approximation is used to suppress the time rate of change of the free surface in the vertically integrated continuity equation. This permits the definition of a streamfunction for the vertical-mean flow but does not imply that the free surface at all times coincides with its equilibrium level. It only eliminates free-surface perturbations associated with external gravity waves.

Let  $h$  be the variable depth of the interface below the undisturbed surface level and  $\eta$  the free surface elevation, so the upper layer thickness is  $h' = h + \eta$ . Let  $H$  be the water depth,  $D = h(H-h)/H$  the equivalent depth for the internal mode,  $\vec{v}$  the vertical-mean current,  $\psi$  the corresponding stream function and  $\vec{v}'$  the current shear between the upper and lower model layers. The linearized two-layer equations can then be written in terms of these variables as follows

$$\nabla \cdot (H\vec{v}) = 0, \quad H\vec{v} = \vec{k} \times \nabla \psi \quad (1)$$

$$\frac{\partial \vec{v}}{\partial t} = f\vec{k} \times \vec{v} - \nabla(g\eta) + \frac{H-h}{H} \nabla(\epsilon gh') + \frac{\tau_s}{\rho H} - \frac{\tau_b}{\rho H} \quad (2)$$

$$\frac{\partial h'}{\partial t} + \nabla \cdot (D\vec{v}') + \nabla \cdot (h\vec{v}) = 0 \quad (3)$$

$$\frac{\partial \vec{v}'}{\partial t} = f\vec{k} \times \vec{v}' - \nabla(\epsilon gh') + \frac{\tau_s}{\rho h} + \frac{\tau_b}{\rho(H-h)} - \frac{\tau_i}{\rho D} \quad (4)$$

where  $f$  is the Coriolis parameter,  $g$  the earth's gravity,  $\epsilon = \Delta\rho/\rho$  the density difference across the interface,  $\tau_s$ ,  $\tau_b$ ,  $\tau_i$  the surface, bottom and interface stress, respectively,  $\nabla$  the gradient operator and  $\vec{k}$  the vertical unit vector. In the following,  $h$  will be treated as a



constant equal to the mean thermocline depth, and  $h'$  is the local, instantaneous deviation of the upper layer depth from this mean value. Note that a positive value of  $h'$  represents a downward displacement of the interface.

Internal friction is taken to be proportional to the velocity shear across the interface, while bottom friction is proportional to the bottom current, thus

$$\frac{\tau_i}{\rho} = c_i \vec{v}'; \quad \frac{\tau_b}{\rho} = c_b (\vec{v} - \frac{h}{H} \vec{v}') = \frac{c_b}{H} (\vec{k} \times \nabla \psi - h \vec{v}') \quad (5)$$

where the coefficients have dimensions of velocity. The corresponding decay times for interfacial and bottom friction are

$$T_i = \frac{D}{c_i} \quad T_b = \frac{H}{c_b} \quad (5a)$$

Consider a straight shore aligned with the  $y$ -coordinate with a uniform shelf profile so the depth is a function of  $x$  only. The wind blows parallel to the shore and varies periodically along the shore. As noted above, a similar situation arises if a uniform wind blows over a closed basin. First ignore friction and consider the response to a wind wave which progresses along the shore, thus

$$\tau_{sx} = 0, \quad \tau_{sy} = \tau_0 e^{i(ky - \sigma t)} \quad (6)$$

where  $k$  is the alongshore wavenumber,  $\sigma$  the frequency, and  $\tau_0$  a constant. The solutions will be of the form

$$\psi = \psi_0(x) e^{i(ky - \sigma t)} \quad h' = h'_0(x) e^{i(ky - \sigma t)} \quad (7)$$

After combining the mean flow equations (1-2) into the vorticity equation and eliminating the shear velocities from equations (3-4), the resulting system of equations is

$$\left[ \frac{d}{dx} (H^{-1} \frac{d}{dx}) - k^2 H^{-1} + \frac{kf}{\sigma} \frac{dH^{-1}}{dx} \right] \psi_0 - \frac{kh}{\sigma} \frac{dH^{-1}}{dx} \varepsilon g h'_0 = \frac{dH^{-1}}{dx} \frac{i\tau_0}{\sigma\rho} \quad (8)$$

$$\begin{aligned} \left[ \frac{d}{dx} (D \frac{d}{dx}) - k^2 D - \frac{kf}{\sigma} \frac{dD}{dx} - \frac{f^2 - \sigma^2}{\varepsilon g} \right] \varepsilon g h'_0 - \frac{(f^2 - \sigma^2)kh}{\sigma} \frac{dH^{-1}}{dx} \psi_0 \\ = (kD + \frac{f}{\sigma} \frac{dD}{dx}) \frac{i\tau_0}{\rho h} \end{aligned} \quad (9)$$

With boundary conditions of zero normal velocities at the shore

$$\psi_0 = 0, \quad \left( \frac{\sigma}{f} \frac{d}{dx} - k \right) \varepsilon g h'_0 = \frac{i\tau_0}{\rho h} \quad \text{at the shore.} \quad (10)$$

For  $\tau_0 = \text{real}$ , the solutions are purely imaginary, either positive or negative. A positive value represents a  $90^\circ$  phase lag behind the wind, a negative value means that the solution is  $90^\circ$  ahead of the wind. When the forcing frequency becomes equal to a normal mode frequency, resonance occurs and the solutions change sign.

Without the last terms on the left of (8)-(9) and in the absence of forcing, solutions of the first equation are topographic shelf waves and a solution of the second equation is the internal Kelvin wave. The last terms on the left of the equations show that the bottom slope causes a coupling of these two wave forms. The effect of the shear flow on the mean flow is due to the fact that bottom pressure enters in the vorticity balance of the mean flow in the presence of depth variations (Welander, 1959). Since the bottom pressure is partly determined by thermocline variations, an internal Kelvin wave propagating over a sloping bottom is a source of mean flow vorticity. On the other hand, the effect of the mean flow on the shear flow enters through the last term of the continuity equation (3) for the internal flow. This term becomes non-zero if the mean flow crosses depth contours, and thus the cross-slope flow of topographic waves will generate baroclinic flow. Allen (1975) has evaluated these coupling effects and found that the barotropic motion caused by the Kelvin wave is of the same order as the effect of topographic variations on the Kelvin wave itself. It would, therefore, be inconsistent to include topography in the vertical-shear equations without

allowing for coupling with barotropic motion. Allen also showed that the baroclinic effect on a barotropic shelf wave is weaker than the barotropic effect on an internal Kelvin wave for relatively weak stratification such as that encountered in Lake Ontario.

Solutions of the coupled set of equations for the Lake Ontario cross section of Figure 1.1 can readily be obtained by numerical methods. After replacing the derivatives by finite differences, the resulting system of equations may be conveniently solved by the method of Lindzen and Kuo (1969) as done for a similar problem by Wang (1975). Figure 3.8 shows alongshore velocities 5 km off the north shore generated by winds of different periods and amplitude equal to  $1 \text{ dyne/cm}^2$ . The alongshore wavelength is taken to be twice the length of Lake Ontario, that is, 600 km, the thermocline depth is 12 m, the density difference is  $1.5 \times 10^{-3}$  and the grid mesh is 2 km. The top part of the figure presents results obtained without allowing for coupling of mean and shear flow; the lower part includes this coupling. The period of the shelf wave is 9.5 days in the absence of coupling effects and 9.1 days in the presence of shear flow. The period of the Kelvin wave is much more reduced by coupling effects, from 27 days without the mean flow to 21.2 days in the presence of the mean flow. Note that, when coupled, both the mean and shear flows have resonances at the shelf wave period and the Kelvin wave period. Thus the shelf wave currents have a baroclinic component and the Kelvin wave currents have a barotropic component.

To place these results in the proper perspective, it is important to realize that the Kelvin wave speed in a two-layer model with variable depth is strongly affected by the depth at the shore. In two-layer models the bottom layer must have a finite value at the shore but the choice of this depth is quite arbitrary in cases where the actual thermocline intersects the bottom. In the present calculations, the lower layer depth at the shore was set at 2 m. Computations for different values of this depth showed that the Kelvin wave period is reduced by as much as a quarter if the lower layer depth at the shore is increased to equal the upper layer depth. This change of period is of the same magnitude as that introduced by coupling of mean and shear flows. This implies that accurate estimates of Kelvin wave speeds can be obtained only if coupling effects are included and the lower layer depth at the shore is assigned a very small value. The latter, however, implies that the thermocline will intersect the bottom as soon as the slightest forcing is applied and hence the linearized equations become invalid. This matter will be discussed in a later section of this chapter when the two-layer model is compared with a multi-level temperature model.

Another aspect of the coupling of barotropic and baroclinic flows which has not been considered yet is the effect of friction. According to the friction formulations (5), internal friction will affect only the shear flow and hence can have at most an indirect effect on the mean flow due to the inviscid coupling mechanism.

However, bottom friction leads to additional coupling of mean and shear flows as will be illustrated presently.

### 3.5 Two-Layer Response to Observed Wind

This section will be concerned with a two-layer simulation of an observed upwelling event on the northshore of the Lake Ontario cross-section shown in Figure 1.1. As argued above, this type of event is essentially three-dimensional and hence its simulation would require a model of the whole lake with actual topography and shore configuration. Such a complete model will be discussed at the end of this section, but it is worthwhile to consider first a much more economical model based on the above mentioned fact that the nearshore response of a closed basin to uniform wind is equivalent to the response of a straight shelf to a periodic alongshore wind. Furthermore, it is also interesting to see to what extent the same event can be simulated by an even simpler model of a straight channel with a uniform alongshore wind and consequently no allowance for alongshore waves.

Starting with the intermediate model, we consider again the model used in the last section but with the wind having the form of a standing wave with arbitrary time variation

$$\tau_{sx} = 0 \quad \tau_{sy} = \tau_0(t) \cos ky \quad (11)$$

The solutions for all variables will be of the form

$$\psi = \text{Re} [\psi_0(t, x) e^{iky}] \quad (12)$$

where  $\psi_0$  is a complex variable. The solutions of interest are the values of the variables at the location of maximum alongshore wind,  $y = 0$ , and hence the solutions are given by the real parts of the complex variables.

Upon replacing the mean flow equations(1-2) by the vorticity equation and substituting solutions of the form (12) into this equation and the shear equations (3-4), the following equations are obtained for the complex variables

$$\frac{\partial h'_0}{\partial t} = - \frac{\partial}{\partial x} (Du'_0) - ikDv'_0 + ikh \frac{dH^{-1}}{dx} \psi_0 \quad (13)$$

$$\frac{\partial u'_0}{\partial t} = f v'_0 - \epsilon g \frac{\partial h'_0}{\partial x} + \frac{\tau_{bx}}{\rho(H-h)} - \frac{\tau_{ix}}{\rho D} \quad (14)$$

$$\frac{\partial v'_0}{\partial t} = - f u'_0 - i \epsilon g k h'_0 + \frac{\tau_{by}}{\rho(H-h)} - \frac{\tau_{iy}}{\rho D} + \frac{\tau_n}{\rho h} \quad (15)$$

$$\left[ \frac{\partial}{\partial x} (H^{-1} \frac{\partial}{\partial x}) - k^2 H^{-1} \right] \frac{\partial \psi_0}{\partial t} = ifk \frac{dH^{-1}}{dx} \psi_0 - i \epsilon g k h \frac{dH^{-1}}{dx} h'_0$$

$$+ \frac{ik\tau_{bx}}{\rho H} - \frac{\partial}{\partial x} \left( \frac{\tau_{by}}{\rho H} \right) + \frac{dH^{-1}}{dx} \frac{\tau_n}{\rho} \quad (16)$$

$$\frac{\tau_{bx}}{\rho} = -\frac{C_b}{H} (hu'_0 + ik \psi_0) \quad \frac{\tau_{ix}}{\rho} = c'_i u_0 \quad (17)$$

$$\frac{\tau_{by}}{\rho} = -\frac{C_b}{H} (hv'_0 - \frac{\partial \psi_0}{\partial x}) \quad \frac{\tau_{iy}}{\rho} = c'_i v'_0 \quad (18)$$

The system of equations (13-18) is solved for the cross section of Figure 1.1 with the use of a staggered grid. The streamfunction  $\psi$  and the transverse velocity shear  $u'$  go to zero at the shores and are computed at integer multiples of the grid interval. The thermocline excursion  $h'$  and the alongshore current shear  $v'$  are computed at the mid-points between the streampoints. The Coriolis terms in (14-15) are computed by averaging over two adjacent gridpoints. A forward time extrapolation scheme is used except for the Coriolis terms which are centred in time. This is done in (14-15) by using the old value of the  $v'$  component in the first equation and then using the new value of the  $u'$  component in the second equation. Finally, the solution of (16) is completed by inversion of the tri-diagonal matrix.

First, effects of friction are evaluated by computing the response to a wind impulse of 1 dyne/cm<sup>2</sup> lasting for 16 hours. A forcing of this time scale tends to suppress near-inertial waves and thus brings out more clearly the solutions of interest. The solutions



for the alongshore currents near the north shore are presented in Figure 3.9. The top part shows the inviscid case. The periods are seen to agree with the resonance periods at the bottom of Figure 3.8. The middle of Figure 3.9 shows results for an internal friction coefficient of 0.01 cm/s. According to (5a) the corresponding decay time for a depth of 50 m and thermocline depth of 12 m is about 1 day. As expected, the effect of internal friction is mostly confined to the shear flow. The bottom of Figure 3.9 presents the case of bottom friction with a coefficient of 0.05 cm/s. Again, the decay time for a depth of 50 m is about 1 day according to (5a). This results in considerable damping of the mean flow, some damping of the shear flow, a substantial increase in the period of the mean flow and a slight decrease in the period of the shear flow. This illustrates the complex interaction of mean and shear flows due to bottom friction, which is additional to the inviscid coupling effect discussed previously. An example of this coupling effect was also found in the three-dimensional model results of Simons (1975), which showed that the topographic normal modes of Lake Ontario were strongly modified by stratification.

Application of Eqs. (13-18) to model an observed upwelling event is illustrated in Figure 3.10. The top of the figure shows the eastward, alongshore component of the wind stress in dynes/cm<sup>2</sup> as computed from winds measured over water with a drag coefficient of  $1.2 \times 10^{-3}$ . The second panel of Figure 3.10 presents observed depths of

the  $10^{\circ}$  isotherm 5 km from the north shore (solid line) and in deep water (broken line). The complete records (Figure 2.14) show that stratification in mid-lake started by the end of June, with the  $10^{\circ}$  isotherm rapidly descending to 10 m and then remaining near that level. Near the northshore, the  $10^{\circ}$  isotherm descended more slowly and reached the 10 m level for the first time on July 25. On that date, the thermocline appears fairly horizontal over the whole cross section of Figure 1.1 and hence this date is taken as the starting time for the model. As before, the alongshore wavelength is 600 km, the grid mesh is 2 km and friction is omitted. The computed thermocline depths 5 km from the northshore are presented in the third panel of Figure 3.10 for two values of the density gradient. The higher value corresponds to the observed temperatures in deep water; the lower value is obtained from nearshore observations at the start of the simulations.

The apparent similarities between these model results and the observations raise the question whether the solutions are directly forced by the local wind or significant contributions are made by alongshore waves. To answer this question, a two-layer channel model was used with wind stress uniform alongshore. Following Bennett (1974), the longshore internal pressure gradient is ignored but not the external pressure gradient, since the propagation of end effects is much faster along the free surface than along the thermocline. The internal-mode equations are obtained from (3-4) by discarding along-

shore derivatives. The transverse component of the mean flow must vanish, in view of the continuity equation and the boundary conditions at the shore. The longshore component of the mean flow follows from (2), with the surface gradient determined by the condition of zero alongshore transport through the cross section. Since the mean flow is directed along depth contours, the inviscid coupling of mean and shear flows due to the last term of Eq. (3) cannot occur, so the only coupling is due to friction.

Inviscid solutions for the infinitely long stratified channel are known (e.g. Csanady, 1973; Bennett, 1974). For a constant alongshore wind the thermocline excursion increases linearly with time, and hence the thermocline depth is the time-integral of the wind stress. It is apparent from the top of Figure 3.10 that the wind blows predominantly towards the east and hence the thermocline will gradually move upward. For this reason, a model start on July 25 is unsuitable. If, however, the model is started on August 3 when the observed thermocline excursion tends to vanish again, then the solution approaches that of the wave model for the duration of the upwelling event. Such solutions are shown at the bottom of Figure 3.10 for the inviscid case and the case of internal friction. After the upwelling event the thermocline continues to move upward due to light eastward winds.

Comparison of the solutions of the wave model and the infinite channel model shown in panels (c) and (d) of Figure 3.10,

respectively, confirm that the thermocline depth is not solely determined by local wind forcing. In particular, the sudden deepening of the thermocline in late August is not primarily caused by the wind reversal at that time but by alongshore wave effects. This is confirmed by temperature observations east and west of our cross section of Lake Ontario shown in Figures 3.6-3.7. Between August 20 and August 26, they show a wave of warm water propagating westward along the northshore. Thus, while the wind-forced upwelling is quite uniform alongshore (and, hence, can be simulated by a channel model), the subsequent relaxation of the thermocline takes on the form of a wave and, hence, for time scales of a few weeks or longer, alongshore variations must be included in an upwelling model. The wave model of Eqs. (11-18) presents the lowest-order approximation to such variations and, as such, encompasses the three-dimensional character of the problem.

While the wave model appears to give surprisingly good results in return for relatively little effort, a more realistic simulation of the present upwelling event requires a full-scale model of the whole lake. Thus, experiments were carried out with a two-layer model with a 5-km grid using the actual bathymetry of Lake Ontario and also with a rectangular model having the same dimensions as Lake Ontario and a longitudinally uniform depth profile corresponding to Figure 1.1. The effects of the relatively large gridsize on the internal Kelvin wave and the topographic waves were first

investigated with the above wave model. The solutions were quite comparable to those of the 2-km grid but the Kelvin wave period is a little shorter on the 5-km grid than on the 2-km grid, since its speed is effectively determined by the depth of the grid point nearest to the shore.

The experiments with the two-layer model of Lake Ontario brought out some numerical problems. In the absence of friction or diffusion, considerable grid dispersion occurs for long periods of integration. The problem is caused by irregular topography and shoreline features and, hence, it is reduced as the basin shape and bathymetry become more regular. Actually, for a rectangular basin with constant depth, the solution closely approaches the exact solution which can be obtained by graphical means (Csanady and Scott, 1974; Simons, 1980). In the presence of friction or diffusion, the grid dispersion problem is generally reduced and acceptable solutions are obtained as shown by the three-dimensional model verification study of Simons (1975). In that case, current reversals and baroclinic effects in response to strong wind forcing were properly reproduced for time scales of a week or so, but this type of model is not suitable for sustained alongshore wave propagation. Bennett (1977) has analyzed this problem and concluded that high nearshore model resolution as well as low friction were needed, but our own experiments suggest that his improved results may have been partly due to the simpler basin configuration of his fine-grid model as compared to his

coarse-grid model. In any case, numerical simulation of inviscid baroclinic and barotropic wave propagation over highly irregular topography remains a difficult problem.

### 3.6 Multi-Level Temperature Model

The two-layer model used in the foregoing has certain shortcomings. In the first place, it requires a well-defined thermocline and does not allow for more gradual vertical temperature gradients and seasonal changes of stratification due to long-term surface heating and cooling. In the second place, the linearized two-layer model requires finite layer depths at the shore, which implies that the water depth at the shore must be greater than the mean thermocline depth. In the case of the cross section of Figure 1.1, this means that the northshore of the two-layer model is about 2 km removed from the actual northshore. It is possible to use a nonlinear version of the two-layer model with the thermocline intersecting the bottom or the free surface, but experiments with such models have not been encouraging. The problem is, of course, that the intersection points do not, in general, coincide with the model grid points.

A multi-level temperature model eliminates these difficulties by predicting temperatures and currents at fixed levels and thus allowing for arbitrary stratification and seasonal variations of surface heat fluxes. The model equations are

$$\frac{\partial \vec{v}}{\partial t} = \frac{\partial}{\partial z} \left( A \frac{\partial \vec{v}}{\partial z} \right) + f \vec{v} \times \vec{k} - \nabla(g \eta) - \nabla P \quad (19)$$

$$\frac{\partial T}{\partial t} = \frac{\partial}{\partial z} \left( K \frac{\partial T}{\partial z} \right) - \nabla \cdot (\vec{v} T) - \frac{\partial}{\partial z} (w T) \quad (20)$$

$$\frac{\partial w}{\partial z} = - \nabla \cdot \vec{v} \quad P = -6.8 \times 10^{-6} \int_z^\eta g(T-4)^2 dz \quad (21)$$

with boundary conditions at the surface and the bottom

$$A \frac{\partial \vec{v}}{\partial z} \Big|_s = \frac{\vec{\tau}_s}{\rho} \quad A \frac{\partial \vec{v}}{\partial z} \Big|_b = \frac{\vec{\tau}_b}{\rho}, \quad K \frac{\partial T}{\partial z} \Big|_s = \frac{q_s}{\rho C_p}, \quad \frac{\partial T}{\partial z} \Big|_b = 0 \quad (22)$$

and the normal velocity components going to zero at the lateral boundaries and at the bottom. The notation is essentially the same as before, thus  $z$  is the vertical coordinate measured upward from the mean surface level,  $\nabla$  is the horizontal gradient operator,  $\vec{k}$  the vertical unit vector,  $\vec{v}$  the horizontal current vector,  $w$  the vertical velocity,  $T$  the temperature in  $^{\circ}\text{C}$ ,  $f$  the Coriolis parameter,  $g$  the earth's gravity,  $\eta$  the free surface elevation,  $P$  the baroclinic pressure,  $A$  and  $K$  the vertical eddy viscosity and heat diffusivity,  $\tau_s$  and  $\tau_b$  the surface and bottom stress, and  $q_s$  the downward surface heat flux, where  $\tau_s$  and  $q_s$  are prescribed and  $\tau_b$  is proportional to the square of the bottom current.

The dynamic principles of this model are the same as those of the two-layer model. The governing equations are the equations of motion (19), the thermodynamic energy equation (20) and the principle of mass conservation, (21). Vertical accelerations are neglected, which leads to quasi-hydrostatic flow. Density variations are ignored except where they influence buoyancy and so the water is effectively incompressible. The last part of (21) approximates the density of fresh water by a quadratic function of temperature with maximum density at 4°C. Nonlinear acceleration terms in the equations of motion are neglected the same as in the linearized two-layer model. However, nonlinearity is an essential feature of the temperature equation, with temperature changing due to three-dimensional advection by currents. If this equation were linearized by using a mean vertical temperature gradient, the model would essentially reduce to the linearized two-layer model. As it is, however, it is rather similar to a two-layer model with varying layer depths.

It is common in multi-level models to simulate effects of turbulence by analogy to the gradient diffusion concept such that turbulent friction and heat diffusion are parameterized by eddy viscosities and diffusivities. Thus, a model of this type often includes horizontal and vertical diffusion of momentum and heat. However, most of these effects are not essential and, in fact, should be excluded when comparing a multi-level temperature model with a two-layer model as will be done in the following. The only essential



form of turbulent viscosity is the shear stress between model layers so as to transfer the surface wind stress to subsurface model layers, at least to the model layers above the thermocline. At the thermocline, the shear stress may go to zero as in a two-layer model without interface friction. Similarly, the only essential heat diffusion is that required to counteract any vertical instability that might be generated by temperature advection and to transfer any surface heat flux to subsurface layers.

In a previous study (Simons, 1981) thermocline models were compared to evaluate their capability for simulating observed seasonal stratification cycles in Lake Ontario. The most satisfactory results were obtained from a semi-empirical formulation, which for stable stratification takes the form

$$K = \frac{\epsilon}{f} \left| \frac{\tau_s}{\rho} \right| e^{z/\delta} (1 + \sigma Ri)^{-1} \quad (23)$$

where  $\epsilon$  is a coefficient of order  $10^{-2}$ ,  $\delta$  is an Ekman depth equal to  $2(\epsilon \tau_s / \rho) / f$ ,  $\sigma$  is approximately equal to 5 and  $Ri$  is the Richardson number defined as

$$Ri = 6.8 \times 10^{-6} g \frac{\partial(T-4)^2}{\partial z} \left| \frac{\partial \tau}{\partial z} \right|^{-2} \quad (24)$$

The model calculations to be discussed here will be concerned with relatively short time scales, so that surface heat fluxes may be ignored. Vertical diffusion of heat is invoked only to counteract any vertical instability that may occur. In that case, the unstable profile is changed instantaneously to uniform vertical temperature, which is equivalent to infinitely large diffusion of heat. The vertical eddy viscosity is assumed to have a similar form to (23):

$$A = 10^2 \left| \frac{\tau_s}{\rho} \right| (1 + 5\text{Ri})^{-1} \quad (25)$$

where the value of  $f$  at middle latitudes has been used and the exponential variation has been ignored. As in many conventional formulations of this type, the resulting mixing of momentum increases with wind stress and tends to vanish near the thermocline where the static stability becomes large. It is interesting to note that earlier verification studies of three-dimensional models (e.g. Simons, 1975) independently led to the same choice of the numerical value of the eddy viscosity in the surface layers.

An important aspect of the heat advection equation of a multi-level model is the problem of numerical diffusion introduced by finite-difference formulations. Examples have been discussed by Simons (1980). Thus, even in the absence of explicit diffusion of

heat, an initially steep temperature gradient cannot be sustained indefinitely in a multi-level temperature model. As such, the model is less suitable for simulating long-term internal wave propagation than a linearized model like the two-layer model used above. However, this problem may be reduced by using sufficiently high vertical resolution in the region of the thermocline.

Numerical solution of the above equations on various three-dimensional grids has been discussed extensively by Simons (1980), and the reader is referred to that monograph for details. The particular choice made for the present computations will be briefly summarized.

A number of fixed horizontal levels is placed at selected intervals along the vertical. Temperature and currents are defined as averages for the layers between two adjacent levels and predicted from (19-20) with the baroclinic pressure at the mid-point of each layer determined from the second part of (21). The vertical velocity is determined at the levels themselves by using the continuity equation given by the first part of (21). In the horizontal, the variables are staggered to form a single Richardson lattice with temperature, pressure and vertical velocity being defined at the center of a grid element and horizontal velocity components on the sides.

Centered differences are used for the space derivatives. Time extrapolation of the temperature is based on the Lax-Wendroff procedure, which first predicts the temperature half a step forward and

then uses this temperature on the right-hand side of the equation to extrapolate the temperature a complete step in time. An upstream temperature prediction was also tried but the resulting smoothing appeared prohibitive. Time extrapolation of the Coriolis terms employs the forward-backward procedure discussed in conjunction with Eqs. (14-15). The vertical diffusion terms are treated with a backward implicit scheme. This is necessary because the coefficient (25) becomes very large during periods of high winds, and hence the stability condition for a forward integration scheme would lead to an undesirably short time step. In order to use this implicit scheme for the diffusion terms only, the equations are broken down into two parts. At each time step of the extrapolation, we first solve

$$\frac{\partial \vec{v}}{\partial t} = \frac{\partial}{\partial z} \left( A \frac{\partial \vec{v}}{\partial z} \right) \quad \frac{\partial T}{\partial t} = \frac{\partial}{\partial z} \left( K \frac{\partial T}{\partial z} \right) \quad (26)$$

using the future, unknown values of the variables on the right. The resulting system of equations is coupled only with respect to each vertical column and is readily solved by tri-diagonal matrix inversion. After this is done, the time step is completed by adding changes of variables due to the remaining terms in the equations.

As noted earlier, three dimensional solutions of these equations have been obtained by a number of investigators, usually with fairly coarse horizontal and vertical resolutions. The present study

will deal with only one horizontal dimension in order to concentrate on a more detailed horizontal and vertical representation and to compare the results with the two-layer simulations presented before. The model is an infinite channel model with transverse depth profile corresponding to Figure 1.1 and forced by a uniform wind. The limitations of this type of model were pointed out with reference to the bottom of Figure 3.10 which shows that the model cannot be expected to perform adequately for time scales longer than a week or so.

The numerical treatment of the channel equations is the same as for the more general model described above except for the barotropic pressure gradient. In the general model, it is convenient to derive an equation for the vertically integrated flow to determine the surface pressure. Since it can be shown that only this equation is affected by the stability condition associated with the fast surface waves, it is common to use a relatively large time step of the order of 1 hr for the internal flow and temperature predictions. The equation for the vertically integrated flow can then be solved with the same time step by imposing a rigid lid condition or by using the semi-implicit scheme which is often used in meteorology (see, e.g. Simons, 1980). For the present channel model the situation is very simple. Following Bennett (1974), the transverse external pressure gradient is determined from the condition that the vertically integrated cross-shore flow must vanish everywhere and the longitudinal pressure component follows from the conditions that this component

must be uniform across the channel and that the alongshore flow integrated over the cross section must vanish. Thus, at each time-step, the currents are predicted first without regard to external pressure and then corrected to satisfy these conditions.

The vertical structure of the model consists of 20 layers with uniform depths of 1.5 m down to 30 m and one single, variable-depth layer below 30 m. The horizontal grid mesh is equal to 2 km over the whole cross section, but the mesh is reduced to 0.5 km in a 10-km-wide nearshore zone. The coupling of fine and coarse grids does not allow for feedback from the fine grid. Thus, the solution is first determined for the whole cross section using the coarse grid and then this solution is used to specify boundary conditions for the fine grid. It may be noted that the depths in the temperature points of the fine grid must be consistent with those of the coarse grid such that the volume is the same in both grids. Otherwise, sustained heat advection into or out of the nearshore zone will cause temperature discontinuities at the boundary of the fine grid.

An example of the application of this model is shown in Figure 3.11. The simulated event is the same as that considered in Figure 3.10. The left-hand side of Figure 3.11 shows three observed isotherms, 5 km from the Port Hope shore. The right-hand side of Figure 3.11 shows the corresponding isotherms computed with the channel model starting from observed temperatures on August 3 and assuming no motions at that time. The divergence of the isotherms

during downwelling and the subsequent upwelling appear to be properly reproduced. The error in the prediction of the depth of the downwelling seems to be due to the first two days of the simulation; the magnitude of the subsequent upwelling is more accurately modelled.

The right-hand side of Figure 3.11 also shows results from a two-layer channel model. The short dashes represent results at a distance of 5 km from the model shore. Since the two-layer model requires a finite lower layer depth at the shore, the model shore is approximately 2 km away from the actual shore. Thus, it may be more realistic to compare model results at a distance of 3 km from the model shore. These results are presented by the long dashes in Figure 3.11 and show remarkable agreement with the  $10^{\circ}$  isotherm of the multilayer model. This suggests that a linearized two-layer model can produce quite satisfactory simulations of upwelling events even if the thermocline excursions are too large to justify linearization.

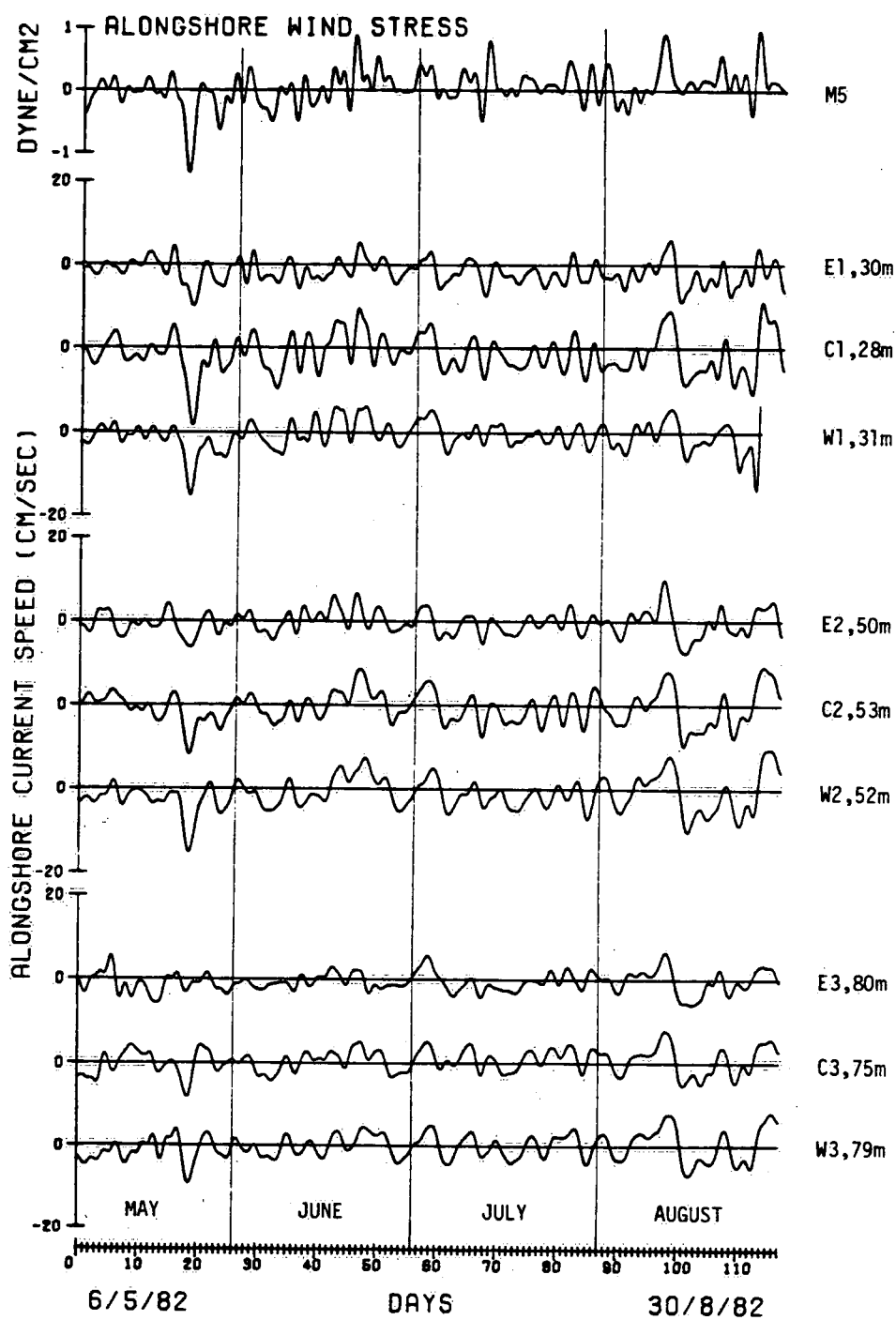


Fig. 3.1 Alongshore component of bottom currents in the eastern, central and western coastal transects off the north shore of Lake Ontario.



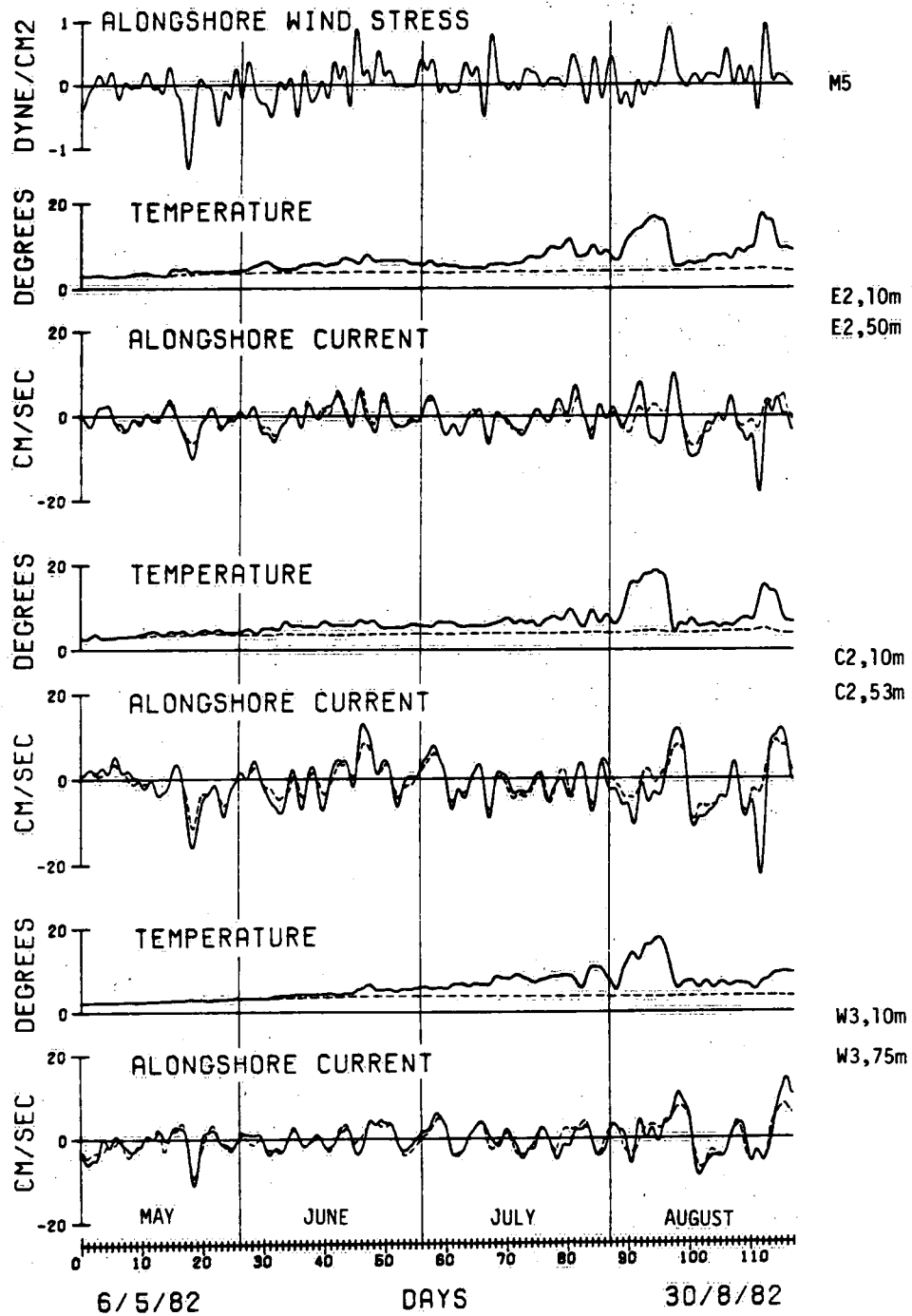


Fig. 3.2 Temperature and currents at the surface (solid lines) and bottom (dashed) in the eastern, central and western coastal transects of the north shore of Lake Ontario.

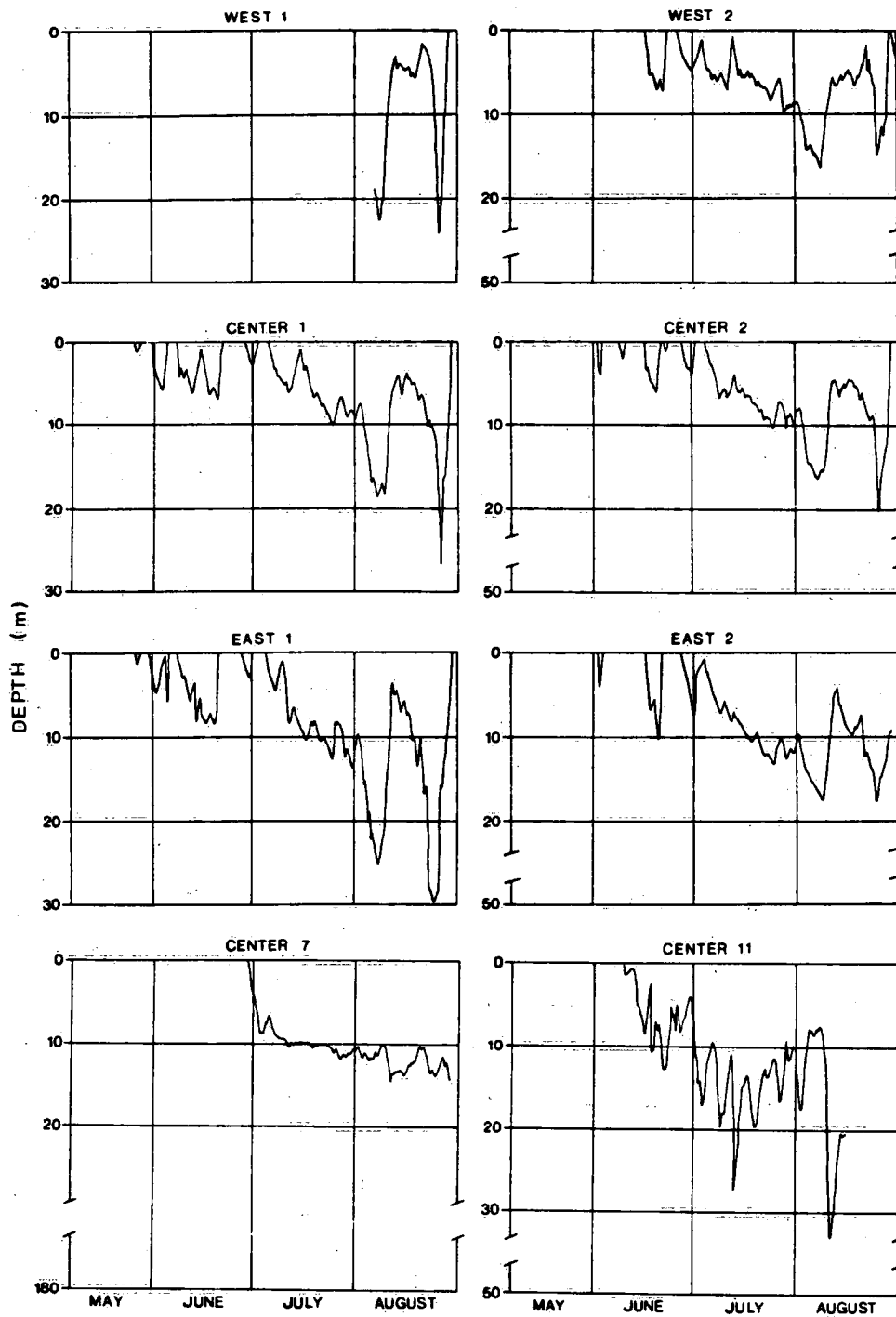


Fig. 3.3 Depth of 10-degree isotherm measured by Fixed Temperature Profilers in Lake Ontario.

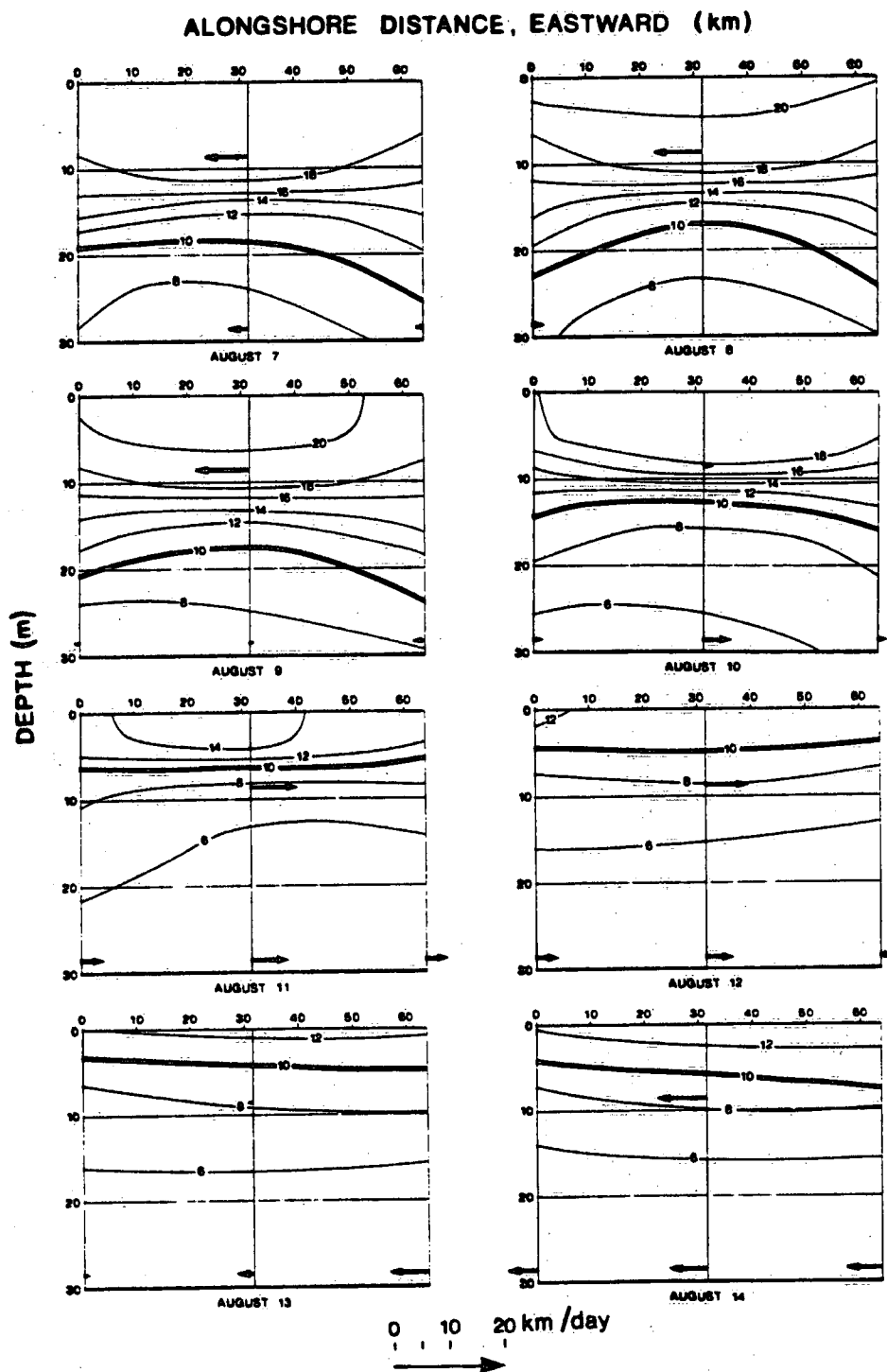


Fig. 3.4 Daily averaged alongshore temperature variations 5 km off the north shore of Lake Ontario. Daily-mean currents shown by arrows.

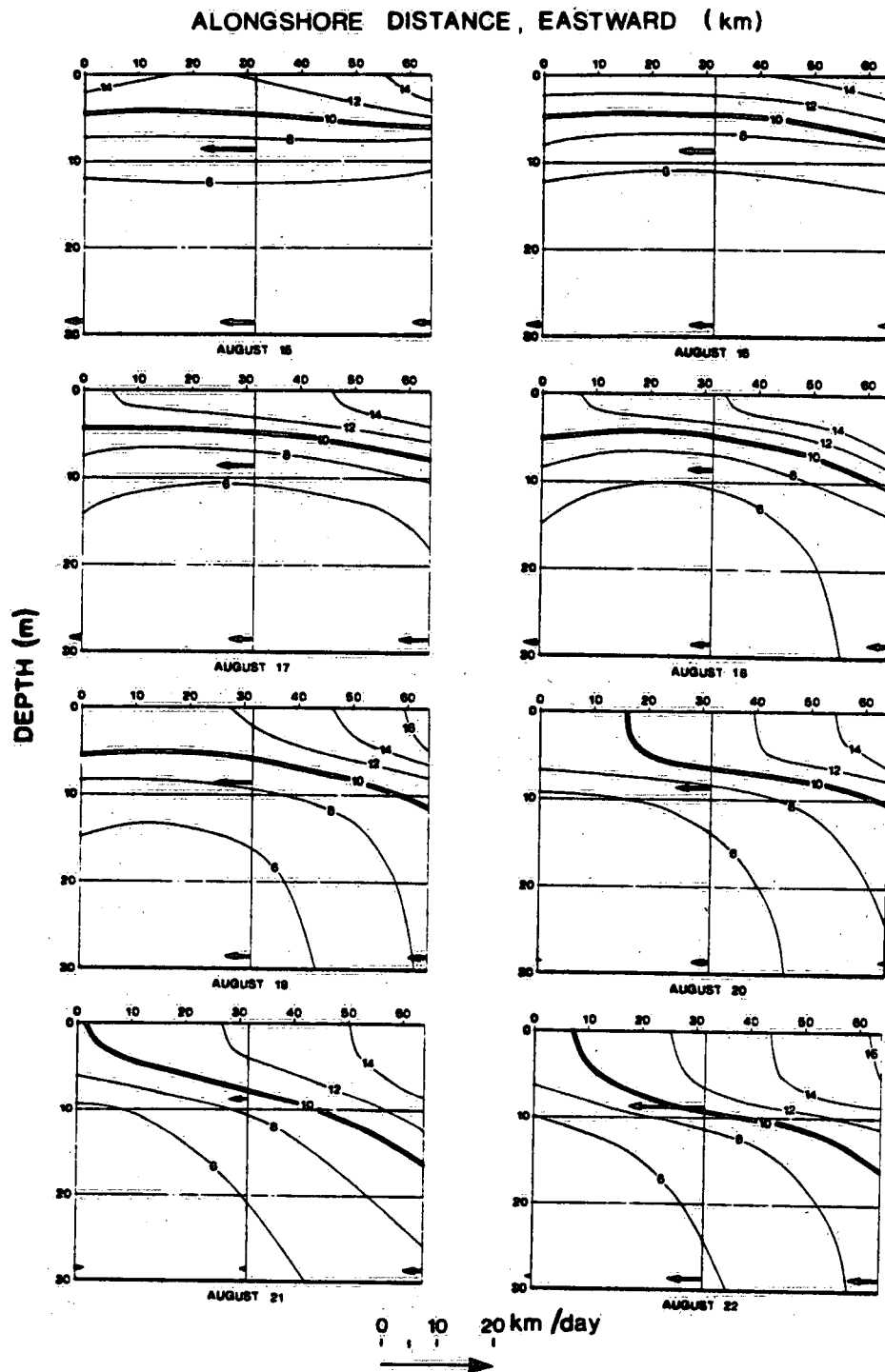


Fig. 3.5 Continuation of Fig. 3.4.

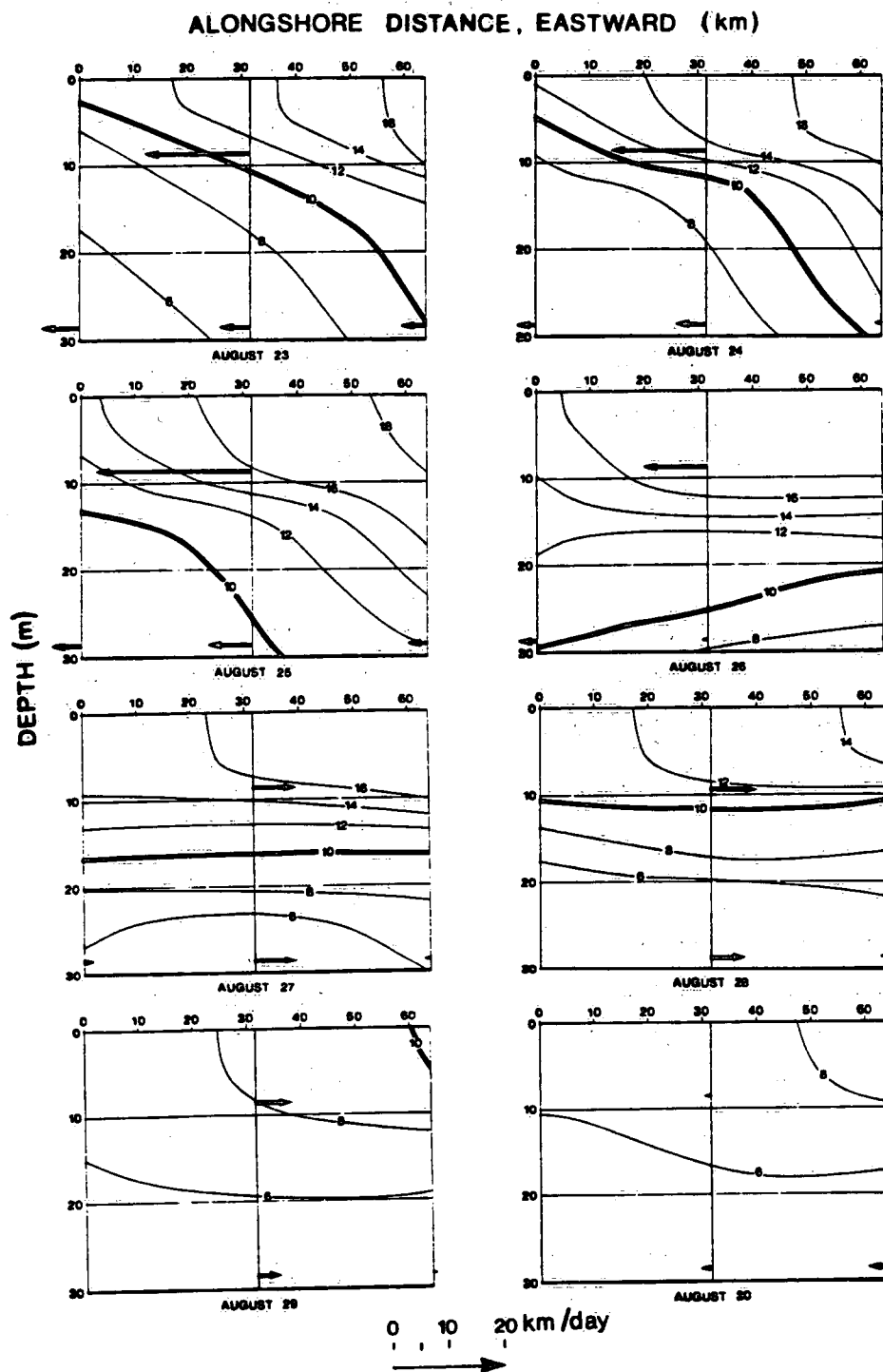


Fig. 3.6 Continuation of Fig. 3.5.

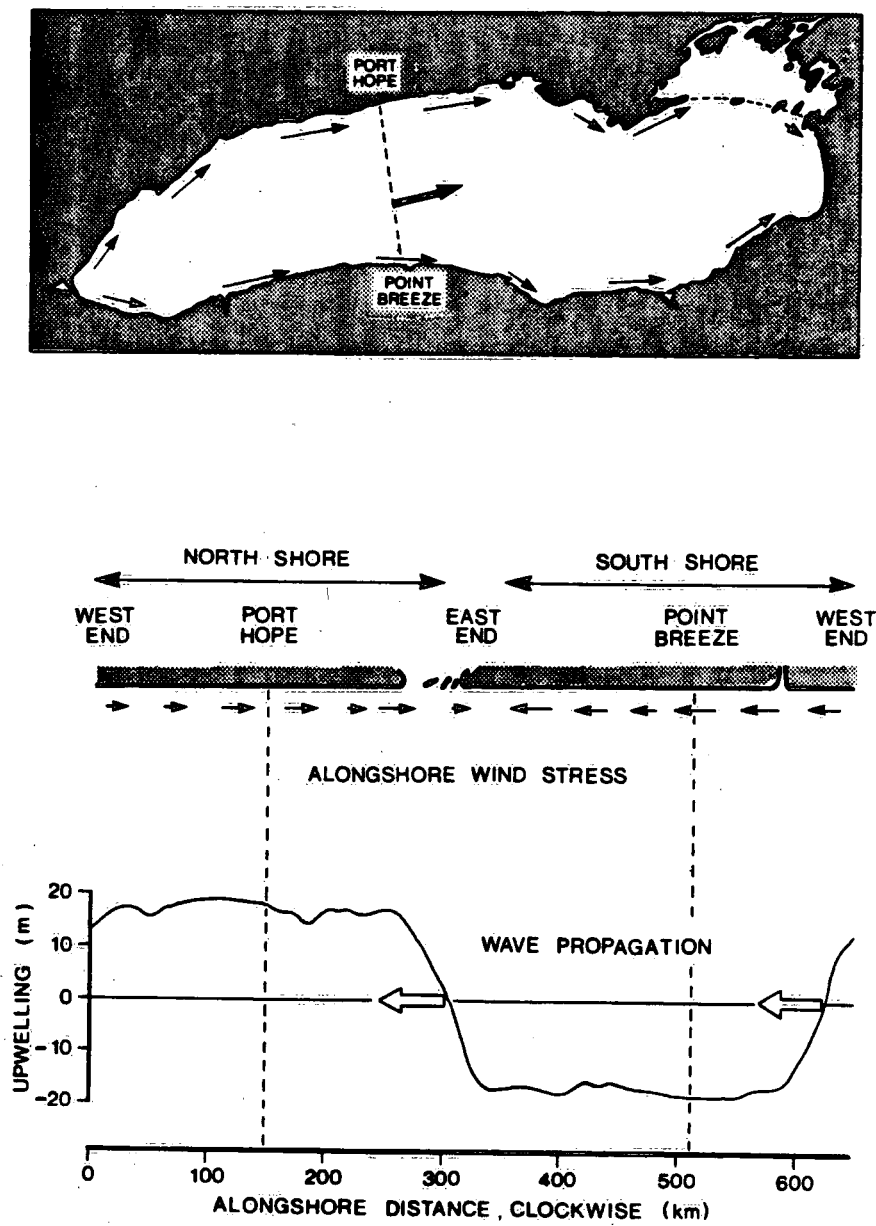


Fig. 3.7 Alongshore component of wind stress during storm of August 9-11, 1982 and resulting thermocline excursions computed from a simple upwelling model.

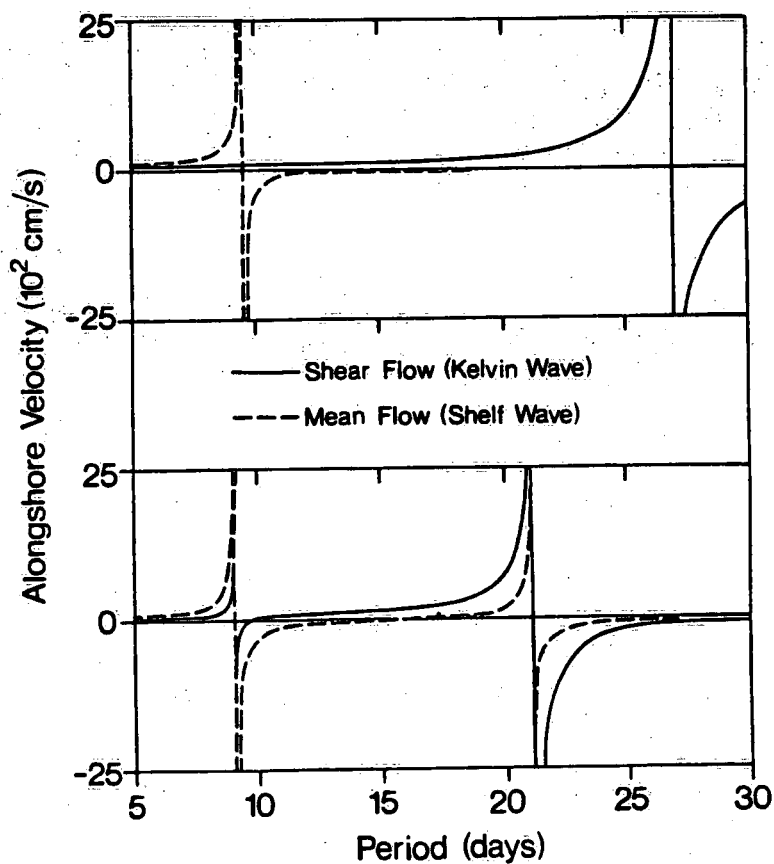


Fig. 3.8 Inviscid response of two-layer channel model to progressive alongshore wind wave, 5 km off Port Hope. Alongshore wavelength 600 km, thermocline depth 12 m, shore depth 14 m, density difference  $1.5 \times 10^{-3}$ . Above: uncoupled mean and shear flow; below: coupled mean and shear flow.

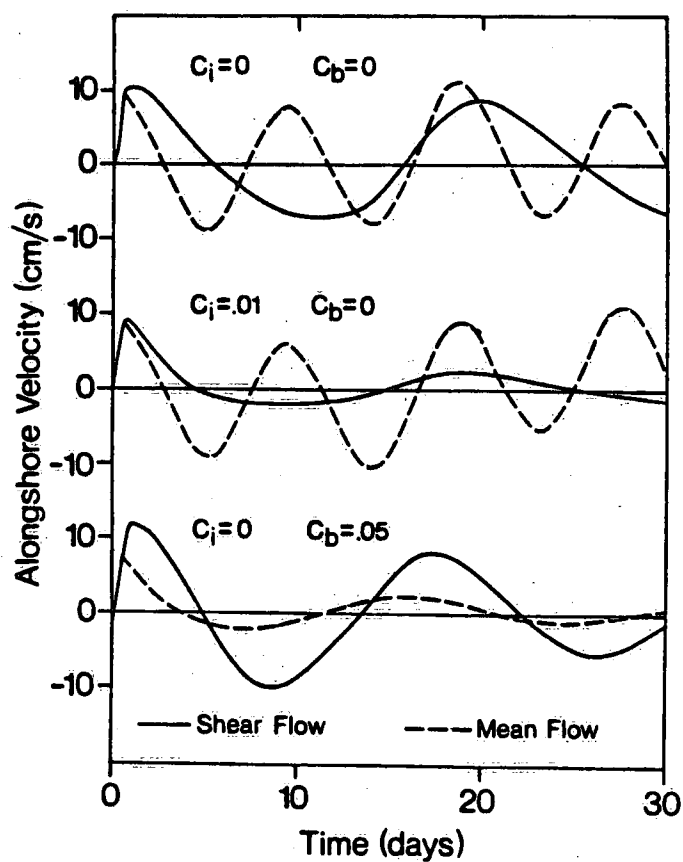


Fig. 3.9 Response of two-layer channel model to wind impulse of 16 h duration with alongshore shape of a standing wave. Model parameters as in Figure 3.8, coupled mean and shear flow. Above: no friction; middle: internal friction with coefficient  $c_i=0.1$  cm/s; below: bottom friction with coefficient  $c_b=0.05$  cm/s.



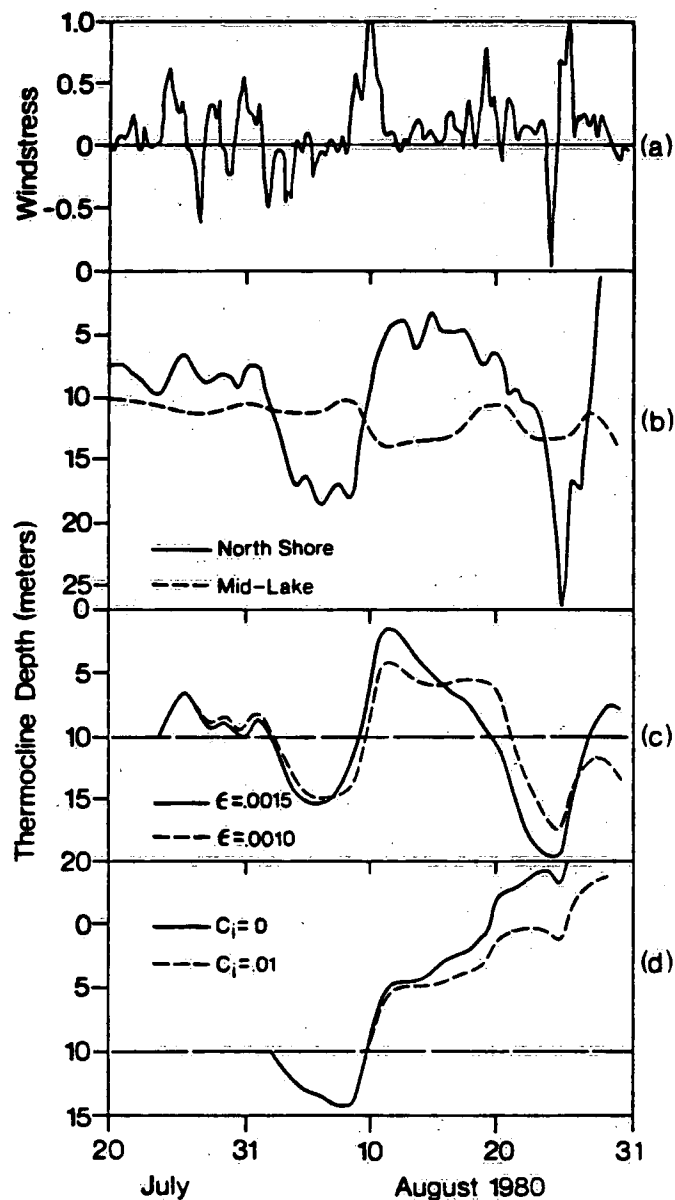
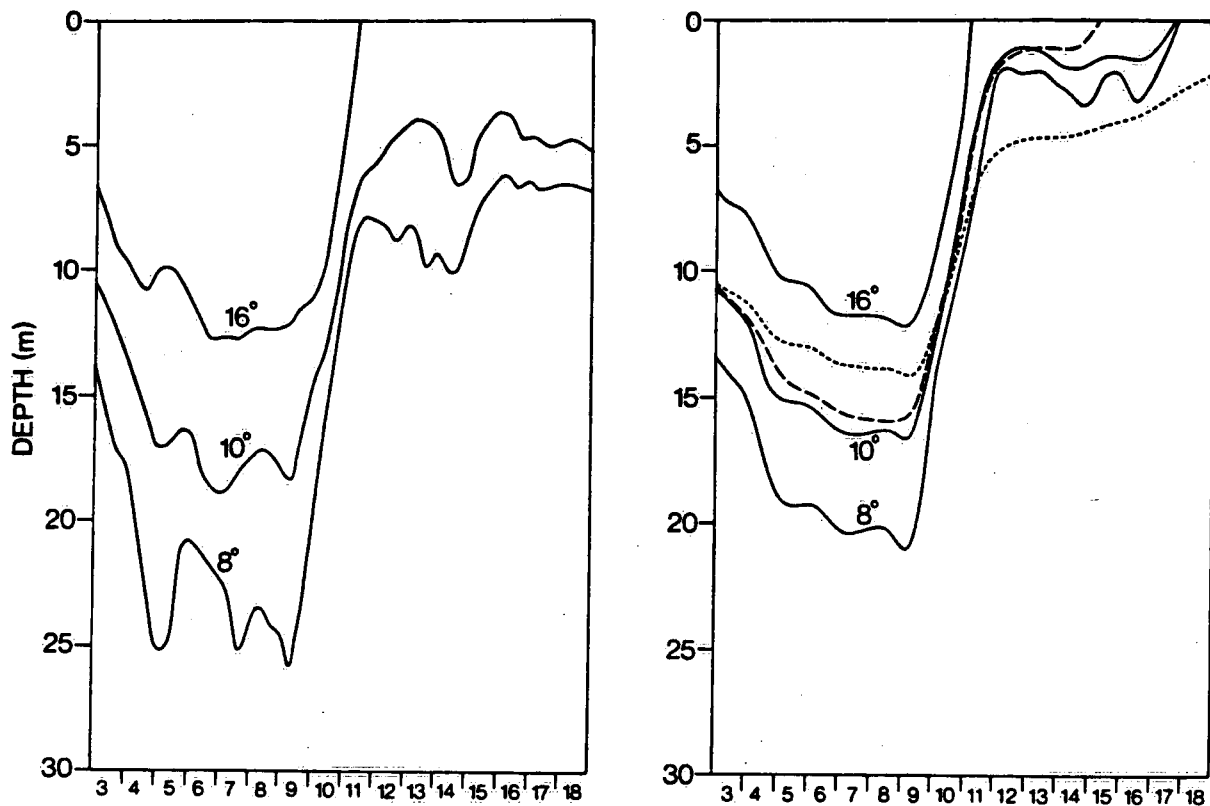


Fig. 3.10 (a) Eastward component of wind stress observed on Lake Ontario.

(b) Observed 10° isotherm depths, 5 km from northshore and at mid-lake station.

(c) Thermocline depth computed by two-layer model of Figure 3.9 without friction, for two values of the density gradient.

(d) Thermocline depth computed by two-layer infinite channel model with uniform wind and internal friction given by coefficient  $c_i$  (cm/s).



AUGUST 1982

Fig. 3.11 Left: observed temperature variations 5 km off Port Hope.  
Right: temperature variations computed 5 km offshore with an infinite channel model with horizontal gridmesh of 0.5 km and vertical grid spacing of 1.5 m (solid lines) and thermocline depth computed by a 2-layer model 3 km offshore (long dashes) and 5 km offshore (short dashes).

## Winter Study: North-South Transect

### 4.1 Current Measurements

The present analysis is concerned with a cross-lake array of current meters (Fig. 1.2, Table 1.2). Currents were decomposed into alongshore and onshore components with the alongshore direction defined to be  $80^\circ$  from north. Our primary concern is with the alongshore current and the distribution of this flow throughout the cross section. All time series were smoothed by a digital low-pass filter. The filter is designed to eliminate fluctuations shorter than one day without affecting current variations with periods longer than one day. This eliminates all effects of free surface seiches and any wave-induced noise in the current meter records.

For many practical considerations it is important to determine long-term mean water movements in a lake. The cross-lake distribution of the alongshore current averaged over the entire period from 4 November 1982 to 23 March 1983 are presented in Figure 4.1. Positive contour values indicate eastward currents, negative values represent westward currents. The currents show remarkable consistency in the vertical, as should be expected under homogeneous conditions. Most striking is the strong eastward current along the south shore with compensating return flow in deep water. This seasonal-mean circulation will be discussed in more detail in the next section.

Alongshore current variations in time and space are illustrated in Figure 4.2. The first record shows the current 12 m below the surface at a distance of 5 km from the north shore, with a sounding depth of 28 m. The current is characterized by large-amplitude oscillations with periods of 5-10 days. It will be analyzed in the following Chapter as part of the data from the alongshore current meter array. In essence, the current fluctuations are caused by local wind impulses, with secondary effects of wind-induced topographic waves propagating around the perimeter of the lake in a counterclockwise direction.

The three records in the centre of Figure 4.2 represent currents in the deepest part of the cross section at 12 m and 50 m below the surface and 1 m above the bottom. They show that the current is essentially uniform in the vertical and generally runs against the direction of the coastal current. This deep return current is primarily driven by pressure gradients associated with the slope of the free surface against the wind (Bennett, 1974). In addition, deep currents exhibit low-frequency oscillations due to topographic vorticity modes of rotating basins (see e.g., Saylor et al, 1980).

Finally, the last current record of Figure 4.2 shows the near-surface current at a distance of 3 km from the south shore with a water depth of 29 m. The fluctuating component of the current is very similar to that observed at the north shore, both in amplitude and in

phase. However, the long-term mean component is quite different, with a pronounced eastward net flow raising the overall level of the south shore current record. A similar contrast between the south shore and north-shore currents clearly emerged from the extensive coastal observations during the stratified season of 1972 (IFYGL) and also was suggested by the more limited winter data of 1972/73. The dynamics of this phenomenon in presence of stratification have been presented in the IFYGL literature (see Saylor et al., 1981, for a review). The properties of this circulation during the homogeneous season will be presented in the following pages.

#### 4.2 Transport Calculations

The spatial resolution of the above current measurements should be adequate to compute an accurate distribution of water transport through the cross section. The first step is to obtain vertically integrated currents or transports per unit width for each vertical string of current meters. Since the currents are quite uniform in the vertical, as illustrated by the example of Figure 4.2, a simple linear interpolation should be acceptable. Thus, for strings of three current meters, the integrated current,  $U$ , is obtained as follows:

$$U = 50 \frac{u_1 + u_2}{2} + (h - 50) \frac{u_2 + u_3}{2}$$

where  $u_1$ ,  $u_2$  and  $u_3$  are the currents at depths of 12 m and 50 m below the surface and 1 m above the bottom, and  $h$  is the local water depth in meters.

For moorings with observations at two depths, the formula used is

$$U = h \frac{u_1 + u_2}{2}$$

where  $u_1$  and  $u_2$  are the currents at 12 m and the bottom. The latter approximation is also used for moorings with observations at a single depth. In that case the missing current is estimated as follows. First, the ratio of standard deviations between surface (12 m) and bottom currents is obtained for stations where both measurements are available. For moorings in water shallower than 100 m the values range from 1.2 to 1.4. Thus, the missing surface records in stations C10 and C11 are obtained by adding one third to the bottom current, and the missing bottom current for station C1 is estimated by subtracting one quarter from the surface current.

The vertically averaged current is equal to the vertically integrated current divided by the local water depth. The long-term mean values of the vertically averaged currents for each string of current meters are presented by black circles connected by solid lines in the left hand panel of Figure 4.3. Positive values represent

eastward flow. The standard deviations of the fluctuations around the long-term means are denoted by triangles connected by broken curves in the same drawing. The current fluctuations are large in both coastal zones and decrease with offshore distance much more rapidly near the steep south shore than over the gently sloping bottom of the north shore.

The long-term mean values and standard deviations of the vertically-integrated currents or transports per unit width are presented in the right hand panel of Figure 4.3. Integration of the area under the mean transport curve gives a total eastward water transport of  $70 \times 10^3 \text{ m}^3/\text{s}$  and a total westward transport of  $66 \times 10^3 \text{ m}^3/\text{s}$ , the net transport being  $4 \times 10^3 \text{ m}^3/\text{s}$  to the east. This may be compared with the hydraulic flow associated with the Niagara inflow and St. Lawrence outflow, which is approximately  $7 \times 10^3 \text{ m}^3/\text{s}$  as illustrated by the shaded rectangle in Figure 4.3. Expressed in terms of the one-way transport, the error is about 4%. This small error in the total water balance, together with the horizontal and vertical consistency of the current observations shown in Figures 4.1 and 4.2, lend considerable credence to the data.

The cross-lake distribution of water transport divides the lake into three zones. In the northern part, the mean transport tends to vanish but the fluctuating component of the transport is very large. This is consistent with concurrent wind observations which show large day-to-day variations in speed and direction but a nearly

vanishing net forcing when averaged over the entire period of measurement. The southern part of the section, on the other hand, shows a strong eastward mean transport which is apparently compensated by return flow in the central part of the basin. Here, the standard deviations reach a maximum at the line separating the belts of mean eastward and mean westward transport. This suggests a north-south meandering of the eastward and westward flow maxima at this point in contrast to the northern border of the return flow, which appears quite stable with low standard deviations of fluctuating transport components.

At first glance, the cross-lake distribution of the seasonal-mean water transport (solid lines of Figure 4.3) seems to reflect the results of analytical and numerical model studies (see Simons, 1980, for a review). Upon closer inspection, however, significant discrepancies become apparent. If the seasonal-mean circulation is visualized as the quasi-steady response of the lake to the mean wind, the corresponding model solutions display narrow wind-driven boundary currents along both shores, with adjacent bands of return flow and cross-wind drift in the interior. In this particular cross section of Lake Ontario, typical numerical solutions for the mean wind stress during the period of observation ( $1.1 \times 10^{-2} \text{ Nm}^{-2}$  to the east) are dominated by a relatively large clockwise circulation cell near the north shore, while the counterclockwise cell along the south shore is quite weak and only a few km wide. In contrast to



these solutions, the observations show negligible net transport near the north shore, the return flow is concentrated in the central part of the cross section and the band of south-shore flow extends to the point of maximum depth (see Figure 4.1). Thus, the strong eastward flow along the south shore is not a narrow boundary current but, together with the return flow, forms a counterclockwise circulation cell centered in mid-lake. In the remainder of this chapter, these observations will be compared with the results of circulation models, and it will be shown that the seasonal-mean flow is due to nonlinear interactions of topographic waves.

As noted above, the one-way transport averaged over the period of observation is ten times as large as the hydraulic flow. If it is assumed that the eastward flowing Niagara River water is mixed throughout the belt of eastward transport, then it follows that 90% of this inflow must be recirculated, since only 10% of the total eastward transport can leave through the St. Lawrence River. With a mean speed of 5 km/day in the belt of eastward transport and a length of the lake less than 300 km, the time scale of the recirculation is a few months. In reality, the recirculation must be expected to be greater than 90%, since the Niagara River water will not be confined to the belt of easterly transport.

To conclude this discussion of the current meter data, cross-lake distributions of vertically integrated currents as a function of time for the entire period of observation, 4 November 1982

to 23 March 1983, are shown in Figure 4.4. Solid lines denote reversals from eastward to westward transport and vice versa. Vertical shading represents eastward transport greater than  $10 \text{ m}^2/\text{s}$ , horizontal shading represents westward transport greater than  $10 \text{ m}^2/\text{s}$ . The meandering of the transport maxima in the southern part of the basin is quite noticeable.

It is of interest to illustrate the correlation between these observed circulation features and the distribution of toxic contaminants such as mercury and mirex in the sediments of Lake Ontario. Figures 4.5 and 4.6 show examples of such distributions reproduced from Thomas (1983). The dominating effect of the year-round boundary current along the south shore is evident. In particular, the mercury distribution, however, exhibits clear indications of westward displacements of the Niagara River plume. Also, the recirculation of up to 90 percent of the water masses at the eastern end of the lake, as inferred from the foregoing transport calculations, is quite apparent in the sediment distributions.

#### 4.3 Dynamics of Large Lake Circulations

Hydrodynamic models appear to have been generally accepted as useful tools to elucidate the dynamics of ocean circulations and to simulate short-term local current patterns as well as climatological mass transports in the world's oceans. Unlike their meteorological

counterparts which have been constantly improved by recourse to routine observations from a dense network of weather stations, oceanic circulation models cannot be adequately verified with the available data base and their acceptance is based more on faith than fact. There is no indication that this faith has been shaken by the conclusions of systematic verification studies of hydrodynamic models of the Great Lakes, which raise serious doubts about the ability of such models to simulate long-term circulation patterns (Simons, 1976; Allender, 1977; Bennett, 1977; Schwab, 1983). Perhaps it is felt that the disparity of oceanic and limnological scales or differences in dynamical processes render a comparison of circulation models of lakes and oceans invalid.

The dynamics of lakes and oceans may be contrasted by recourse to the vorticity balance for the vertically integrated mass transport or, more specifically, the vorticity equation for the vertically averaged transport

$$\frac{\partial \zeta}{\partial t} + J\left(\psi, \frac{\zeta}{H}\right) = J\left(\frac{f}{H}, \psi\right) - \nabla \cdot \left(\frac{B}{H} \nabla \psi\right) + \text{curl} \left(\frac{\tau_s}{H}\right) \quad (1)$$

where  $\zeta = \nabla \cdot (H^{-1} \nabla \psi)$ ,  $t$  is time,  $\psi$  the mass transport stream function,  $H$  the depth,  $f$  the Coriolis parameter,  $\nabla$  the horizontal gradient operator,  $J$  the Jacobian,  $\tau_s$  the wind stress,  $B$  a depth-dependent bottom stress coefficient, and effects of baroclinic pressure and surface waves have been ignored. The first term on the right

GB 707

C335 no.

171E

represents planetary and topographic vorticity tendencies. While the beta-effect is generally predominant in the oceans, the Coriolis parameter may be treated as a constant in lake models with the result that the topographic effect takes over. Thus, the planetary Rossby waves of ocean models are replaced by topographic normal modes in lake models. The last term on the right is similarly affected by the spatial scales of oceans and lakes. While large-scale ocean circulations are governed by the curl of the wind, the dimensions of lakes are small compared to typical weather systems and hence the wind stress is in first approximation uniform. As pointed out in studies of the North Sea (Groen and Groves, 1962), shelf waves (Gill and Schumann, 1974), and lakes (Bennett, 1974), such smaller-scale circulations are generated by depth gradients normal to the wind. Finally, the bottom stress coefficient as determined from Ekman theory is proportional to the inverse of the depth in deep water but tends to become inversely proportional to the square of the depth in shallow water (Simons, 1983; Schwab, 1983).

There may also be some doubt whether, in spite of the extensive data base used in circulation studies of the Great Lakes, the spatial resolution of the measurements has been adequate for model verification. The common procedure in these studies has been to more or less cover the basin with a network of current meters and to compare observations with model results in adjacent grid points. It is clearly preferable to design a measurement array which permits

unambiguous interpolation between instruments such that mass conservation requirements are satisfied. Thus, the high-resolution array of instruments in the cross section of Lake Ontario during the winter of 1982/1983 is most suitable for evaluating the performance of typical lake circulation models and, by extension, obtaining an indication of the reliability of similar ocean models.

The simulation capability of a circulation model will likely depend on the time scales under consideration and on the relative importance of various dynamical processes in a given situation. Indeed, results of past experiments show that the immediate response of a lake to a strong wind impulse is more readily simulated than long-term circulations dominated by frictional effects or stratification (Simons, 1980). In view of this, the following analysis considers short-term and long-term circulations separately.

#### 4.4 Numerical Models

Choosing the most suitable model for studies of this kind is not a straightforward matter. There is a choice of free surface or rigid lid models, vertically integrated or multi-level formulations, various finite-difference lattices or some other spatial discretization. The present study is not directed at a comparison of different modeling techniques. Instead, the primary intent is to see if conventional and representative hydrodynamic models are capable of

simulating the main characteristics of observed circulation patterns. For a homogeneous basin, the most direct approach is to solve the vertically integrated equations of motion and the continuity equation on a single Richardson lattice or, if divergence effects are suppressed by the rigid lid approximation, to solve the vorticity equation (1) on a rectangular grid.

The rigid lid approximation rests on the assumption that the characteristic length scales are smaller than the ratio of the surface wave speed to the Coriolis parameter. With a typical depth of 100 m and a basin width well below 100 km, topographic circulations in Lake Ontario are unlikely to be affected by free surface effects, and hence the vorticity equation should give the same solutions as the shallow water equations. However, allowance must be made for numerical truncation errors caused by imperfect resolution of finite difference schemes. Since such errors may be quite different for the rigid lid and free surface models, it appears worthwhile to use both of them for the present simulations. Also, effects of model resolution will be explored in the next section before proceeding to the actual model calculations for Lake Ontario.

The vertically integrated free surface equations for homogeneous water are

$$\frac{\partial U}{\partial t} = -gH \frac{\partial h}{\partial x} + fV - BU + \frac{\tau_{sx}}{\rho} - \frac{\partial}{\partial x} (U\bar{U}) - \frac{\partial}{\partial y} (V\bar{U}) \quad (2)$$

$$\frac{\partial v}{\partial t} = -gH \frac{\partial h}{\partial y} - fU - BV + \frac{\tau_{sy}}{\rho} - \frac{\partial}{\partial x} (Uv) - \frac{\partial}{\partial y} (Vv) \quad (3)$$

$$\frac{\partial h}{\partial t} = - \frac{\partial U}{\partial x} - \frac{\partial V}{\partial y} \quad (4)$$

where  $U$ ,  $V$  are the components of the vertically integrated transport vector in  $x$ ,  $y$  direction, and  $\bar{u}$ ,  $\bar{v}$  the corresponding vertically averaged currents,  $h$  is the free surface displacement,  $g$  is gravity,  $\rho$  is density and the notation is otherwise the same as in equation (1). Based on model studies of the Great Lakes (Simons, 1983; Schwab, 1983) the best estimate of the bottom stress coefficient is  $B = 5 \times 10^{-3} H^{-2}$  where  $H$  is expressed in meters and  $B$  has dimensions of  $s^{-1}$ . The corresponding frictional time scale varies from one day for depths of 20 m to 100 days for depths of 200 m, a typical overall value for Lake Ontario being 10 days.

On a single Richardson lattice, the model variables are staggered in space, with the surface elevation being defined at the centre of a grid square and the normal components of the transport vector on the sides of the square. Spatial derivatives are approximated by central differences and the Coriolis term is obtained by averaging over four surrounding points. In order to preserve total kinetic energy in the averaging process, the Coriolis terms in (2) and (3) are multiplied by  $(1 + H_u/H_v)/2$  and  $(1 + H_v/H_u)/2$ , respectively, where  $H_u$  and  $H_v$  are the depths in  $u$ - and  $v$ -points,



respectively. The nonlinear terms are approximated by the energy-consuming momentum formulation for a single Richardson lattice (Lilly, 1965). Time extrapolation is carried out by applying a single-step forward scheme to each variable in turn, thereby using the most recent values of the two other variables. Due to the structure of the equations, this procedure is equivalent to a forward-backward scheme for the Coriolis terms and a leapfrog scheme for the pressure-divergence terms, with the time step being determined by the CFL condition (Courant et al. 1928). The present Lake Ontario model employs a mesh size of 5 km and a time step of 75 s. The time step for the nonlinear terms depends on the speed of the current rather than on the free surface wave, and hence these terms are recomputed at intervals of 1/2 hour. For a discussion of these numerical procedures, reference is made to Simons (1980).

The solution of the vorticity equation also employs a single-step scheme for time extrapolation and central differences for spatial derivatives. The Coriolis term is averaged over the old and new time step and hence appears on the left as well as the right hand side of the finite difference equation. The frictional term is evaluated forward in time, which sets an upper bound on the time step in shallow water. The grid spacing used for the Lake Ontario calculations was 2.5 km, and the time step was one hour for the linearized model and 1/4 hour if the nonlinear terms were included. Solutions were obtained by relaxation with an overrelaxation factor of 1.5. In

order to achieve convergence of long-term mean solutions, it was found necessary to continue the iteration process until the difference between successive iterations was everywhere smaller than  $1 \text{ m}^3 \text{ s}^{-1}$ , while typical instantaneous values of the stream function were of order  $10^5 \text{ m}^3 \text{ s}^{-1}$ . The number of required iterations is considerably reduced if the first guess is obtained by linear extrapolation from the last two time steps.

#### 4.5 Model Resolution

Since wind-driven circulations in homogeneous lakes are dominated by topography, the required resolution of a numerical model is essentially determined by the maximum depth gradients encountered in the basin. In Lake Ontario (Fig.1.1) the southshore bottom slope is twice as steep as the northshore slope and hence numerical truncation errors may be anticipated to be most severe along the southern shore. A straightforward method of evaluating such truncation errors is to increase the model resolution until the solution converges. It is not practical to apply this procedure to the actual lake, since studies of topographic waves suggest that the grid spacing should be less than 1 km, which translates into  $10^4 - 10^5$  grid points for the whole lake. As an alternative, the procedure was applied to an idealized basin with topographic features similar to Lake Ontario.

An idealized basin which has received a great deal of attention in theoretical studies is the circular basin with parabolic depth profile. Analytical solutions are available for the inviscid, time-dependent response to a wind impulse (Birchfield and Hickie, 1977) as well as steady state circulations (Birchfield, 1967, 1973). The first step of the present resolution experiments was to extend these solutions to include bottom friction in time-dependent problems and to allow for more realistic depth variations. This was done by applying the method of separation of variables to reduce the two-dimensional problem to a one-dimensional problem which can be solved numerically with sufficient resolution to assure that the solutions are exact. The second step was to solve the same problem on a two-dimensional rectangular grid with lower resolution and to compare the results with the exact solutions.

The one-dimensional problem is formulated by assuming that the depth of the circular basin is a function of radius only and by writing the dynamical equations (1) - (4) in polar coordinates and discarding the nonlinear terms. For a uniform wind, the wind stress components in these equations are proportional to the sine and cosine of the azimuthal angle, and hence the solutions must be of the same form. Substituting such solutions leads to equations in which the radius of the basin appears as the only spatial variable. The corresponding finite-difference equations were formulated for the free surface as well as the rigid lid model. In this case, the vorticity equation can be solved conveniently by direct matrix inversion.

When applied to problems of inviscid circulation in circular basins with parabolic depth profile, both one-dimensional numerical models were found to converge to the available analytical solutions. The parabolic depth was then replaced by the steep southern slope of the depth profile of Lake Ontario shown in Figure 1.2. Since the width of this slope region is about 20 km, an interior region of constant depth was added such that the diameter of the circular basin was comparable to the width of the cross section of Figure 1.2. With bottom friction included, both numerical models were run with increasing resolution until their solutions converged. These results will be referred to as the exact solutions. As expected, the models required a grid spacing less than 1 km to reduce the errors to a few percent of the currents. This grid interval represents a few percent of the width of the bottom slope region.

Two examples of the resolution experiments will be presented here because they have a direct bearing on the following discussion of Lake Ontario calculations. The first one concerns the response to a wind impulse of finite duration, the second one is the long-term averaged current induced by actual winds observed during the 1982/1983 Lake Ontario experiment. In each case the model solution of interest is the current in the diameter perpendicular to the wind.

Figure 4.7 presents the impulse response as a function of offshore distance and depth. The solid lines represent the exact solutions obtained from the high-resolution one-dimensional models.

The dashed curves show results from a free surface model with a two-dimensional rectangular grid with resolution of 5 km. The dotted lines present results from a two-dimensional rigid lid model with the same grid spacing. For this particular problem, the 5 km resolution appears acceptable for the free surface model but not for the rigid lid version. If the grid spacing of the latter is reduced by one half, the accuracy becomes comparable to that of the former.

Figure 4.8 compares long-term results obtained by forcing the circular basin with winds observed on Lake Ontario during the 140-day period from 4 November 1982 to 23 March 1983. The solutions on the left were averaged over the first 70 days, the results on the right are averages for the whole period. Since the mean wind over the second half of the experiment is opposite to that of the first half, the net wind and, hence, the net circulation is very small. The heavy solid lines present the exact solutions. The squares represent the free surface model with a two-dimensional grid of 5 km; the circles show results from the two-dimensional vorticity model with a grid of 2.5 km. For the low bottom friction used in the present studies, the free surface model tends to overestimate topographic current oscillations in deep water. This leads to serious errors when solutions are averaged over long periods of time, especially if the mean forcing tends to vanish.

Like the analytical solutions for the circular basin, the foregoing numerical results were obtained from linear models. The

separable solutions of the linearized problem were also used to compute second-order corrections, as done by Bennett (1978) for a stratified circular basin. The first azimuthal wave which is forced by the uniform wind generates a circular vortex of zero wavenumber as well as the second azimuthal wavenumber. For the present case, the circular vortex appears as a mean cyclonic circulation in the interior of the basin, as shown by the thin solid line in Figure 4.8. The reason is that topographic alongshore transport of the type shown in Figure 4.8 is typically associated with Ekman-type transport toward the bottom of the page (Birchfield, 1973; Birchfield and Hickie, 1977). The resulting onshore advection of alongshore momentum generates cyclonic flow in the interior and anticyclonic flow closer to shore. However, the nearshore effect tends to be reversed in the diameter along the wind, and hence it is part of the second azimuthal wavenumber. It is noted that, although Bennett's (1978) paper was primarily concerned with internal Kelvin waves, some of the illustrations in that paper show a cyclonic vortex in the interior of the basin which the author explains as the rectified effect of forced topographic waves.

The nonlinear problem may also be formulated as an energy-conserving low-order spectral model as often done in atmospheric studies (e.g. Simons, 1972). In addition to the nonlinear self-interactions of the forced wave, such models include interactions between the circular vortex and the waves and between waves of

different wavenumbers. Calculations of that kind were made for the present case. A detailed discussion of the results is beyond the scope of the present paper but it is of interest to mention that nonlinear changes of the first azimuthal wave were found to be comparable in magnitude to the truncation errors in the low-resolution simulations shown in Figure 4.8.

#### 4.6 Short-Term Current Fluctuations

The short-term model performance is, in this study, evaluated by comparing the response of the model and the real lake, respectively, to a finite wind impulse. Impulse response functions are familiar from storm surge prediction (Schwab, 1978) and will also be used for computing wind-driven coastal currents in the following Chapter. For the hydrodynamic model, the response characteristics are determined by forcing the linearized model with a unit wind impulse and recording the time variations of computed currents in grid points of interest. For the lake itself, empirical response functions can be obtained from observed current series provided that simultaneous wind records are available.

The impulse response method becomes particularly simple if the basin is of small extent compared to typical weather systems such that the wind field may be assumed to be uniform over the whole lake. In that case the current,  $u$ , at a particular location can be written as

$$u(t) = \int_0^T \tau(t - t') \cdot R(t') dt' \quad (5)$$

where  $\tau$  is the wind stress history,  $R$  the impulse response function for the location of interest and  $T$  represents the finite memory of the lake due to friction. In terms of observations at discrete time intervals,  $\Delta t$ , and memory  $N = T/\Delta t$ , equation (5) becomes

$$U_i = \sum_{n=1}^N \tau_{i-n} \cdot R_n \quad (6)$$

Given a wind and current record, equation (6) generates a system of equations which can be solved for the unknown impulse response. In order to obtain reliable results, the length of the data series must be much greater than the length of the response function and the system must be solved by a least squares algorithm. After some experimentation, a suitable time step was found to be 12 hours, with winds and currents being staggered in time. To utilize the complete current records, the wind record was extended backward in time.

Winds are available from routine weather observations at Toronto Island Airport, slightly west of Station A7. During the first 80 days of the experiment winds were also measured by a meteorological buoy at Station C7 and by shore-based wind recorders at both ends of



the cross-lake array. The wind records from the buoy were frequently interrupted by icing problems and hence are not very useful. Frequency spectra of wind records from the two shore stations have the same shape as the Toronto Island wind spectrum, but the amplitudes are reduced by height differences and, perhaps, some sheltering effects. As shown in Chapter 2, the summer measurements taken by a similar wind recorder on the beach near the Toronto Island weather station showed a uniform reduction of the wind spectrum for periods longer than a few days. If this result is used to adjust the present shore-based measurements, the wind at the southshore station becomes almost identical in speed and direction to that on Toronto Island when averaged over the common period of operation. At the northshore station the mean wind speed is 15% lower and the direction is turned 40 degrees counterclockwise.

Since the Toronto Island wind record is continuous and appears to be quite representative of wind conditions over the lake, it is used for the present calculations. The wind is taken to be uniform but the possible effects of a long-term windshear as observed between the two shore-based wind recorders will be evaluated. The wind stress is obtained from the square of the windspeed with a drag coefficient ranging from  $1.5 \times 10^{-3}$  for windspeeds less than  $10 \text{ m s}^{-1}$  to  $3.0 \times 10^{-3}$  for speeds over  $20 \text{ m s}^{-1}$  with a linear variation in between. These relatively high values are suggested by earlier model studies of the Great Lakes (Simons, 1975; Schwab, 1978) and, again in

this study, appear necessary to reproduce observed short-term current variations.

The model verification is concerned primarily with water transports through the cross section, i.e., with alongshore currents, since these measurements can be checked for mass conservation. While the water transports through a north-south cross-section of the lake are most likely dominated by the east-west component of the wind, effects of the north-south component cannot be ruled out. Thus, the empirical modeling procedure included both components of the wind. The response to the wind component normal to the cross section shows good convergence for different truncation of the response function between 10 and 30 days, but the response to the second wind component does not. Therefore, the short-term model verification is confined to the response of alongshore currents to alongshore winds.

Computation of empirical response functions may be adversely affected by the low-frequency portions of the wind and current spectra. To avoid this problem, long-term oscillations were eliminated by a high-pass digital filter. The separation of time scales is somewhat arbitrary but, clearly, the cut-off period should be longer than the memory of the lake as estimated from the impulse response functions. In this study, long-term current variations are taken to have time scales of one month or longer. The high-pass filter fully preserves fluctuations with periods shorter than 35 days and completely eliminates currents with periods longer than 46 days.

Results of computations are presented in Figure 4.9. The solid lines show the empirical current response to a 12-hour wind impulse for all current meter moorings of the cross-lake array of Figure 1.2. The sounding depth is shown for each station, and the results are ordered from shallow to deep water on both the northern and southern half of the section to illuminate the asymmetry of the response. The broken curves show impulse response functions computed by a 5-km free surface model in corresponding grid points or, for a few stations, in the middle of two adjacent grid points. The correspondence between empirical and computed response is best near the northern shore and in deep water and is particularly poor for stations with depths approaching the mean for the cross section (100 m).

As noted in the Introduction, the present measurement program was designed to permit unambiguous interpolation between instrument positions and verification of mass balance conditions for water transports through the cross section of the lake. An objective computer algorithm was used for horizontal interpolation of the vertically integrated mass transports computed for each station, as outlined above. Boundary conditions are zero transport at the shores. The empirical cross-lake distributions of transports generated by a 12-hour wind impulse are presented in the left-hand panel of Figure 4.10. Corresponding results from the 5-km free surface model are shown in the right-hand panel. Good agreement is observed during

the first few days and again after the fifth day or so, but considerable differences occur at intermediate times and, in particular, near the mean depth of the cross section. According to simple models of wind-driven lake circulation (Bennett, 1974), the mean depth contour tends to separate downwind coastal currents from mid-lake return flow. This effect is quite evident in the initial response of the present model as well as the empirical results.

The main advantage of the data presentation in the form of Figure 4.10 is that it permits a check of the internal consistency of the current meter observations and the empirically determined response functions. To that end, the mass transports on the left of Figure 4.10 are integrated over eastward and westward current regimes separately and compared in the upper part of Figure 4.11. The remarkably close balance lends credence to the model verification procedure adopted in this study. Corresponding mass transports obtained from the model are shown in the lower part of Figure 4.11, again based on the interpolated results presented on the right of Figure 4.10. In this case the source of the imbalance in the total mass transport can be readily identified. It turns out that approximately one-half of the net westward transport after one day is associated with free surface displacements and the other half is due to interpolation. The interpolation tends to underestimate nearshore transports which, at this time, are directed toward the east, as seen in Figure 4.10.

#### 4.7 Long-Term Circulations

The relatively good performance of the linearized model in simulating the immediate response of the lake to wind is not surprising in view of past experience with lake circulation models (Simons, 1980, 1983; Schwab, 1983). However, as noted in the Introduction, less favorable results may be expected for long-term simulations. This problem will be addressed by using the above-mentioned filter to eliminate current fluctuations with periods shorter than about one month.

The first and last few points of a low-pass series cannot be unambiguously determined. If the digital filter is applied to the total length of the record, the original series must be artificially extended on both sides. Since the original data records have relatively large long-term means and trends, reflection of the series at both ends is probably the best approach. This method was compared with extension with zeros and the differences between the resulting low-pass series were found to be essentially confined to the first and last 10 days. Therefore, in order to avoid ambiguity, the low-pass series were truncated at these points. Figure 4.12 presents the low-pass time series of observed wind stress and current. The days refer to the 140-day period of measurement starting 4 November 1982 and ending 23 March 1983.

Inspection of the left-hand side of Figure 4.12 shows that long-term current variations near the northern shore tend to be correlated with the alongshore wind component. The long-term trend of the southshore current (right-hand side of Figure 4.12) is somewhat similar, but this current is dominated by a strong mean component toward the east. The deep currents run generally against the wind but their variations in time do not show a strong correlation with the wind. Again, a better illustration of these observations is provided by horizontal interpolation of vertically integrated transports. The resulting variations for time scales of one month or longer are presented in Figure 4.12. The most striking feature of the cross-lake distribution of transport is the belt of strong eastward currents extending from the southshore to well beyond the mean depth contour. In contrast to the northshore currents, the southshore current and the deep lake return flow show no clear correlation with wind variations.

The long-term model calculations utilized hourly values of observed winds starting one month before the onset of the field experiment. The model results were then low-pass filtered in the same way as the observed records. Computations were made first with a linear free surface model with a resolution of 5 km and a linear rigid lid model with grid spacings of 5 km and 2.5 km. None of the model results compare with observations except in the shallow water near the northshore. The general features of all model solutions are alike. Particularly similar are the results from the 5-km free surface model

and the 2.5-km rigid lid model. As an example, Figure 4.14 shows results from the linear free surface model with the friction formula presented under equation (4). In contrast to the broad belts of observed currents (Figure 4.13), the computed circulations are characterized by small-scale features. To ensure that the results were not adversely affected by the start-up procedure or by long-term error accumulation, the model was restarted three months earlier. The results were identical.

Since the computed small-scale circulations are concentrated in deep water, they may be partly suppressed if the shallow-water friction formulation given under equation (4) is replaced by the conventional deep-water Ekman friction which is inversely proportional to  $H$  rather than  $H^2$ . Thus the model was rerun with a friction coefficient  $B = 1.5 \times 10^{-4}/H$ , which is greater than the shallow water formula for depths greater than 35 m. The resulting currents were too fast in the shore zones and the overall circulation patterns remained the same.

Small-scale circulation features can be readily eliminated by some form of horizontal diffusion of momentum. This was done by adding a Laplacian of the transport to the linearized forms of equations (2-3) with a coefficient equal to  $25 \text{ m}^2 \text{ s}^{-1}$  for the 5-km grid and  $5 \text{ m}^2 \text{ s}^{-1}$  for the 2.5-km grid. The corresponding diffusive time scale is about 10 days. This removes all small-scale circulations from the low-frequency solutions, as shown in

Figure 4.15. The results agree with theoretical studies of quasi-steady circulation (Birchfield, 1967, 1973), but there is still no agreement with the observed circulation except near the northshore.

The long-term results change significantly when nonlinear terms are retained in the models. As expected from the computations for the circular basin (Figure 4.8), the nonlinear solutions display a cyclonic gyre around the point of maximum depth of the cross section. In the absence of diffusion, the nonlinear solutions are still dominated by the small-scale features of the linear solutions. However, if nonlinear terms and horizontal diffusion of momentum are both included, the solutions show a reasonable resemblance to the observations. Figure 4.16 presents results of the nonlinear free surface model with a 5-km grid and a diffusion coefficient of  $25 \text{ m}^2\text{s}^{-1}$ . Again, very similar results are obtained from the nonlinear rigid lid model with a grid spacing of 2.5 km and a diffusion coefficient of  $5 \text{ m}^2\text{s}^{-1}$ .

As mentioned in the Introduction, an important objective of the present study was to verify the internal consistency of the field data by computing total transports through the cross section of the lake. The total eastward and westward transports corresponding to the interpolated observations of Figure 4.13 are presented at the top of Figure 4.17. Ideally, the difference between eastward and westward transports should equal the hydraulic transport associated with the Niagara inflow and the St. Lawrence outflow, which is approximately



$7 \times 10^3 \text{ m}^3 \text{ s}^{-1}$  to the east. The error is seen to be generally of the order of magnitude of the hydraulic flow but not large enough to invalidate the overall circulation patterns displayed in Figure 4.13. For comparison, the total eastward transport computed by the free-surface model with and without horizontal diffusion and with and without nonlinear terms is shown in the lower part of Figure 4.17. In the absence of diffusion and nonlinear terms, the computed transport is remarkably similar to the observed eastward transport, although the cross-lake distribution is completely different. The solution of the nonlinear model with diffusion appears to deteriorate as time goes on.

#### 4.8 Discussion

The foregoing model results are perhaps best illustrated by contrasting observed and computed long-term mean currents and their standard deviations in time. This comparison is presented in Figure 4.18. The heavy solid curve on the left presents the vertically integrated current distribution across the lake averaged over the 140-day period of measurement. The total eastward transport is  $70 \times 10^3 \text{ m}^3 \text{ s}^{-1}$  and the total westward transport is  $66 \times 10^3 \text{ m}^3 \text{ s}^{-1}$ , the net transport being  $4 \times 10^3 \text{ m}^3 \text{ s}^{-1}$  to the east as compared to the actual hydraulic flow of  $7 \times 10^3 \text{ m}^3 \text{ s}^{-1}$ . The dotted curve and the short dashes show results from the linear free surface model with and without diffusion, respectively; the long dashes show results from the

nonlinear free surface model with diffusion; and the thin solid line shows results from the nonlinear rigid lid model with resolution of 2.5 km. The corresponding standard deviations in time are presented on the right. Unlike the long-term mean current, the cross-lake variations of short-term current variations are simulated reasonably well by all models. The observed cross-lake profile of the long-term current appears only in the nonlinear solutions.

As illustrated in Figure 4.8, part of the problem with the long-term solutions is that numerical truncation errors are accentuated when solutions are averaged over long periods of time. Thus, it is likely that small-scale oscillations in the dashed curve of Figure 4.1 are largely spurious and that the long-term averaged solutions of the linear models are best represented by the dotted curve on the left of Figure 4.18. This is essentially the steady-state solution corresponding to the mean wind stress for the period of measurement ( $1.1 \times 10^{-2} \text{ Nm}^{-2}$  to the east) and the low friction used here. As known from theoretical models and numerical calculations for Lake Ontario (see Simons, 1980, for a review), the cross-lake profile of the solution consists of bands of wind-driven currents along both shores, with adjacent bands of return flow and Ekman drift in the interior. In this particular cross-section of Lake Ontario, numerical steady-state solutions for westerly winds are dominated by a large clockwise circulation cell associated with a wide boundary current along the northshore, while the counterclockwise cell along the

southshore is quite weak and only a few km wide. This was verified in the present study by steady-state calculations with high resolution.

The linear solutions are clearly at variance with the present observations, which are dominated by a large cyclonic circulation cell and much stronger mean currents. Although the resolution of typical lake circulation models is apparently too low to obtain accurate results, it is quite unlikely that linear models with higher resolution could reproduce the cross-lake distribution of the seasonal-mean transport. On the other hand, the cross-lake distribution of the long-term trend of observed transport is consistent with the quasi-steady response of the lake to the long-term trend of the wind as computed by linear models. In other words, if the long-term mean flow is subtracted from Figure 4.13, the resulting picture looks much like Figure 4.15 and, conversely, the linear solutions may be corrected by superposing a seasonal-mean cyclonic circulation cell centred at the maximum depth of the cross section. This circulation cell is a rectified effect of forced topographic waves.

It remains to evaluate the assumptions incorporated in the models, since effects of stratification can be ruled out by recourse to the vertical homogeneity of temperature and current measurements, the two assumptions that have to be considered are the uniformity of wind in space and the linear relation between bottom stress and vertically averaged current.

In regard to the spatial distribution of the wind field, it was mentioned in the discussion of the data analysis that the wind recorders at both ends of the measurement array indicated a slight cyclonic curl in the mean wind. To investigate this effect, linear calculations were made for the extreme case of wind increasing linearly from zero on the northshore to the observed value at the southshore. While this was found to give somewhat larger eastward flow along the southshore, the mean circulation was still dominated by the large clockwise cell associated with the northshore boundary current.

The general effect of bottom friction is known. With increasing friction, the steady-state circulation tends to approach that for a long channel with a single broad band of return flow in the center (Simons, 1980, pp. 74-78). As mentioned earlier, the linear calculations were repeated with the shallow water Ekman formulation replaced by that for deep water, which effectively increased effects of bottom friction. Also, calculations were made with a three-fold increase of the original bottom friction coefficient presented under equation (4). The only effect was to increase the width of the boundary currents by a few km. However, all these formulas are linear and imply that the long-term mean bottom stress is only a function of the long-term mean current. In presence of large oscillatory currents, the mean friction might be totally unrelated to the mean flow if a nonlinear stress law were used, such as  $\tau_b = c_d |v_b| v_b$  where  $v_b$  is the

bottom current and  $c_d$  a nondimensional drag coefficient. Since extensive measurements of bottom currents were made during the field program, the corresponding nonlinear stresses were computed directly from instantaneous observations and then averaged over the whole period of observation. The resultant bottom stress was then divided by the long-term mean current. In stations near the northshore, the mean currents tend to vanish and, hence, separate calculations were made for the first and second half of the period and the results were averaged. Figure 4.19 presents the results for  $c_d = 1 \times 10^{-3}$ , which is a low estimate for this coefficient. For comparison, the solid curve represents the shallow water Ekman formula  $\bar{\tau}_b = BH\bar{v}$  with  $B = 5 \times 10^{-3} \text{ H}^{-2}$  as used in (1)-(4) and with the bar denoting the vertical-mean current. From the viewpoint of effects of bottom friction on long-term averaged circulations, the two formulations appear consistent.

#### 4.9 Conclusions

The purpose of the present study was to evaluate the reliability of typical circulation models by recourse to current meter observations in Lake Ontario for the 140-day period from 4 November 1982 to 23 March 1983. The measurements were taken in a single cross section of the lake with sufficiently high resolution to verify

conservation of total water transport. Effects of model resolution were estimated by comparison of exact and numerical solutions for a circular basin with bathymetry similar to Lake Ontario. Model performance was evaluated for short (days to weeks), intermediate (weeks to months) and long (seasonal) time scales.

The short-term model response to finite wind impulses was verified by comparison with empirical response functions. For longer-term verification, current meter records and model solutions were smoothed by digital filters. Conventional linear hydrodynamic models were found to be adequate for simulating the basic features of all circulations except the seasonal mean. The latter consisted of a cyclonic vortex in the interior of the lake which was found to be due to nonlinear effects. For all except short time scales, adding a moderate amount of horizontal diffusion to the models appeared to improve the results.

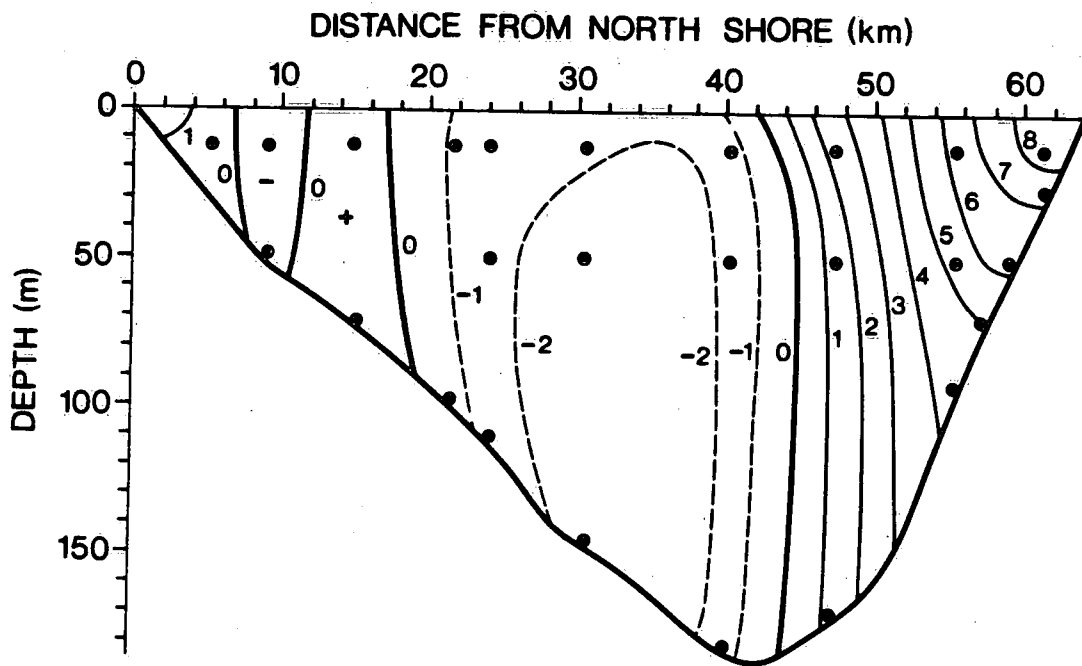


Fig. 4.1 Time-averaged eastward current (cm/s) in Lake Ontario cross section of Figure 1, 4 November 1982 - 23 March 1983. Instrument locations are denoted by black circles.

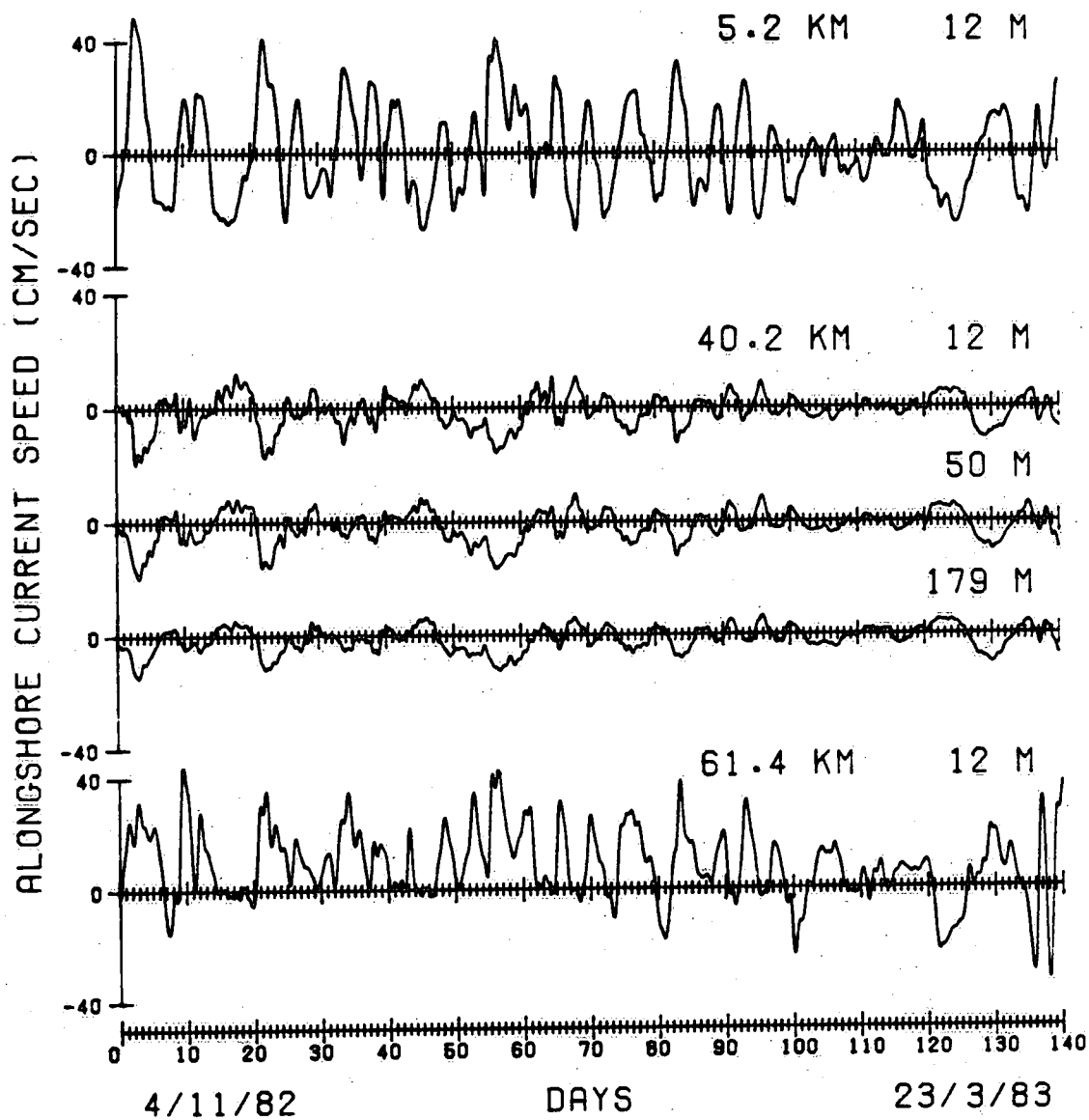


Fig. 4.2 Filtered time series of alongshore currents in Lake Ontario cross section of Figure 1 at indicated depths and distances from north shore.



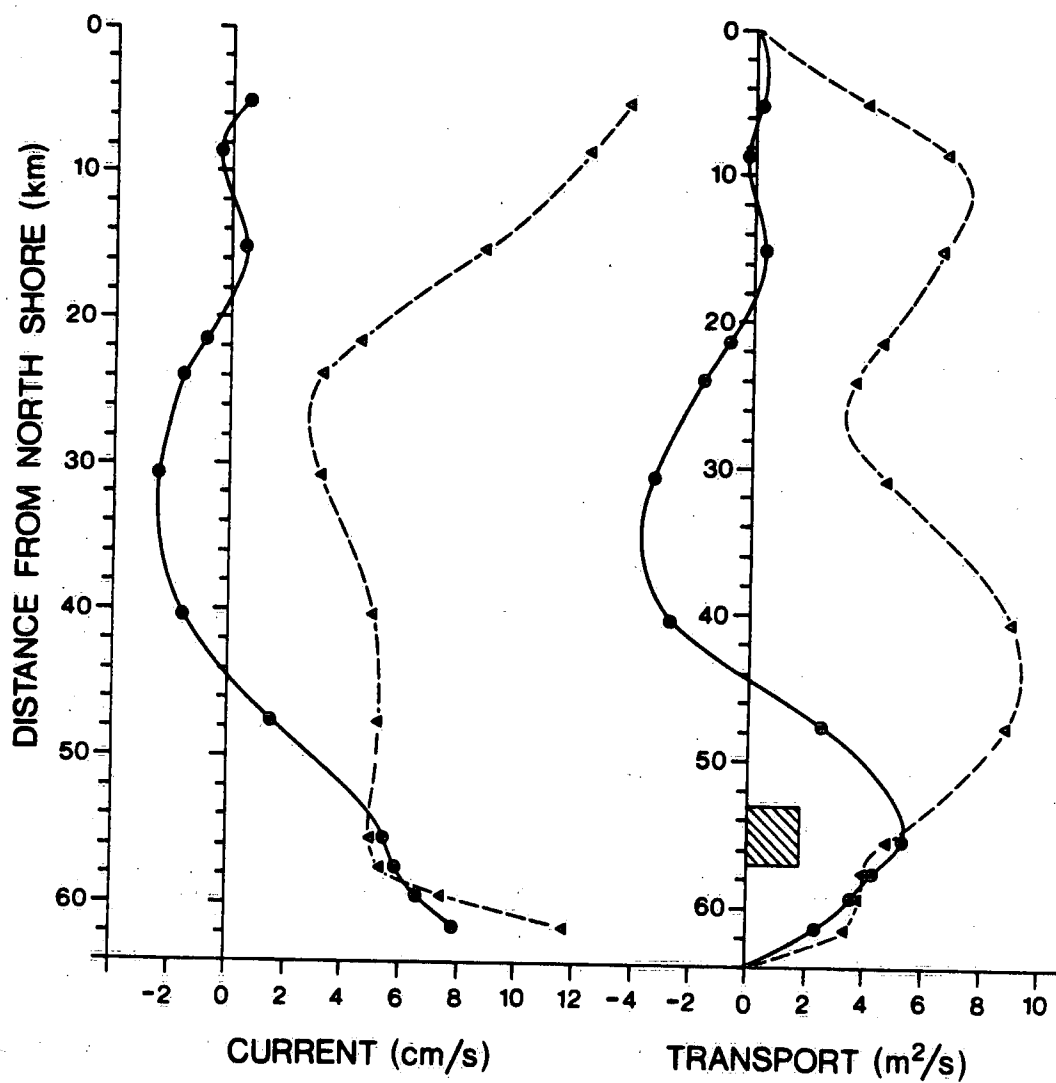


Fig. 4.3 Left: Long-term means (solid lines) and standard deviations in time (dashed) of vertically averaged currents in Lake Ontario cross section of Figure 1, 4 November 1982 - 23 March 1983.

Right: Same for vertically integrated currents. Shaded rectangle illustrates contribution from river flow.

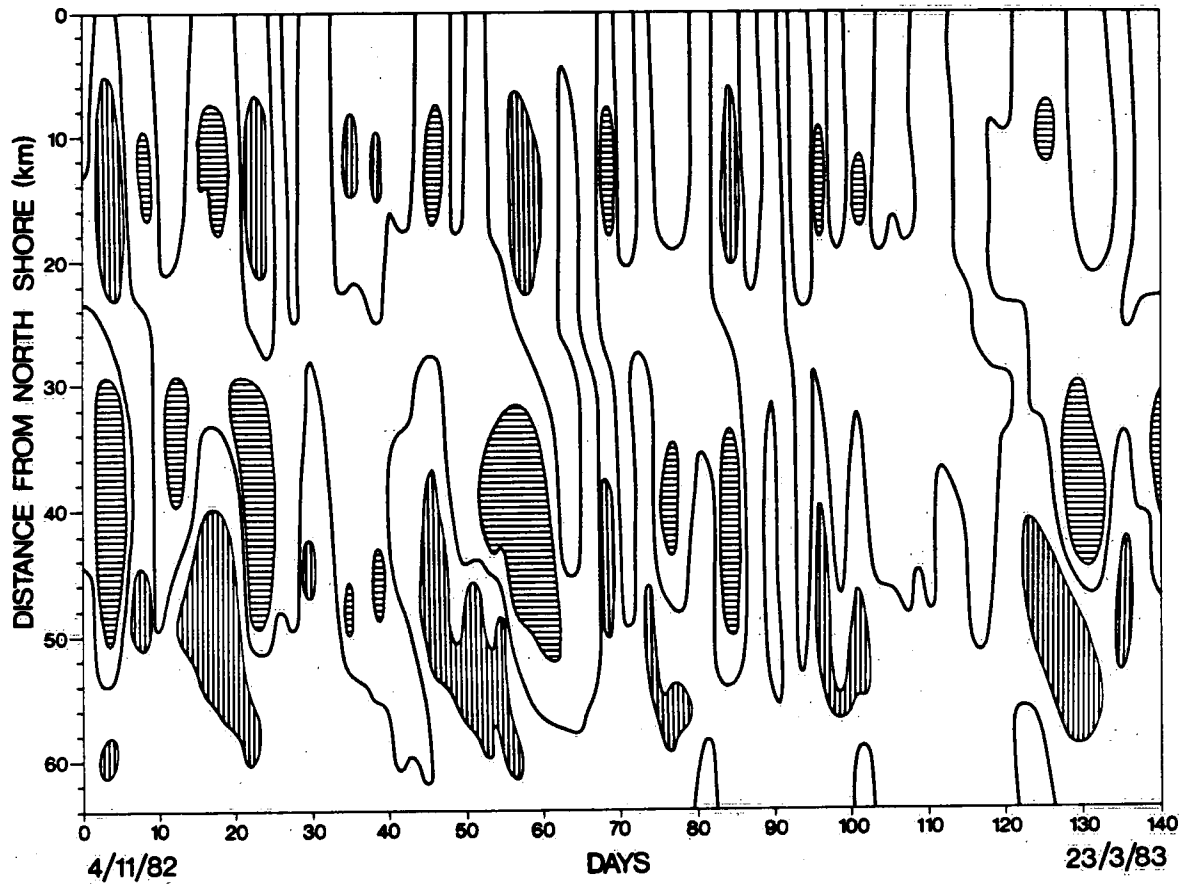


Fig. 4.4 Cross-lake distribution of vertically integrated currents as a function of time. Solid lines denote current reversals (zero transport), vertical shading represents eastward transport greater than 10 m<sup>2</sup>/s, horizontal shading is westward transport greater than 10 m<sup>2</sup>/s.

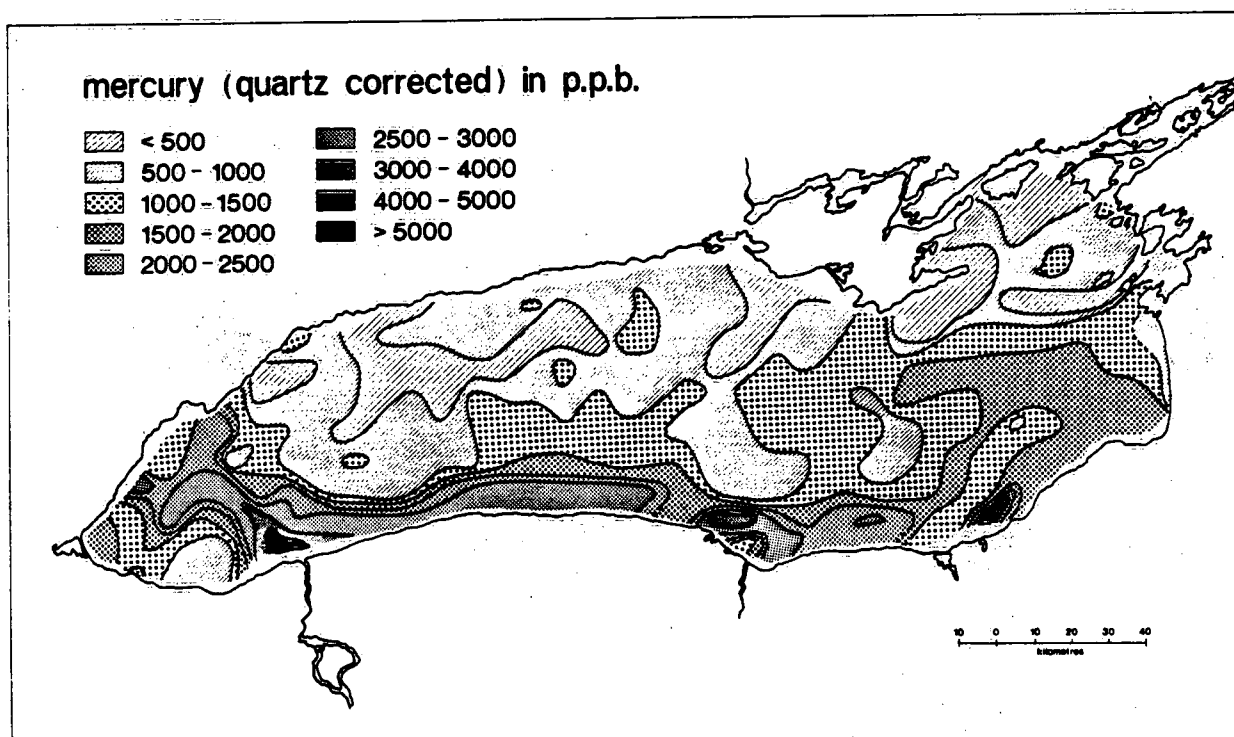


Fig. 4.5 Mercury distribution in Lake Ontario sediments (from Thomas, 1983).

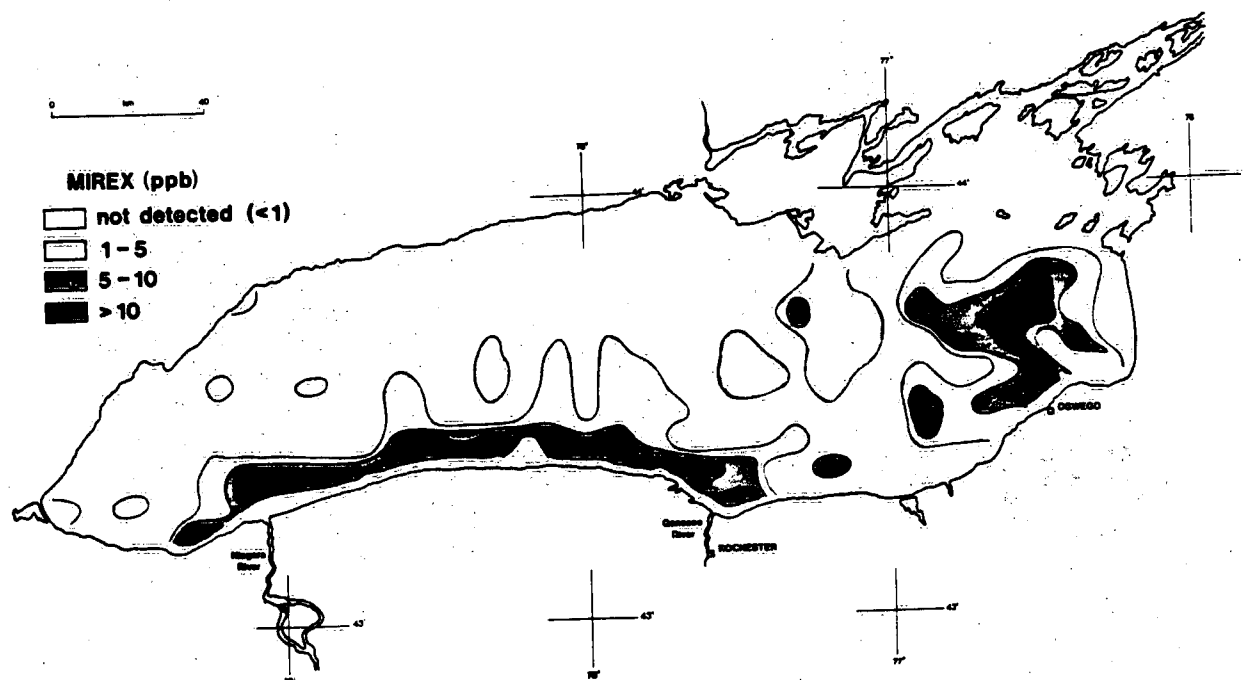


Fig. 4.6 Mirex distribution in Lake Ontario sediments (from Thomas, 1983).

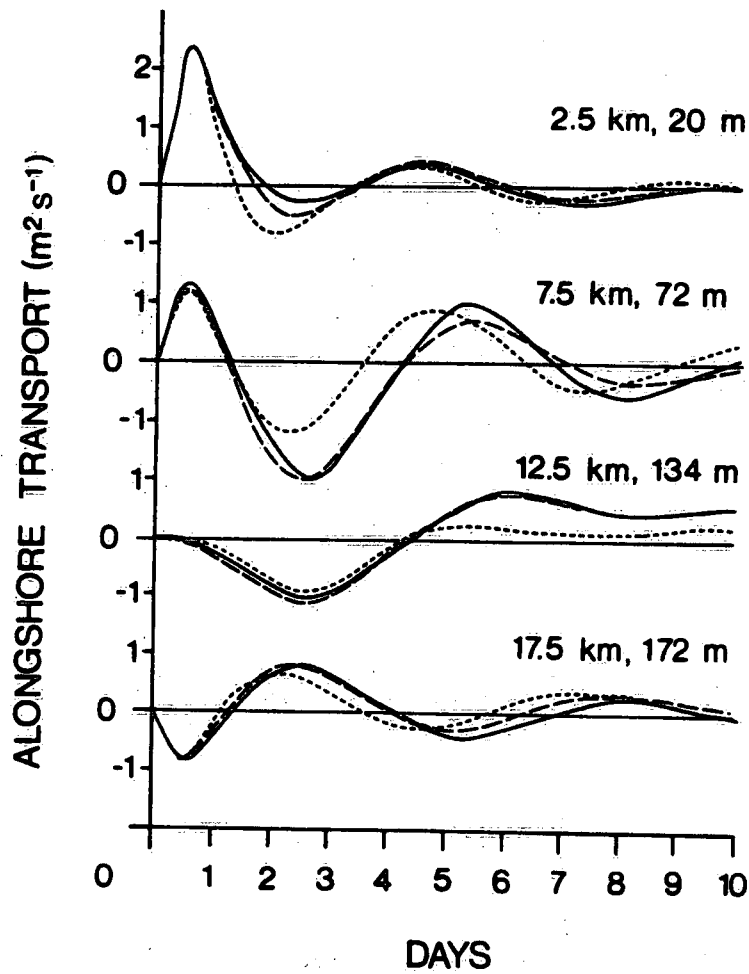


Fig. 4.7 Response of vertically integrated currents to 12-hour wind impulse of  $10^{-1} \text{ Nm}^{-2}$  as a function of offshore distance and depth in a circular basin. Solid: exact solutions; dashed: free-surface model with 5-km grid; dotted: rigid lid model with 5-km grid.

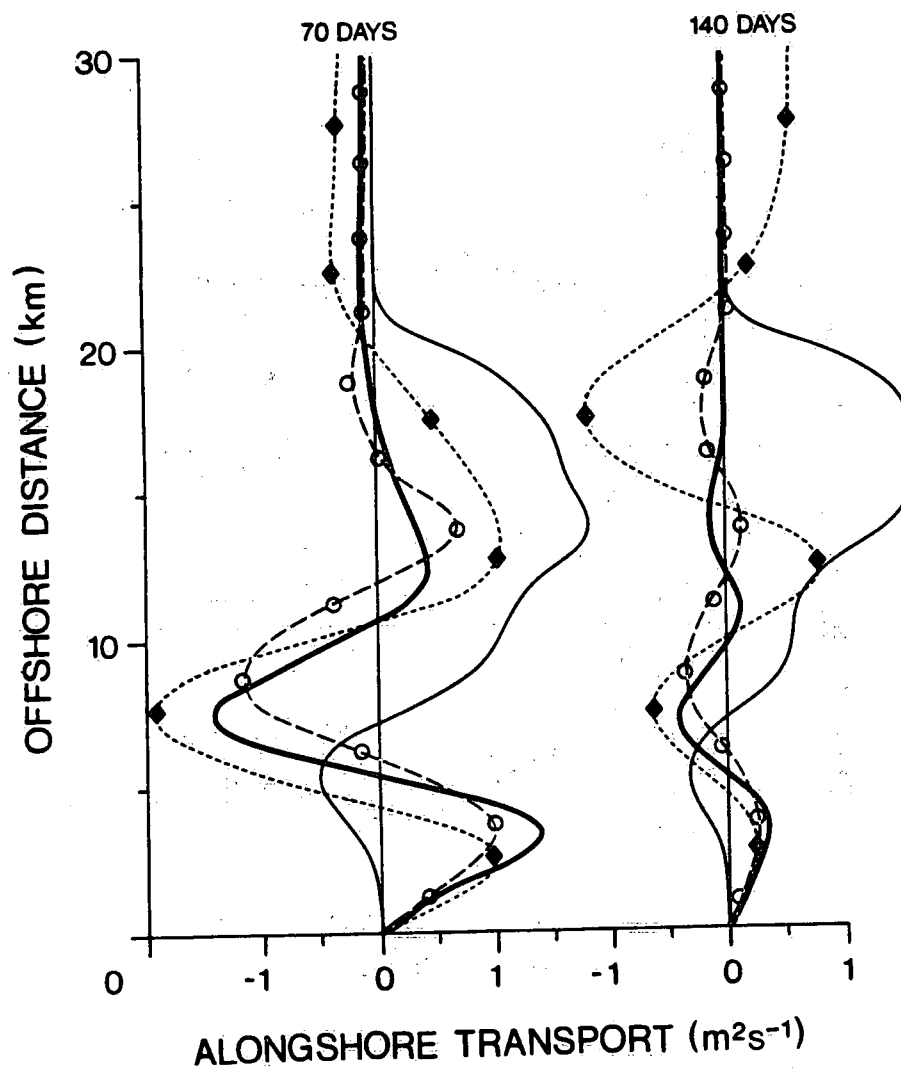


Fig. 4.8 Long-term means of vertically integrated currents in a circular basin for winds observed on Lake Ontario, 4 November 1982 to 23 March 1983. Heavy solid lines: exact solutions; squares: free surface model with 5-km grid; circles: rigid lid model with 2.5-km grid; thin solid lines: second-order circular vortex.

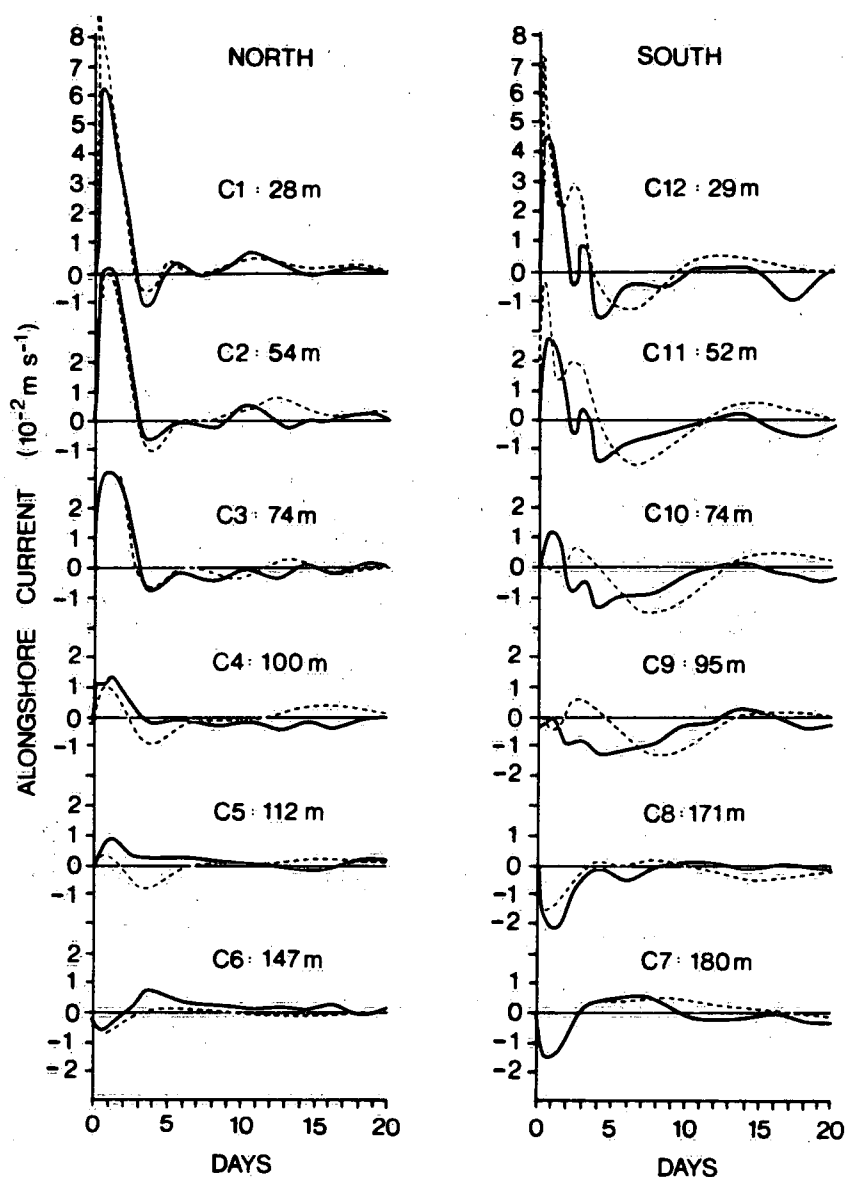


Fig. 4.9 Response of vertically averaged alongshore currents to 12-hour wind impulse of  $10^{-1} \text{ Nm}^{-2}$  for stations of cross-lake array of Fig. 1. Solid curves show empirical results, dashed curves are model results.

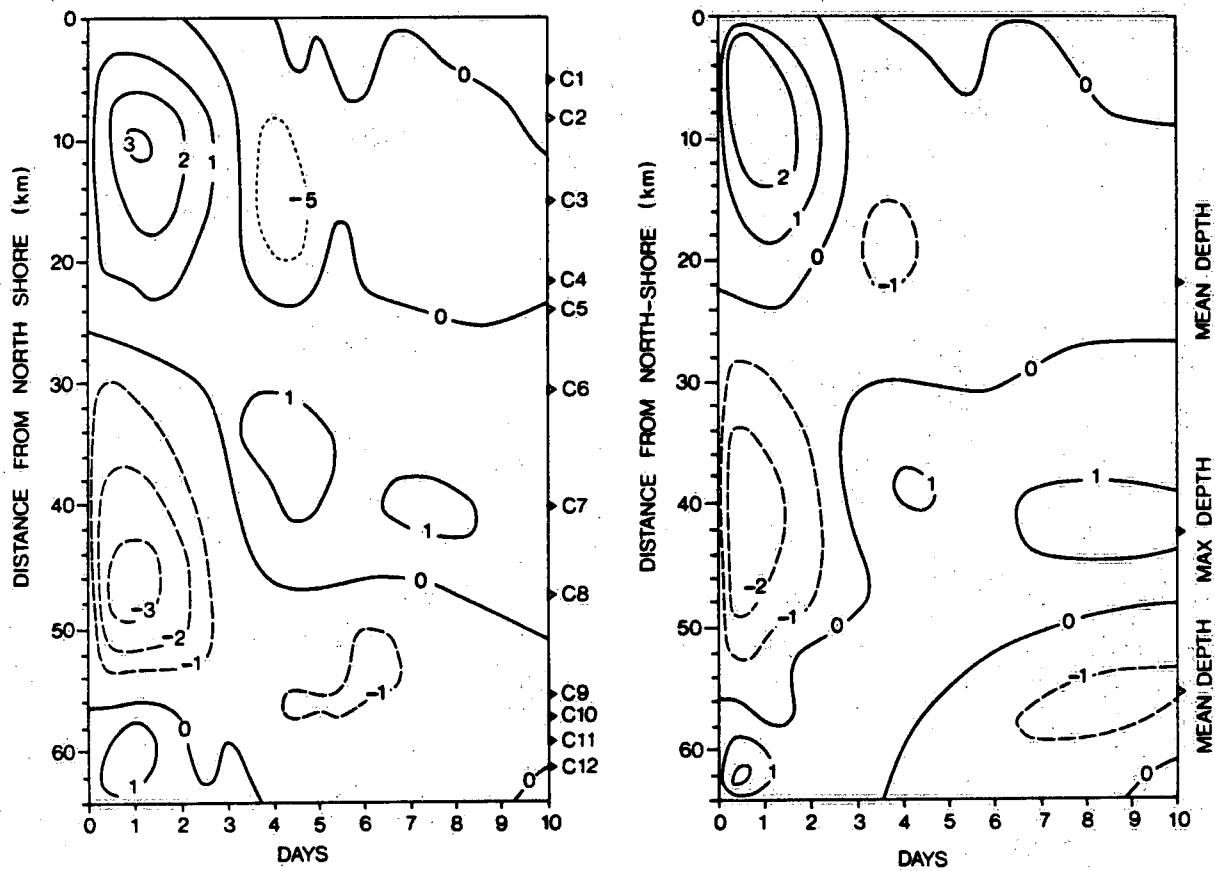


Fig. 4.10 Cross-lake distribution of vertically integrated currents ( $\text{m}^2 \text{s}^{-1}$ ) corresponding to Fig. 4.9. Left: empirical results; right: model results.



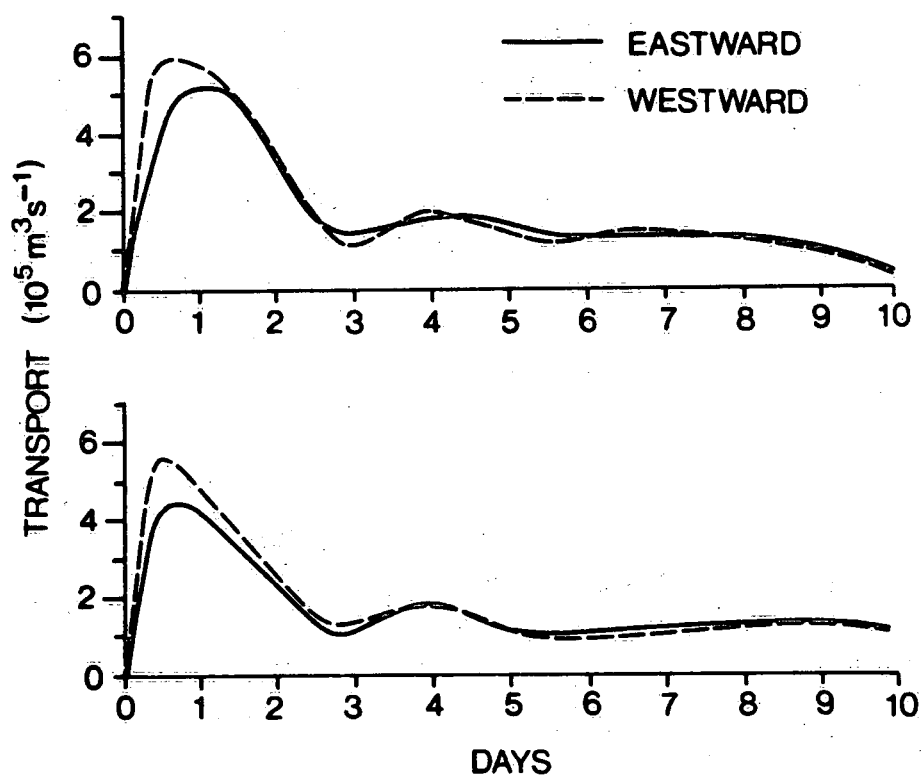


Fig. 4.11 Total eastward and westward transports corresponding to maps of Fig. 4.10. Above: empirical results; below: model results.

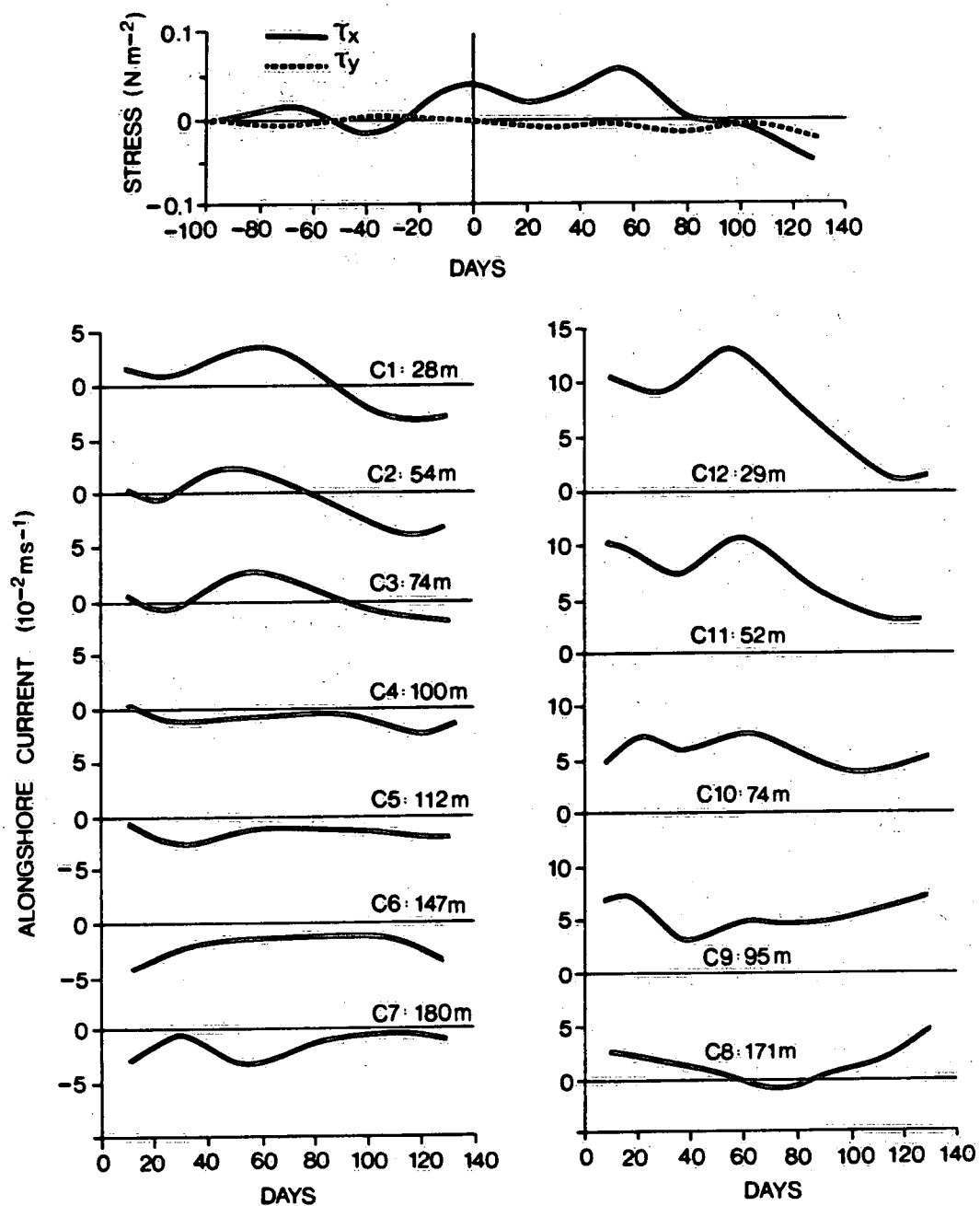


Fig. 4.12 Low frequency variations of alongshore ( $\tau_x$ ) and onshore ( $\tau_y$ ) wind stress and vertically averaged alongshore currents observed in cross section of Fig. 1, 4 November 1982 - 23 March 1983.

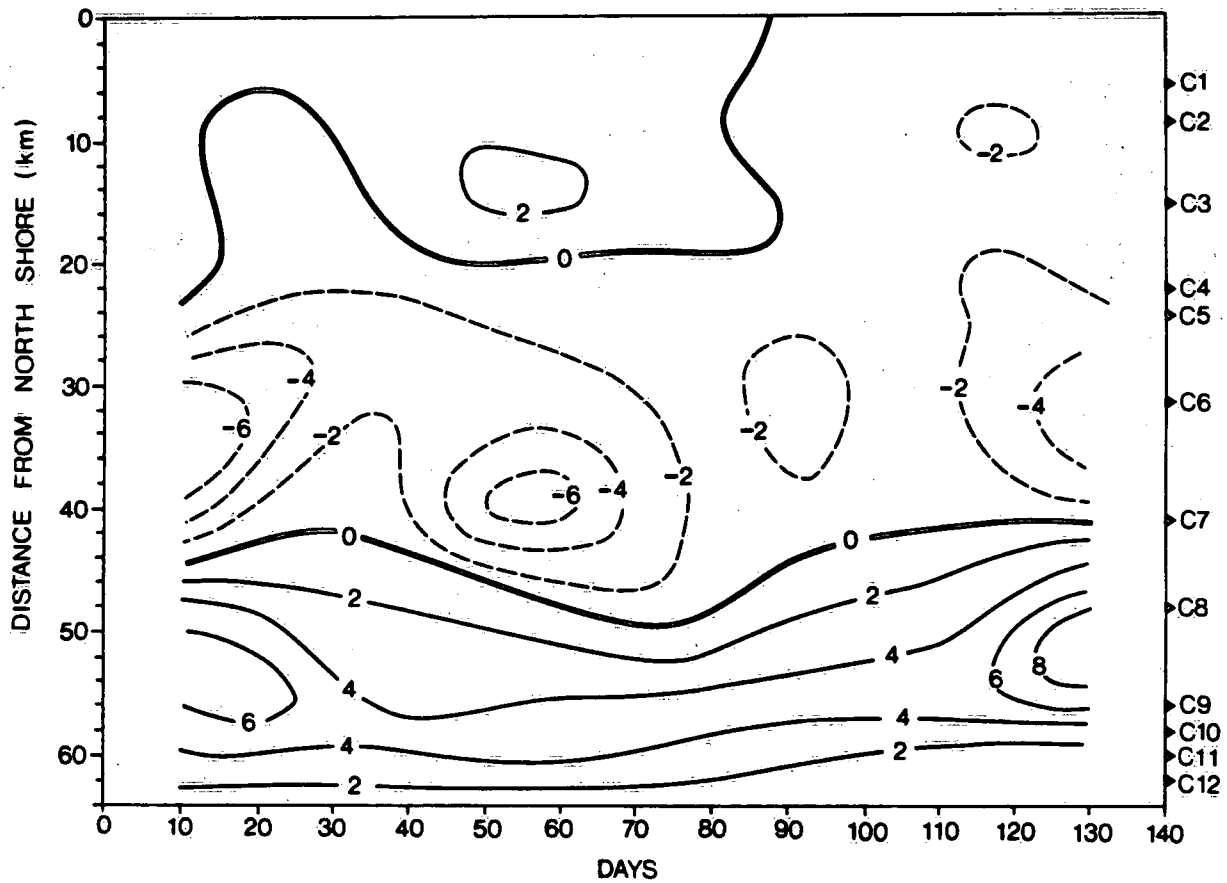


Fig. 4.13 Cross-lake distribution of vertically integrated currents  
( $\text{m}^2 \text{s}^{-1}$ ) corresponding to Fig. 4.12.

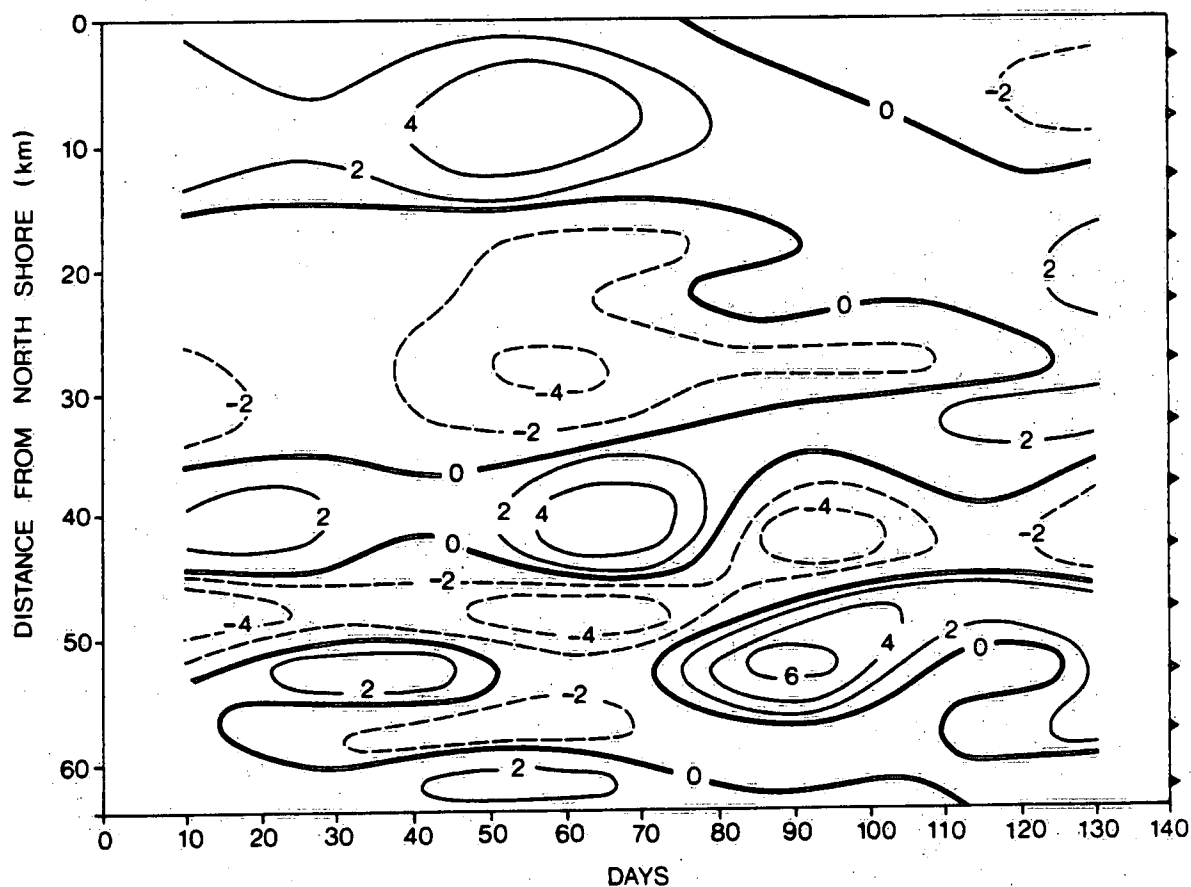


Fig. 4.14 Cross-lake distribution of low-frequency variations of vertically integrated currents ( $\text{m}^2 \text{s}^{-1}$ ) computed by linear free-surface model with 5-km grid.

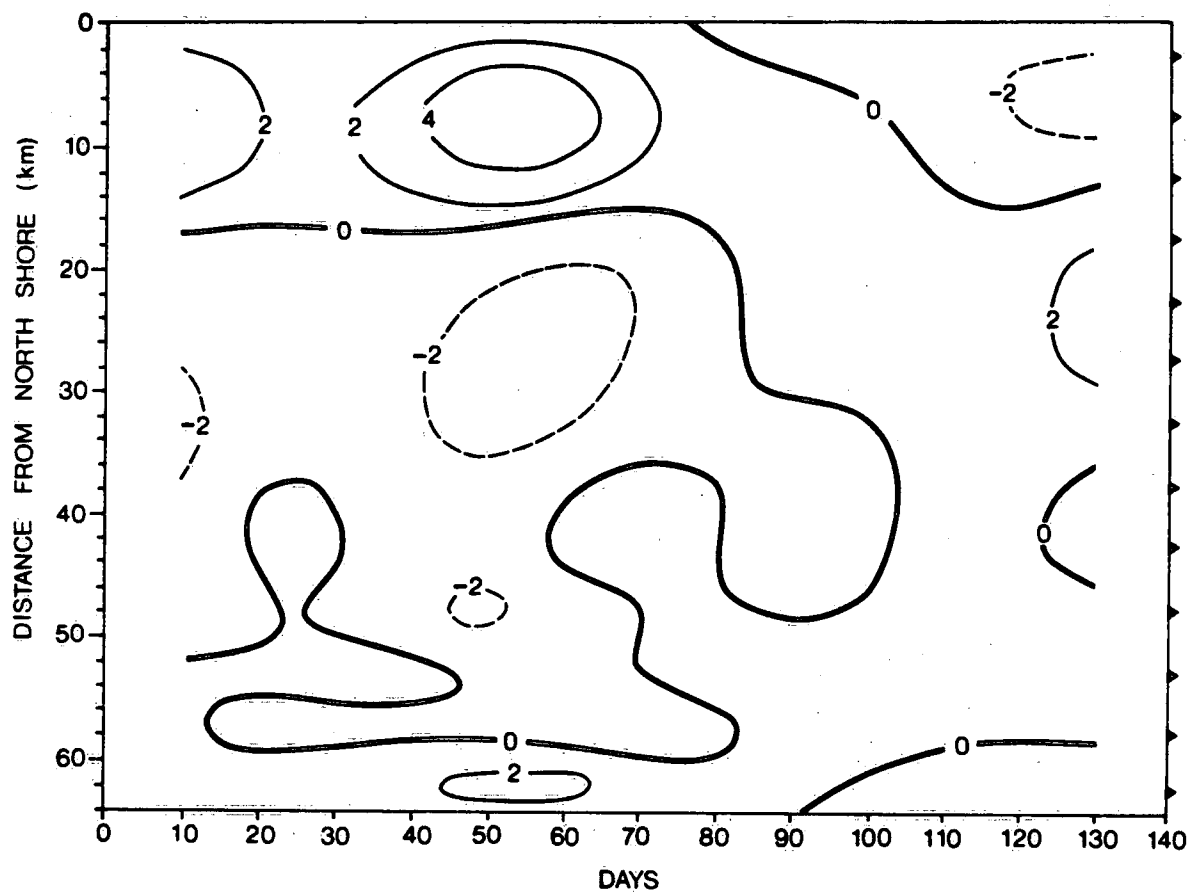


Fig. 4.15 Same as Fig. 4.14 but for linear model with horizontal diffusion of momentum with coefficient of  $25 \text{ m}^2 \text{ s}^{-1}$ .

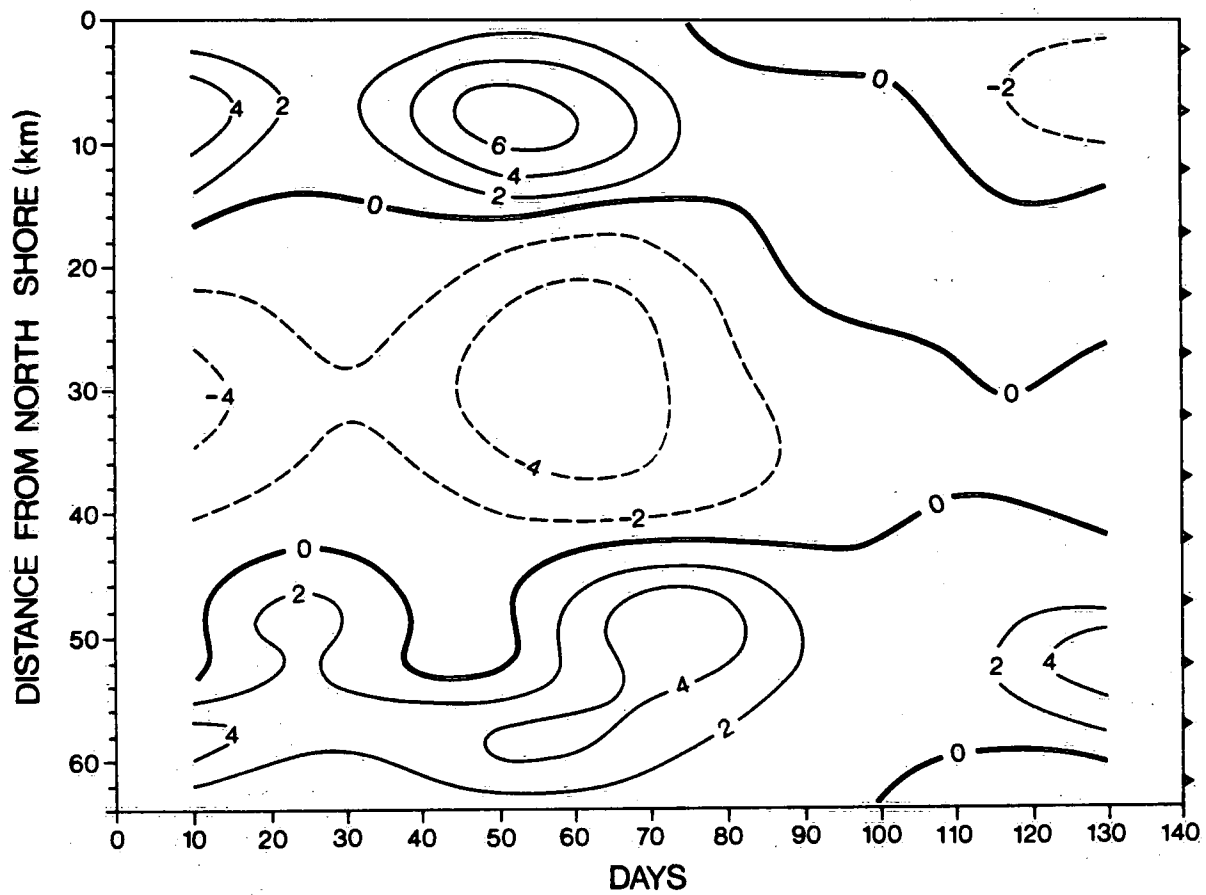


Fig. 4.16 Same as Fig. 4.15 but for nonlinear model with diffusion coefficient of  $25 \text{ m}^2\text{s}^{-1}$ .

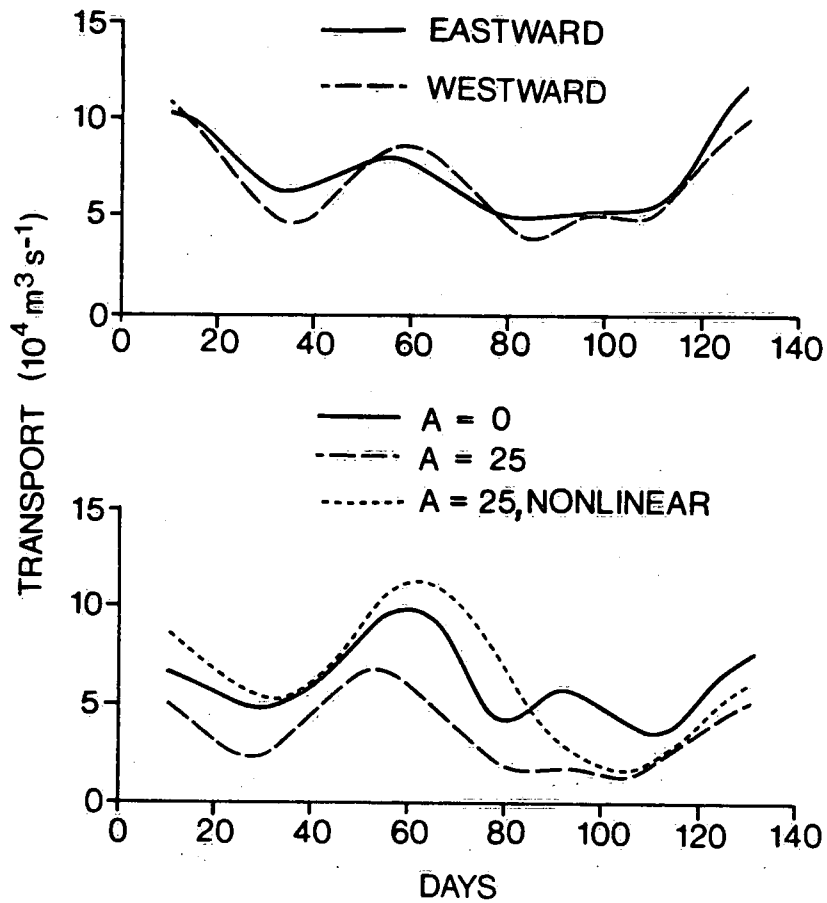


Fig. 4.17 Above: total eastward (solid) and westward (dashed) transports corresponding to Fig. 4.12. Below: total eastward transports corresponding to Fig. 4.14 (solid), Fig. 4.15 (dashes) and Fig. 4.16 (dots).

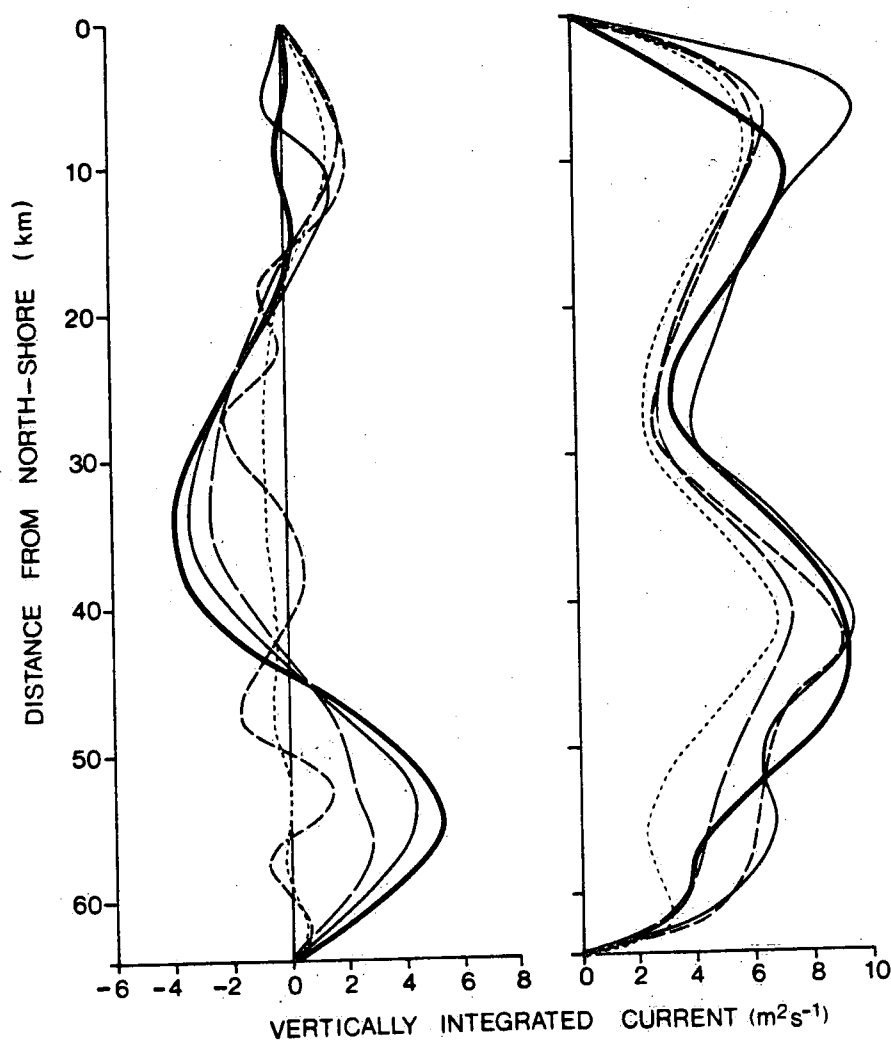


Fig. 4.18 Long-term means (left) and standard deviations in time (right) of vertically integrated currents for cross section of Fig. 1, 4 November 1982 to 23 March 1983. Heavy solid line: observed; dashes: free-surface model without diffusion; dots: free-surface model with horizontal diffusion coefficient of  $25 \text{ m}^2 \text{ s}^{-1}$ ; long dashes: nonlinear free-surface model with diffusion; thin solid line: nonlinear rigid lid model with  $2.5 \text{ km}$  grid and diffusion of  $5 \text{ m}^2 \text{ s}^{-1}$ .



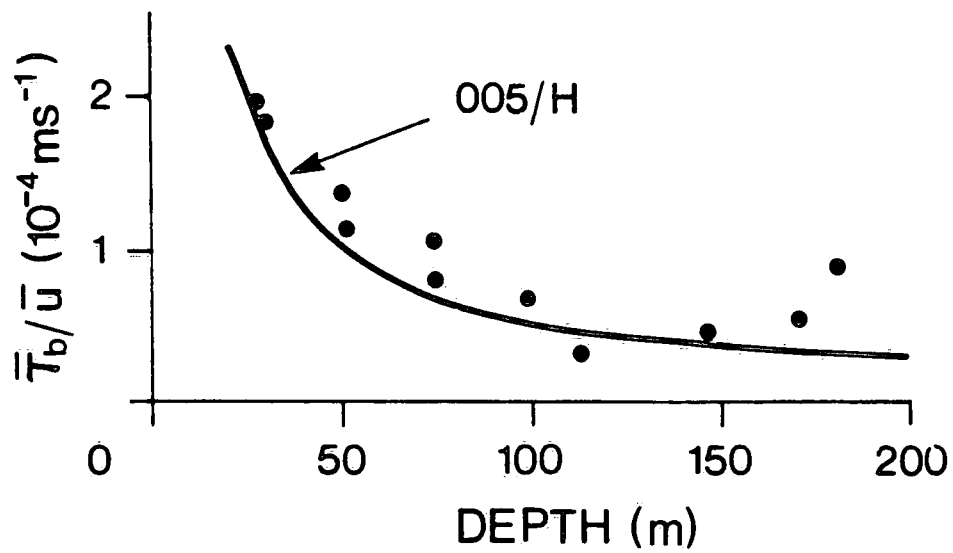


Fig. 4.19 Long-term mean values of nonlinear bottom stress divided by long-term mean currents as obtained from current meter observations in cross section of Fig. 1.

## Winter Study: North Shore

### 5.1 Introduction

In an earlier paper (Simons, 1983), hereafter referred to as RTR, it was argued that observed current fluctuations in homogeneous coastal waters cannot, in general, be explained by either a balance between local wind and bottom stress or by free topographic wave models. Calling to mind the familiar storm surge problem, the response of nearshore currents to wind was visualized as a combination of a directly forced and a free response, with resonance occurring at forcing frequencies corresponding to normal mode solutions. Using observations from Lake Ontario it was also shown that for water depths less than 100 m, topographic waves are rapidly damped out by bottom friction and hence must be continually reinforced by new wind impulses.

The above study relied heavily on numerical models of shelves and rotating basins and to a much lesser extent on observations of winds and currents. The limited data base available for the study did not permit verification of some crucial model results, such as the speed of alongshore wave propagation and alongshore variations in amplitude and resonance frequency of the current response. The more complete series of measurements of the 1982/83 field program permit a test of the validity of the earlier conclusions.

In the former paper it was also shown that the available current observations could be adequately simulated by dynamical models. Analysis and verification of model results in the frequency domain was based on the response of observed and computed currents to periodic wind forcing. Computations in the time domain were made by convolution of wind stress and impulse response functions obtained from two-dimensional numerical models. Naturally, linear transfer models in time can also be estimated directly from observed winds and currents. Such empirical models for nearshore currents are briefly explored in the last part of this Chapter.

## 5.2 Time Series Analysis

The present analysis is concerned with the alongshore array and the northern part of the offshore array. The distance between stations and measurement depths were summarized in Table 1. Winds are available from routine weather observations at Toronto Island Airport, slightly to the west of current meter station A7. The stress is computed in the conventional manner, with a drag coefficient of  $1.2 \times 10^{-3}$  for wind speeds less than  $10 \text{ m s}^{-1}$ , linearly increasing to  $2.4 \times 10^{-3}$  at speeds of  $20 \text{ m s}^{-1}$ , and equal to the latter value for higher wind speeds.

Energy spectra of currents showed that low frequency variations in all stations were aligned with the local bathymetry.

From model experiments it is also known that current variations along the northshore of Lake Ontario are primarily induced by the alongshore component of the wind. Therefore, the following analysis deals with alongshore components of wind stress and currents.

An indication of topographic wave effects on the response of nearshore currents to wind is readily obtained by computing correlations between wind stress and current meter records at different time lags. Figure 5.1 shows lagged cross-covariances between the Toronto Island wind stress and all current observations in the nearshore zone. Solid curves represent surface measurements; dashed curves refer to bottom currents. Current reversals due to wave activity are evidenced by negative correlations starting three to five days after the wind. As expected, the directly-forced initial response to surface stress is considerably greater at the surface than at the bottom, but the subsequent free response is essentially uniform in the vertical. Unlike the cross-covariances, maximum cross-correlations are the same for surface and bottom currents, since the standard deviations of the currents increase toward the surface.

The time lag of maximum correlation increases from the first to the last station of the alongshore array in agreement with the direction of shelf wave propagation. As discussed in RTR, Section 5, such an alongshore variation of phase lag between response and forcing occurs because a uniform wind blowing over a closed basin is equivalent to a wavelike wind pattern over a straight shelf. A much

greater alongshore trend shows up in the time of zero-crossing of the correlation functions. This reflects the westward increase of dominant wave period along this shore found from shelf wave dispersion curves (RTR, Fig. 9) and confirmed by the following spectral results. However, as pointed out by a reviewer, a similar effect would result from wave propagation along a uniform shelf. While this cannot be overlooked, it is felt that the corresponding wave speed of 35 km/day would be an underestimate of the actual value.

The phase speed of shelf wave propagation may be estimated from lagged correlations between individual stations. Similar calculations have been made for the Oregon Shelf by Kundu and Allen (1976) and for Lake Ontario by Clarke (1977) and Marmorino (1979). The results confirm that the time lags of maximum correlation between consecutive stations are in all cases consistent with westward wave propagation. The total lag between the first and last station is about 20 hrs, equivalent to a wave speed of 110 km/day. The speed estimates range from over 200 km/day for the central moorings to as low as 60 km/day for the western stations. This kind of variation might be expected from the above-mentioned shelf wave dispersion curves, but it should be recalled (RTR, Fig. 6) that the apparent phase propagation under conditions of periodic forcing may be significantly affected by friction.

### 5.3 Spectral Analysis

For a detailed analysis of the relation between wind and currents, recourse may be had to computations in the frequency domain. Of special interest is the spectral transfer function, which represents the response of the current to periodic excitation by the wind. The spectral response function is the Fourier transform of the impulse response in the time domain (see, e.g., Blackman and Tukey, 1958). The latter is familiar from storm surge prediction (see, e.g., Schwab, 1979). The frequency response has an amplitude and a phase. The amplitude is the coherent part of the square root of the spectral energy ratio between currents and wind. The units are current ( $\text{m s}^{-1}$ ) divided by wind stress ( $\text{N m}^{-2}$ ). The phase follows from the cross-spectrum and is converted to the lag of the current behind the wind in units of the forcing period.

The power spectra and cross-spectra were computed by the lagged covariance method with maximum lag of 28 days, i.e., one fifth of the total record length of 140 days. Spectral estimates were obtained for periods equal to fractions of 56 days and smoothed by Hanning. Rotary spectra were also computed, showing that nearshore current oscillations were essentially rectilinear and oriented along local depth contours. As noted earlier, the cross-spectra between wind and currents were based on the alongshore components, since the cross-shore component of the wind has less effect on currents in the coastal zone.

As expected from Figure 5.1, the current meter spectra show smooth and consistent variations from one station to the next. It will suffice, therefore, to limit presentation of results to a few illustrations. The left panel of Figure 5.2 shows frequency response functions for the surface currents of the first, middle, and last station in the alongshore array. The right panel of Figure 5.2 presents corresponding results for the first three cross-shore stations, including the cross-over station between alongshore and cross-shore arrays ( $C_2 = A_3$ ). Coherences are shown at the top of Figure 5.2. Amplitudes of bottom currents (not shown) are about one-third smaller than those at the surface, as anticipated from Figure 5.1. The amplitude reduction between surface and bottom appears quite independent of frequency.

The observations of Figure 5.2 may be compared with the model results presented in RTR. Amplitudes and phase lags are seen to display the characteristic frequency dependence of resonant topographic response in the presence of bottom friction. Without such topographic effects the amplitudes would increase more uniformly with period and the phase lags would vary much more slowly as a function of frequency (see, e.g., RTR, Fig. 15). In addition, the spectra confirm some model results which could not be verified in the earlier study due to sparsity of data. First of all, the alongshore variation of phase lag vividly demonstrates the presence of topographic waves. Secondly, it was anticipated that alongshore topographic variations

and the associated shelf wave dispersion curves (RTR, Fig. 9) would cause a gradual shift in resonance frequency along Lake Ontario's northshore. This is indicated by the cross-covariances of Figure 5.1 and it is amply confirmed by the spectral results of Figure 5.2. Finally, numerical calculations for a circular basin (RTR, Fig. 6) suggested a counterclockwise shift of the maximum current response relative to the maximum alongshore component of the wind. This could account for the alongshore amplitude variations of the response functions shown in Figure 5.2.

A few notes of caution must be added here. Results of model calculations (RTR, Fig. 3) suggest that alongshore variations of resonance frequencies due to alongshore depth variations are smaller than expected from local wave dispersion curves. This smoothing effect appears in the eastern half of the alongshore array (stations A1 to A4) but not in the western half (stations A4 to A7). Also, alongshore amplitude variations computed by the same model are not consistent with the present observations. Perhaps this effect of alongshore depth variation is observed by the above-mentioned counterclockwise shift of the current maximum or by variations in offshore distance. In any case, results from a two-dimensional numerical model of Lake Ontario show the same alongshore amplitude variations as found in the observed currents.



#### 5.4 Empirical Models

While a spectral analysis of observations can provide useful insights into the dynamics of the nearshore zone, the more practical problem of modelling nearshore currents must be dealt with in the time domain. In view of the foregoing, the currents cannot be simulated adequately on the basis of a local balance between wind and bottom stress but must include effects of topographic wave propagation and hence, effects of forcing at distant locations. In principle, therefore, the model must cover the whole basin or shelf region. For a recent discussion of the basin-wide topographic response to wind, reference may be made to Schwab (1983). As long as the system is linear, however, it is always possible to compute impulse response functions for the location of interest. The local current is then obtained by convolution of the impulse response with the wind history in one or more stations.

In the previous paper (Simons, 1983), impulse response functions were computed from a two-dimensional numerical model of Lake Ontario. In addition to the linearity of the model, it was assumed that the scale of the forcing was sufficiently large, compared to the size of the lake, so that the forcing would be approximately uniform in space. It is clear that, given those assumptions and given local wind and current measurements, the impulse response may also be obtained directly from these observations. Just like the corresponding

spectral transfer functions, empirical response functions in the time domain shed considerable light on the characteristic behavior of the system and, hence, provide a useful tool for verification of dynamic models. They can also, of course, be used for the practical purpose of modelling currents, thus eliminating the need for numerical models.

The impulse response in time is the Fourier transform of the frequency response function and vice versa (see, e.g., Blackman and Tukey, 1958). Since the latter are already available, the former can be readily obtained. The present spectral results were computed at frequency intervals of  $1/56$  cpd, the total number of frequency estimates being  $28/\Delta t$ , where  $\Delta t$  is the data interval in days. The corresponding Fourier transform has twice as many discrete values in time and is 56 days long. For practical purposes, this impulse response function may be severely truncated. The optimum length may be estimated by truncating the function at different points, convoluting the result with the wind record and comparing the computed current with the current meter record. This procedure showed that the error variance did not decrease if the response function was extended beyond 20 days. The corresponding error variances in percent of observed current variances are presented in Table 5.1.

**Table 5.1 Error variance in percent of variance of observed current for (a) impulse response obtained from spectral response and (b) impulse response obtained by least squares fit**

Depth	Station										
	A1	A2	A3	A4	A5	A6	A7	C1	C2	C3	C4
12 m (a)	25		22	22			23	23	22	24	50
(b)	23		21	21			21	21	21	23	45
50 m (a)	30	21		22	25	26	26				
(b)	27	20		21	23	24	23				

The impulse response can also be obtained directly from time series of observed winds and currents by solving the system of equations generated by convolution of the unknown impulse response function with the wind history for each point of the current meter record. For reliable estimates, the data records should be much longer than the response function and hence the system of equations must be solved in a least squares sense. A number of such algorithms are available in standard computer libraries. Results for the present data set are presented in Table 5.1. Schwab (1979) used this method to obtain an empirical model for storm surge prediction and found the results comparable to those obtained from hydrodynamical models.

To illustrate the present results, Figure 5.3 compares observed and computed currents for the same moorings as in Figure 5.2. The data were smoothed by a low-pass filter with amplitude

response decreasing from unity to zero between 24 and 18 hrs. The empirical model used for these calculations was obtained by the least squares method with data spacing of 12 hrs. As seen in Table 5.1, the error variances for these moorings range from 21 to 23 percent. It is evident that the errors tend to be correlated for all stations. This suggests that inaccurate wind stress estimates are the primary cause of discrepancies between observed and simulated currents. In addition, it should be noted that, although currents along Lake Ontario's north shore are primarily excited by alongshore wind impulses, some effects of cross-shore wind components will occur because the lake is a closed basin. The least squares algorithm can be readily extended to determine impulse responses for both wind components simultaneously. This procedure was found to reduce the mean squared error by up to one third but the results cannot be generalized since they are completely determined by the shape of the basin.

Since the response functions obtained from the data spectra were truncated and the least squares results were derived without regard to the spectra, the frequency transforms of these impulse response functions are not necessarily the same as the frequency response functions obtained from the data spectra (Fig. 5.2). To illustrate the consistency of the various calculations, Figure 5.4 compares results for station A3. The solid line is the original frequency response shown by the solid line in the rhs of Figure 5.2.

The other two curves are the Fourier transforms of the empirical impulse response functions obtained by the two methods described above, the dashed line referring to the first method, the dotted line to the second. The empirical models tend to underestimate the energy transfer for periods of six to seven days and overestimate the low frequency energy.

As a final note it may be added that the impulse response function is an example of a general class of linear transfer models in the time domain. For other models of this type, reference may be made to Box and Jenkins (1970, Ch. 10). Such models are available in standard computer libraries and have also been used for storm surge prediction (Budgell and El-Shaarawi, 1979). Experiments along those lines were carried out here and indicated that these models might be preferable for single-step prediction with the past history of the current as well as the wind being known. For practical purposes, however, this is of less interest. If the Box-Jenkins models are reformulated in terms of the wind history alone, one obtains impulse response functions very similar to those discussed above.

## 5.5 Summary and Conclusions

In an earlier paper (Simons, 1983) hydrodynamic model results and a limited data set were analyzed to evaluate effects of topographic wave propagation on wind-driven currents in homogeneous

coastal waters. In the present Chapter a much more complete series of measurements made in the winter of 1982-1983 along the north shore of Lake Ontario were reviewed. Lagged cross-correlations and spectral transfer functions between winds and currents were found to be consistent with the mechanism of resonant topographic wave response damped by bottom friction. Alongshore variations of amplitude and resonance frequency of the current response reflected effects of alongshore topographic variations estimated from shelf wave dispersion curves.

Empirical transfer function models between wind and currents were also computed in the time domain. Impulse response functions were obtained as Fourier transforms of the frequency response functions and by a least squares fit of current records to wind history. Based on the alongshore component of the wind alone, these models were found to explain about 75 percent of the variance of observed currents.

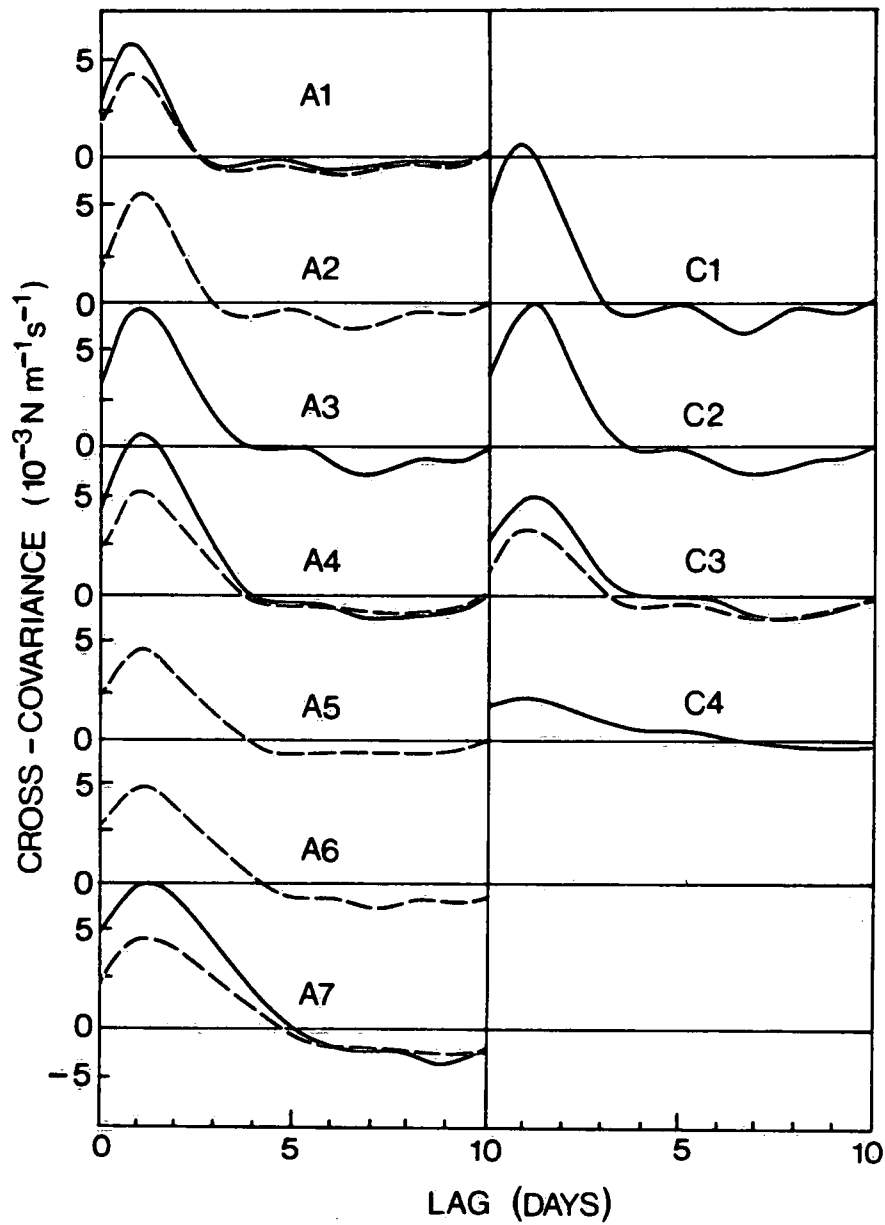


Fig. 5.1 Lagged cross-covariances between alongshore components of wind stress and currents.

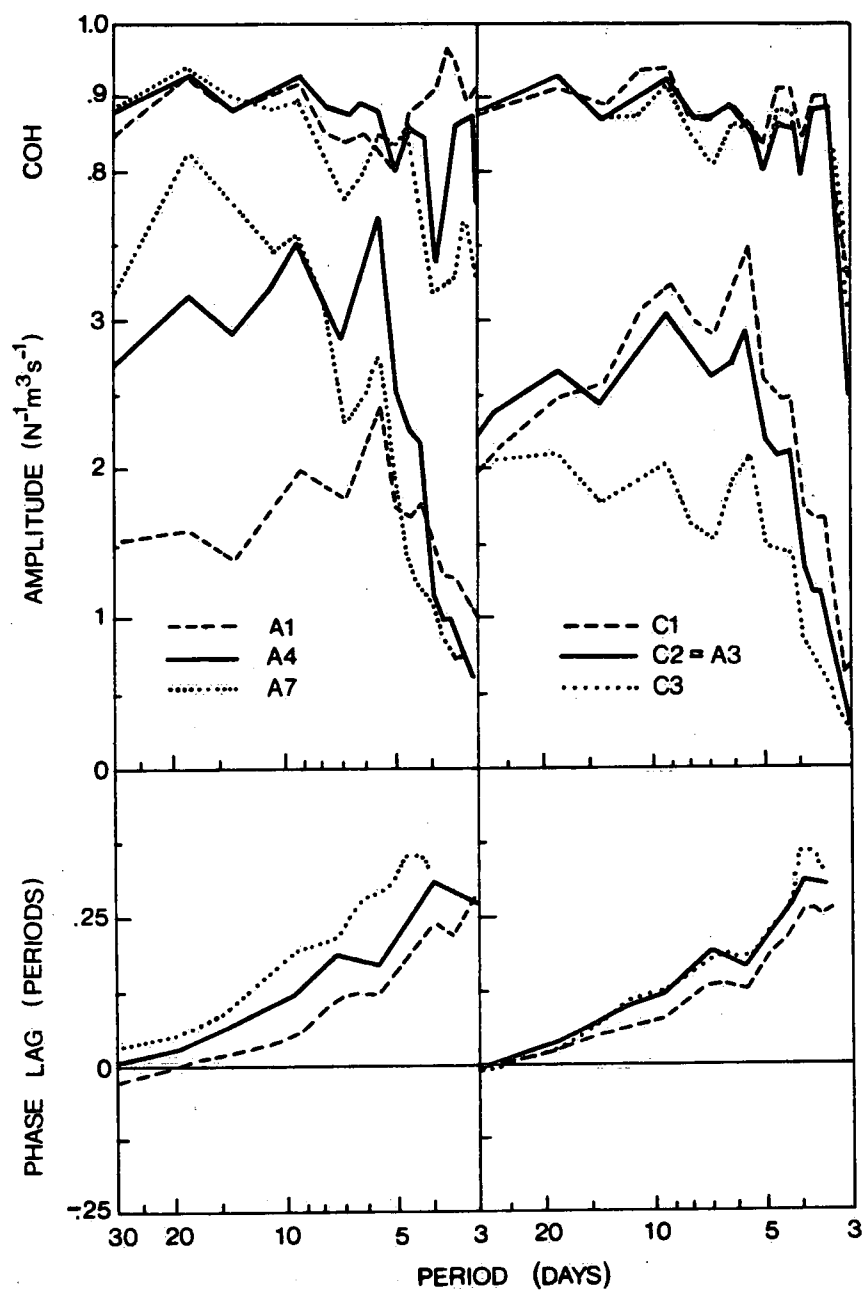


Fig. 5.2 Amplitude and phase of frequency response and coherence between wind stress and selected currents.



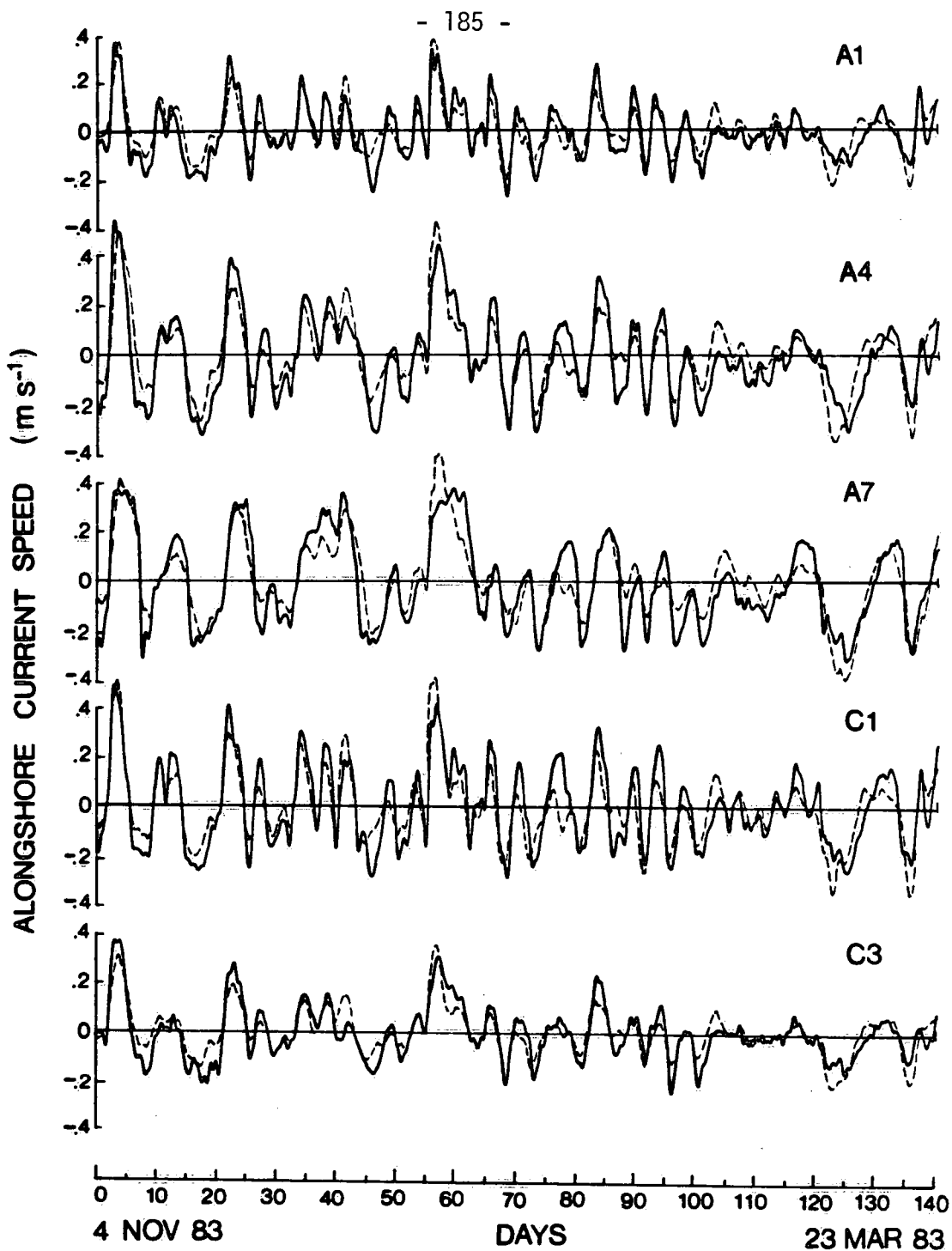


Fig. 5.3 Observed (solid) and computed (dashed) surface currents, smoothed by low-pass filter.

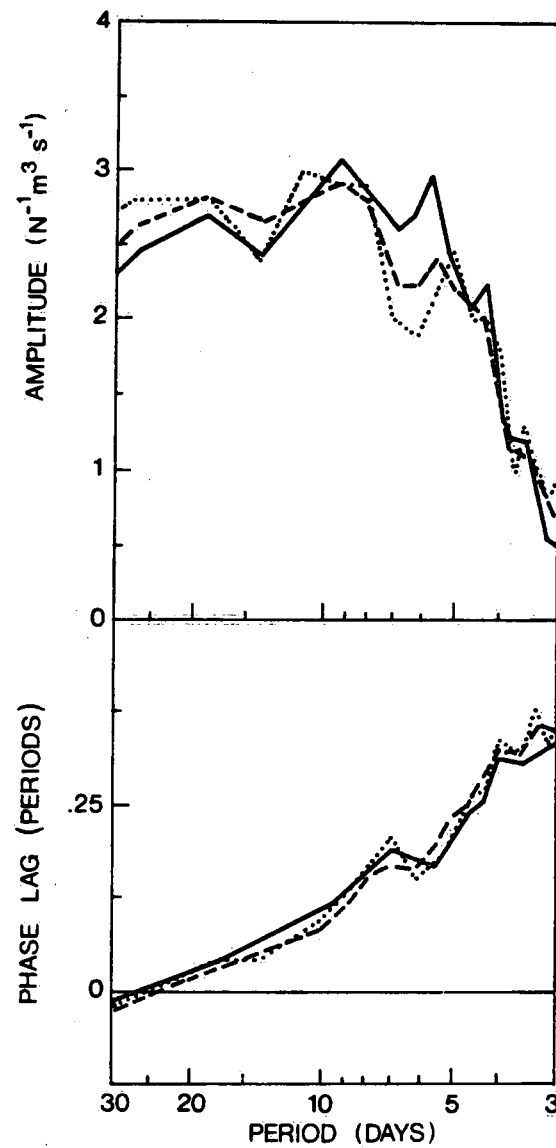


Fig. 5.4 Amplitude and phase of frequency response of current meter station A3. Solid curve: based on spectra of observed wind and current as in Fig. 5.2; dashed: Fourier transform of truncated impulse response obtained from spectra; dotted: Fourier transform of impulse response obtained from least squares fit.

## References

- Allen, J.S. 1975. Coastal trapped waves in a stratified ocean. *J. Phys. Oceanogr.* 5:300-325.
- Allender, J.H. 1977. Comparison of model and observed currents in Lake Michigan. *J. Phys. Oceanogr.* 7:711-718.
- Bennett, J.R. 1973. A theory of large-amplitude Kelvin waves. *J. Phys. Oceanogr.* 3:57-60.
- \_\_\_\_\_ 1974. On the dynamics of wind-driven lake currents. *J. Phys. Oceanogr.* 4:400-414.
- \_\_\_\_\_ 1977. A three-dimensional model of Lake Ontario's summer circulation. I. Comparison with observations. *J. Phys. Oceanogr.* 7:591-601.
- \_\_\_\_\_ 1978. A three-dimensional model of Lake Ontario's summer circulation: II. A diagnostic study. *J. Phys. Oceanogr.* 8:1095-1103.
- Bennett, J.R., and E.J. Lindstrom, 1977. A simple model of Lake Ontario's coastal boundary layer. *J. Phys. Oceanogr.* 7:620-625.
- Birchfield, G.E. 1967. Horizontal transport in a rotating basin of parabolic depth profile. *J. Geophys. Res.* 72:6155-6163.
- \_\_\_\_\_ 1973. An Ekman model of coastal currents in a lake or shallow sea. *J. Phys. Oceanogr.* 3:419-428.
- Birchfield, G.E., and B.P. Hickie, 1977. The time-dependent response of a circular basin of variable depth to a wind stress. *J. Phys. Oceanogr.* 7:691-701.
- Blackman, R.B. and J.W. Tukey, 1958. The measurement of power spectra. Dover, New York, 190 pp.

- Box, G.E.P., and G.M. Jenkins, 1970. Time series analysis: Forecasting and control. Holden-Day, San Francisco, 575 pp.
- Budgell, W.P., and A. El-Shaarawi, 1979. Time series modelling of storm surges in a medium-sized lake. In Predictability and Modelling in Ocean Hydrodyn. (J.C.J. Nihoul, ed.), Elsevier Oceanogr. Ser. 25, 197-218.
- Charney, J.G. 1955. The generation of oceanic currents by wind. J. Mar. Res. 14:477-498.
- Clarke, A.J. 1977. Observational and numerical evidence for wind-forced coastal trapped long waves. J. Phys. Oceanogr. 7:231-247.
- Courant, R., K.O. Friedrichs and H. Lewy, 1928. Über die Partiellen Differenzgleichungen der Mathematischen Physik. Math. Ann. 100:32-74.
- Csanady, G.T., 1968. Motions in a model Great Lake due to a suddenly imposed wind. J. Geophys. Res. 73:6435-6447.
- \_\_\_\_\_ 1973. Transverse internal seiches in large oblong lakes and marginal seas. J. Phys. Oceanogr. 3:439-447.
- \_\_\_\_\_ 1976. Topographic waves in Lake Ontario. J. Phys. Oceanogr. 6:93-103.
- Csanady, G.T., and J.T. Scott, 1974. Baroclinic coastal jets in Lake Ontario during IFYGL. J. Phys. Oceanogr. 4:524-541.
- Donelan, M.A. 1977. A simple numerical model for wave and wind stress prediction. NWRI, Unpubl. Rep., National Water Research Institute, Burlington, Ont., Canada, 21 pp.
- \_\_\_\_\_ 1978. On the fraction of wind momentum retained by waves. Proc. 10th Int. Liege Colloq. Ocean Hydrodyn., Elsevier, Amsterdam.

1982. The dependence of the aerodynamic drag coefficient on wave parameters. First International Conference on Meteorology and Air/Sea Interaction of the Coastal Zone, May 10-14, 1982; The Hague, Netherlands. Published by the American Meteorological Society, Boston, Mass. pp 398-404.
- Gill, A.E., and A.J. Clarke, 1974. Wind-induced upwelling, coastal currents and sea-level changes. Deep-Sea Res. 21:325-345.
- Gill, A.E., and E.H. Schumann, 1974. The generation of long shelf waves by the wind. J. Phys. Oceanogr. 4:83-90.
- Groen, P. and G.W. Groves, 1962. Surges. The Sea, Vol. 1, M.N. Hill (ed.), Interscience, New York:611-647.
- Kundu, P.K., and J.S. Allen, 1976: Some three-dimensional characteristics of low frequency current fluctuations near the Oregon coast. J. Geophys. Res. 84:1206-1214.
- Lilly, D.K., 1965. On the computational stability of numerical solutions of time-dependent non-linear geophysical fluid dynamic problems. Mon. Wea. Rev. 93:11-26.
- Lindzen, R.S. and H.L. Kuo, 1969. A reliable method for the numerical integration of a large class of ordinary and partial differential equations. Mon. Wea. Rev. 97:732-734.
- Marmorino, G.O., 1979. Low-frequency current fluctuations in Lake Ontario, Winter 1972-1973. J. Geophys. Res. 84:1206-1214.
- Mortimer, C.H., 1963. Frontiers in physical limnology with particular reference to long waves in rotating basins. Univ. Michigan, Great Lakes Res. Div., Publ. 10:9-42.

- Murthy, C.R., D.C.L. Lam, T.J. Simons, J. Jedrasik, K.C. Miners, J.A. Bull, W.M. Schertzer, 1984. Dynamics of the Niagara River plume in Lake Ontario. National Water Res. Inst., Burlington, Ont., Canada, Contribution #84-87, 120 pp.
- Mysak, L.A., 1980. Recent advances in shelf wave dynamics. Rev. Geophys. Space Phys. 18:211-241.
- Pickett, R.L., 1976. Lake Ontario circulation in November. Limnol. Oceanogr. 21:608-611.
- Saylor, J.H., J.C.K. Huang and R.O. Reid, 1980. Vortex modes in southern Lake Michigan. J. Phys. Oceanogr. 10:1814-1823.
- Saylor, J.H., J.R. Bennett, F.M. Boyce, P.C. Liu, C.R. Murthy, R.L. Pickett, T.J. Simons, 1981. Water Movements. In: E.J. Aubert and T.L. Richards (eds.) IFYGL - The International Field Year for the Great Lakes. NOAA/GLERL, Ann Arbor, 11:247-324.
- Schwab, D.J., 1978. Simulation and forecasting of Lake Erie storm surges. Mon. Wea. Rev. 106:1476-1487.
- \_\_\_\_\_ 1979. Analytical and empirical response functions for storm surges on Lake Erie. Mar. Sci. Dir., Ottawa, Manuscript Rept. Ser. 53, 140-144.
- \_\_\_\_\_ 1983. Numerical simulation of low-frequency current fluctuations in Lake Michigan. J. Phys. Oceanogr. 13:2213-2224.
- Schwab, D.J., J.R. Bennett, P. Liu and M.A. Donelan, 1984. Application of a simple numerical wave-prediction model to Lake Erie. J. Geophys. Res. 89:3586-3592.
- Simons, T.J. 1972. The nonlinear dynamics of cyclone waves. J. Atmos. Sci. 29:38-52.

- \_\_\_\_\_ 1975. Verification of numerical models of Lake Ontario, II. Stratified circulations and temperature changes. J. Phys. Oceanogr. 6:372-378.
- \_\_\_\_\_ 1975. Effective wind stress over the Great Lakes derived from long-term numerical model simulations. Atmosphere, 13:169-179.
- \_\_\_\_\_ 1976. Verification of numerical models of Lake Ontario, III. Long-term heat transports. J. Phys. Oceanogr. 6:372-378.
- \_\_\_\_\_ 1980. Circulation models of lakes and inland seas. Can. Bull. Fish. Aquat. Sci. 203, Can. Govt. Publ. Centre, Ottawa; 146 p.
- \_\_\_\_\_ 1981. Verification of seasonal stratification models. Inst. Meteorol. Oceanogr. Univ. of Utrecht, 16 pp.
- \_\_\_\_\_ 1983. Resonant topographic response of nearshore currents to wind forcing. J. Phys. Oceanogr. 13:512-523.
- Thomas, R.L. 1983. Lake Ontario sediments as indicators of the Niagara River as a primary source of contaminants. J. Great Lakes Res. 9:118-124.
- Wang, D.P. 1975. Coastal trapped waves in a baroclinic ocean. J. Phys. Oceanogr. 5:326-333.
- Welander, P. 1959. On the vertically integrated mass transport in the oceans. The atmosphere and sea in motion. (B. Bolin, ed.), Rockefeller Inst. Press, pp. 95-101.



3 9055 1017 2870 6

# DATE DUE REMINDER

APR 2 1998

08 JUL 2009

Please do not remove  
this date due slip.